University of Kassel

Faculty 10 - Mathematics and Sciences

Quantification and Local Modification of the Interfacial DMI

Master thesis

Nanoscience

Date of submission: September, 2022

Participant:

B. Sc. Arne Jan Vereijken

1st Assessor:

Prof. Dr. Arno Ehresmann

2nd Assessor:

Prof. Dr. Thomas Giesen

Contents

List of Figures

List of Tables

1 Motivation

The Dzyaloshinskii-Moriya interaction (DMI) is an asymmetric exchange interaction [1, 2] promoting chiral coupling between adjacent spins, giving rise to robust, chiral, topological spin textures [3]. This includes skyrmions with outstanding properties for information storage and processing [4, 5, 6, 7]. It is known in the literature that DMI originates, e.g., from the interface between a ferromagnet (FM) and a heavy metal (HM) with large spin-orbit coupling (SOC) in non-centrosymmetric heterostructures [8, 9]. Thereby, such thin film heterostructures possess the potential of technological importance [3, 10], motivating the optimization of the DMI. Recently it has been demonstrated that the DMI at such FM/HM interfaces can be tuned by irradiation with keV He^+ ions [8, 11]. The ion bombardment is interesting for further research and engineering of directed domain wall or skyrmion motion [6, 7].

The DMI acts as an intrinsic in-plane field on domain walls, energetically favoring Néel domain walls over Bloch domain walls. This property is utilized in the first part of this work (sections 3 and 4) to implement the domain wall velocity-based asymmetric bubble expansion method for quantification of the DMI by using high-resolution Kerr microscopy. Compared to other DMI-specific methods, the asymmetric bubble expansion method is easily available and does not require complex sample preparation, although the domain structure, which differs from the bubble domains and is referred to be dendrimeric, or maze- or labyrinth-like, entails difficulties [9].

After successful implementation and adaptation of the magneto-optical quantification method, it is applied to the second part of this work (sections 5 and 6), systematically investigating the influence of local He^+ ion bombardment on the magnetization dynamics in a perpendicularly magnetized multilayer system. Ideally, the DMI might be dose-dependently modified as observed in [8]. As the ion bombardment does not solely change the interfacial DMI, the modification of other magnetic properties, e.g., saturation magnetization and effective magnetic anisotropy, is investigated as well by utilizing a vector vibrating sample magnetometer.

In the last part of the work (section 7), some further investigations and optimization approaches are presented, concerning the magneto-optical investigation of the domains. Thereby, the preferred growth direction and the size distribution of the dendrimeric structure are examined. A few proposals for the automatization of the measurement procedure are provided there as well. Prior to the first part of this thesis, a brief introduction to the most important magnetic properties of the investigated sample system is given in section 2.

2 Theoretical Background

This chapter will briefly introduce several basic phenomena and principles of physics which provide proficient support in understanding the goals, experiments, and results of this thesis. The focus here is essentially on understanding the magnetic properties of the samples to be examined. The later sections 3 and 5 will provide deeper insights into the experimentally determined and modified properties as well as the physical phenomena that enable the analysis or modification of these properties either directly or indirectly.
The most important properties are the interfacial Dzyaloshinskii-Moriya interaction (DMI) in section 2.3, the saturation magnetization, the magnetic anisotropy, and the exchange stiffness in section 2.1 as well as the domain structure and domain walls in section 2.2 [9].
A bottom-up approach is chosen to explain the basic and important magnetic properties of the examined samples. Hereby, starting from the quantum mechanically determined magnetic moments of individual atoms and molecules, the model is built up until it can describe the macroscopical magnetic properties of the samples.

2.1 Magnetic Moments, Interactions and Anisotropy Effects

The following section will introduce the atomic or molecular magnetic moment as an elementary entity for the magnetization properties of especially ferromagnetic matter. Like the properties of antiferromagnetic and ferrimagnetic materials, it originates from the collective ordered behavior of these elementary magnetic dipole moments [12, 13].This collective behavior of the individual magnetic moments and the thereby arising macroscopic magnetic properties of matter are discussed at the end of this section, in 2.1.3. In section 2.1.2, the magnetic interaction mechanisms responsible for the collective behavior are introduced. The major part of the following section is based on the books [13], [12], and [14] which offer a deeper insight into the treated topics.

2.1.1 Magnetic Properties of Individual Atoms or Molecules

Magnetic fields and thus magnetism emerges from electrical charges in motion [12, 13]. Considering solid matter, this is either a classical electric current, which can explain the properties of electromagnetic conductors, or the intrinsic orbital motion and spins of electrons and nuclei, resulting in individual atomic or molecular magnetic dipoles. This second type of atomic and molecular magnetic dipoles is the foundation of the magnetic properties in matter.

In Bohr's semi-classical atomic model, the interatomic or molecular electron movements are considered as a circular electric current I with the elementary charge $-e$ in a closed circular loop with radius $\vec{r}$ and area $|\vec{A}| = \pi\vec{r}^{\,2}$ [12, 13]. The strength of the resulting magnetic dipole is quantified by the angular magnetic moment $\vec{\mu}_\mathrm{l}$ according to

$$\vec{\mu}_\mathrm{l} = -\mu_0 \left(\frac{e\omega_\mathrm{e}}{2\pi}\right) \cdot \pi\vec{r}^{\,2} \cdot \frac{\vec{A}}{|\vec{A}|} = -\frac{\mu_0 e\omega_\mathrm{e}\vec{r}^{\,2}}{2} \cdot \frac{\vec{A}}{|\vec{A}|} \quad [13]\,, \tag{1}$$

with μ_0 as the permeability in vacuum and ω_e as the angular velocity resulting in $\omega_\mathrm{e}/2\pi$ turns per second. With the electron mass m_e, the orbital angular momentum $\vec{l} = m_\mathrm{e}\omega_\mathrm{e}\vec{r}^{\,2} \cdot \vec{A}/|\vec{A}|$, which magnitude $\vec{l}^{\,2} = l(l+1)\hbar^2; l \in \mathbb{N}_0$ is quantized in an integer multiple of Planck's reduced constant $\hbar$, and Ampère's circuital law $\vec{\mu}_\mathrm{l} = I \cdot \vec{A}$, Eq. (1) results in

$$\vec{\mu}_\mathrm{l} = I \cdot \vec{A} = -\frac{\mu_0 e}{2m_\mathrm{e}} \cdot \vec{l} \tag{2}$$

$$|\vec{\mu}_\mathrm{l}| = -\frac{\mu_0 e\hbar}{2m_\mathrm{e}} \cdot \sqrt{l(l+1)} = -\mu_\mathrm{B} \cdot \sqrt{l(l+1)}\,. \tag{3}$$

The magnetic moment is aligned parallel to the surface normal of the loop and the orbital momentum. In the later part of the second equation, the constants are summarized into a constant magnetic moment, the Bohr magneton μ_B, which represents the smallest possible magnetic moment of electrons [13, 14, 12]. Depending on the orbital quantum number l, the magnetic moment is given in integer multiples of the Bohr magneton. The magnetic moment of the positive nuclei is determinable analogously. However, the inverse proportionality of $1/m$ scales the magnetic moment of the nuclei down to a non-appreciable small value relative to the magnetic moment of electrons [14].

In addition to the electron's orbital momentum, which results from its binding state, the spin angular momentum $\vec{s}^{\,2} = s(s+1)\hbar^2; s \in [-\frac{1}{2}, +\frac{1}{2}]$, as an intrinsic degree of freedom of the electrons, causes a magnetic moment $\vec{\mu}_\mathrm{s}$ depending on the spin quantum number $s = \pm\frac{1}{2}$. Analogously to the magnetic moment in Eq. (3), the magnetic moment caused by the spin amounts to

$$|\vec{\mu}_\mathrm{s}| = \frac{\mu_0 e}{m_\mathrm{e}} \cdot |\vec{s}| = 2 \cdot \mu_\mathrm{B} \cdot \sqrt{s(s+1)}\,. \tag{4}$$

Hereby, the projection of the magnetic moment along the z-axis is given by

$$|\vec{\mu}_{\mathrm{s},z}| = 2 \cdot \mu_\mathrm{B} \cdot |s_z| = \mu_\mathrm{B}\,. \tag{5}$$

The prefactor for the magnetic moment arising from the spin momentum is twice as high as that of the orbital momentum. This ratio g between the two contributions towards the

electron magnetic moment is labeled as a gyromagnetic ratio or more precisely g-factor [1]. With this factor, the total magnetic moment of an electron is

$$\vec{\mu}_{\mathrm{e}} = \vec{\mu}_{\mathrm{l}} + \vec{\mu}_{\mathrm{s}} = -\frac{\mu_0 e}{2m_{\mathrm{e}}} \cdot \left(\vec{l} + g\vec{s}\right) = -\mu_{\mathrm{B}} \left(\vec{l} + g \cdot \vec{s}\right) . \tag{6}$$

The equation (6) shows that the magnetic moment of an electron arises from the occupied quantum mechanical state described by the angular moments $\vec{l}$ and $\vec{s}$ with the quantum numbers l and s. With Eq. (1 - 6), the magnetic moment of a single electron is described. In atoms, however, the total magnetic moment is composed of the entire superimposed sum of the individual magnetic moments. Hereby, the relative orientation of the individual contributions to one another has to be taken into account, since they can increase or even balance out depending on the mutual direction.

For the description of the total electronic situation in an atom, the quantum numbers of the total orbital angular momentum $\vec{L} = \sum \vec{l}_{\mathrm{i}}$; $\vec{L}^2 = L(L+1)\hbar^2$, the total spin angular momentum $\vec{S} = \sum \vec{s}_{\mathrm{i}}$; $\vec{S}^2 = S(S+1)\hbar^2$, and the total angular momentum $\vec{J} = \vec{L} + \vec{S}$; $\vec{J}^2 = J(J+1)\hbar^2$ are introduced, whereby each is composed of the sum of the corresponding quantum numbers of the individual electrons, taking their spatial orientation into account. Treating the collective behavior of all electrons by these vector sums of the individual quantum numbers is usually referred to as the vector model of atoms [13, 15] and requires the so-called LS coupling (see section 2.1.2 Spin-Orbit-Coupling). This results in a magnetic moment $\vec{\mu}_{\mathrm{J}}$ with the strength

$$\vec{\mu}_{\mathrm{J}} = \vec{\mu}_{\mathrm{L}} + \vec{\mu}_{\mathrm{S}} = -\mu_{\mathrm{B}} \left(\vec{L} + g \cdot \vec{S}\right) = -\mu_{\mathrm{B}} g_{\mathrm{J}} \cdot \vec{J} . \tag{7}$$

The dimensionless g-factor g_{J} is called the Landé factor after its empirical discoverer and its value is in between the range of 1 and 2 depending on L, S, and J, according to

$$g_{\mathrm{J}} = 1 + \frac{J(J+1) + S(S+1) - L(L+1)}{2J(J+1)} \quad [13] . \tag{8}$$

The electronic configuration of the atomic ground state is determined by the Aufbau principle, which is composed of Pauli's exclusion principle, Hund's four rules, and the Madelung energy ordering rule [13]. Hund's rules are particularly important for the prediction of the magnetic moment.

These atomic and molecular magnetic dipole moments, which result from the occupation of the quantum mechanical states, are responsible for the properties of magnetic materials.

[1] Both, the g-factor and the gyromagnetic ratio address the ratio between angular momentum and magnetic moment, whereby the first is the mentioned dimensionless factor of 2 and the second includes all physical constants in front of both angular moments $\vec{P}_{\mathrm{l}}$ in Eq. (3) and $\vec{P}_{\mathrm{s}}$ in Eq. (4).

2.1.2 Magnetic Exchange Interactions

This section will provide an overview of interaction mechanisms that are of crucial importance for the elementary dipole moments discussed in the previous section.

Magnetic Dipole Moments in Magnetic Fields

The interaction between magnetic moments and an external magnetic field is describable by substitution of the dipole moment $\vec{\mu}$ by two oppositely charged hypothetical magnetic monopoles of strength q_m with a distance of $\vec{d}_\mathrm{m}$ with

$$\vec{\mu} = q_\mathrm{m} \cdot \vec{d}_\mathrm{m} \quad [12, 13] \; . \tag{9}$$

If such a magnetic dipole composed of magnetic monopoles is placed in a uniform magnetic field $\vec{H}$ of strength $|\vec{H}| = H$, the force acting on each monopole is

$$\vec{F}_\mathrm{m} = q_\mathrm{m} \cdot \mu_0 \vec{H} \quad [13] \; . \tag{10}$$

It follows that the absolute values of the forces are equal for both monopoles but they possess opposite signs, which means the acting forces point in opposing directions, due to their opposite magnetic charges. Therefore, no effective translational force and acceleration occur. Instead, the interaction with the magnetic field, which encloses the angle θ with the dipole $\vec{\mu}$ or the distance $\vec{d}_\mathrm{m}$, manifests in the form of a torque $\vec{T}_\mathrm{m}$ of

$$\vec{T}_\mathrm{m} = -q_\mathrm{m} \cdot |\vec{d}_\mathrm{m}| \cdot \mu_0 |\vec{H}| \sin\theta = -q_\mathrm{m} \cdot \vec{d}_\mathrm{m} \times \mu_0 \vec{H} = -\vec{\mu} \times \mu_0 \vec{H} \quad [13] \; . \tag{11}$$

If friction is negligible, a potential energy landscape E_torque of the form

$$E_\mathrm{torque}(\theta) = -\vec{\mu} \cdot \mu_0 \vec{H} = -\mu \cdot \mu_0 H \cos\theta \quad [13] \tag{12}$$

results from the torque with θ being the angle between the dipole moment and the magnetic field [13]. This potential energy is called ZEEMAN energy and its landscape has an energetically favored minimum at a parallel alignment ($\theta_\mathrm{min} = 0°$) between dipole moment and externally applied field. For cases of a non-uniform magnetic field with a spatial gradient of $\nabla \vec{H} \neq 0$, the translational force

$$\vec{F}_\mathrm{m} = q_\mathrm{m} d_\mathrm{m} \cdot \nabla \vec{H} = \mu \cdot \nabla \vec{H} \tag{13}$$

accelerates the dipole towards the direction of increasing field strength [13].

Magnetic Dipole-Dipole Interaction

The magnetic dipole-dipole interaction, also called dipole coupling, describes the coupling between two magnetic dipoles via their magnetic fields. If two dipoles $\vec{\mu}_1$ and $\vec{\mu}_2$ are spatially separated by $\vec{r}$ from one another, a magnetostatic interaction with an energy E_{dipole} of

$$E_{\text{dipole}} = -\frac{1}{4\pi\mu_0|\vec{r}|^3}\left(3\cdot\frac{[\vec{\mu}_1\cdot\vec{r}]\,[\vec{\mu}_2\cdot\vec{r}]}{|\vec{r}|^2} - \vec{\mu}_1\cdot\vec{\mu}_2\right) \quad [13]\,, \tag{14}$$

takes effect via the magnetic fields arising from the two dipoles. This interaction ranges over larger distances and is steadily present in magnetic solid matter, in which the atomic magnetic dipole moments are in close vicinity to one another, predefined by the crystal structure. But this interaction is rather weak, compared to the other effects in this section. The relative spatial orientation of the dipole moments to each other is taken into account by the scalar products in Eq. (14). In the limiting case of ferromagnetic (parallel) or antiferromagnetic (antiparallel) arrangement (see section 2.1.3), the scalar products emerge to the product of their absolute values

$$E_{\text{dipole}} = \begin{cases} -\frac{|\vec{\mu}_1|\cdot|\vec{\mu}_2|}{2\pi\mu_0|\vec{r}|^3}\cos\Delta\beta, & \text{for ferromagnetic material} \\ +\frac{|\vec{\mu}_1|\cdot|\vec{\mu}_2|}{2\pi\mu_0|\vec{r}|^3}\cos\Delta\beta, & \text{for antiferromagnetic material}\,, \end{cases} \tag{15}$$

with $\Delta\beta$ as a small rotation angle between the dipole moments, including possible small mismatches or fluctuations in the arrangement [13].

Spin-Orbit Coupling

The spin-orbit coupling describes the coupling between the orbital angular momentum $\vec{l}_i$ and the spin angular momentum $\vec{s}_i$ by the spin-orbit interaction energy

$$E_{\text{so}} \propto \vec{s}_i \cdot \vec{l}_i \tag{16}$$

and thus governs their mutual arrangement and the formation of the total angular momentum $\vec{j}_i$. The origin of this spin-orbit-coupling is vividly explained by Bohr's semi-classical model [13]. An electron circulating the atomic nucleus experiences a relative rotational movement of the atomic nucleus in its inertial system, determined by the orbital momentum $\vec{l}_i$. Due to the rotation movement of the positively charged nucleus, the electron is exposed to a magnetic field of strength $H_{\text{nucl,l}}$, which interacts with the magnetic moment $\vec{\mu}_{\text{s}}$ possessed by the electron due to its intrinsic spin $\vec{s}_i$. The magnetic field is pointing along the orbital quantum number and thus, this interaction energetically favors an antiparallel arrangement of $\vec{l}$ and $\vec{s}$ [13].

This coupling is thereby mediated by the nucleus and its charge. More heavily charged atomic nuclei, i.e., heavier atoms, therefore, have stronger spin-orbit coupling in general. In the case of light atoms, which include most typical ferromagnetic materials [15], there is a weak, loose coupling, also called LS-coupling or RUSSEL-SAUNDERS-coupling, between the electron spins $\vec{s}_i$ and the orbital angular moments $\vec{l}_i$. Hereby, equations

$$\vec{L} = \sum_i \vec{l}_\mathrm{i}; \quad \vec{S} = \sum_i \vec{s}_\mathrm{i}; \quad \vec{J} = \vec{L} + \vec{S} \quad [13,\ 15]\ , \tag{17}$$

as described in section 2.1.1, hold true. The magnetic moment $\vec{\mu}_\mathrm{tot} = \vec{\mu}_\mathrm{L} + \vec{\mu}_\mathrm{S}$ and $\vec{J}$ are not aligned colinear to each other due to the g-factor of the electron spin $\vec{S}$, tilting $\vec{\mu}_\mathrm{tot}$ slightly towards it [15]. Hereby, $\vec{\mu}_\mathrm{tot}$ follows a precession movement around $\vec{J}$, in which only the component $\vec{\mu}_\mathrm{J}$ along $\vec{J}$ is observable on average over time. This component is determinable by the LANDÉ factor introduced in Eq. (8) [15].

In addition to the LS-coupling, there is also the jj-coupling. This describes the situation of strong spin-orbit interaction, so that the individual angular moments $\vec{l}_i$ and $\vec{s}_i$ of the electrons are no longer separable, i.e., can no longer be regarded as good quantum numbers and conserved quantities. In this case, the angular moment $\vec{j}_i$ is formed electron-specifically, resulting in

$$\vec{j}_i = \vec{l}_i + \vec{s}_i; \quad \vec{J} = \sum_i \vec{j}_i \quad [12]\ . \tag{18}$$

For this strong coupling to take place, a highly charged nucleus is crucial. Therefore, this coupling mechanism affects mainly heavy atoms, i.e., heavy metals [12]. Particularly important is, that with this coupling mechanism the electron spin is not a conserved quantity and its changes can be compensated for by changes in the orbital angular moments.

Direct Exchange Interaction

The direct exchange interaction also called HEISENBERG exchange interaction according to its discoverer, is a purely quantum mechanical effect [13]. Its quantum mechanical consideration is based on the PAULI exclusion principle affecting two electrons in close vicinity of each other.

The wave function of such a two-electron system is quantum mechanically described via the function $\Psi(\vec{r}_1, \vec{r}_2)$, in which $\vec{r}_1$ and $\vec{r}_2$ represent the respective coordinates of the two electrons. According to the approach of HEITLER and LONDON [12], this total wave function can be

described as a linear combination of the involved atomic wave functions

$$\Psi(r_1, r_2) = \begin{cases} \Psi_\mathrm{a}(\vec{r}_1) \cdot \Psi_\mathrm{b}(\vec{r}_2) & (\mathbf{I}) \\ \Psi_\mathrm{a}(\vec{r}_2) \cdot \Psi_\mathrm{b}(\vec{r}_1) & (\mathbf{II}) \\ \Psi_\mathrm{a}(\vec{r}_1) \cdot \Psi_\mathrm{b}(\vec{r}_2) + \Psi_\mathrm{a}(\vec{r}_2) \cdot \Psi_\mathrm{b}(\vec{r}_1) & (\mathbf{III}) \\ \Psi_\mathrm{a}(\vec{r}_1) \cdot \Psi_\mathrm{b}(\vec{r}_2) - \Psi_\mathrm{a}(\vec{r}_2) \cdot \Psi_\mathrm{b}(\vec{r}_1) & (\mathbf{IV})\,. \end{cases} \tag{19}$$

The indices a and b of the wave function represent the two different atoms and the indices 1 and 2 of the space coordinate describe which electron is under consideration. According to the indistinguishability of the electrons and the Pauli exclusion principle, the physical properties of the asymmetric wave function, given by $|\Psi(\vec{r}_1, \vec{r}_2)|^2$, must be preserved upon interchange of the electrons and additionally, the probability of both electrons occupying the same state ($\vec{r}_1 = \vec{r}_2$) has to be zero [12]. Solely the linear combination (**IV**) in Eq. (19) fulfills both of these conditions simultaneously. The energy of such a system amounts to the spatial integral over the total volumes τ_1 and τ_2:

$$E_\mathrm{tot} = \iint \Psi^*(\vec{r}_1, \vec{r}_2) \langle \mathcal{H} \rangle \Psi(\vec{r}_1, \vec{r}_2) \mathrm{d}\tau_1 \mathrm{d}\tau_2\,, \tag{20}$$

$$\text{with} \quad \langle \mathcal{H} \rangle = \langle \mathcal{H}_1 \rangle + \langle \mathcal{H}_2 \rangle + \langle \mathcal{H}_{1,2} \rangle\,. \tag{21}$$

The Hamiltonian operators $\langle \mathcal{H}_1 \rangle$ and $\langle \mathcal{H}_2 \rangle$ contain only the coordinates $\vec{r}_1$ and $\vec{r}_2$, respectively

$$\langle \mathcal{H}_1 \rangle = -\frac{\hbar^2}{2m}\Delta_1 - \frac{Ze^2}{4\pi\varepsilon_0 |\vec{r}_1|} \text{ and } \quad \langle \mathcal{H}_2 \rangle = -\frac{\hbar^2}{2m}\Delta_2 - \frac{Ze^2}{4\pi\varepsilon_0 |\vec{r}_2|}\,, \tag{22}$$

with the Laplace operator $\Delta_k = \frac{\partial^2}{\partial x_k^2} + \frac{\partial^2}{\partial y_k^2} + \frac{\partial^2}{\partial z_k^2}; k \in [1, 2]$ and the nucleus charge Z. The integral terms of these two Hamiltonian operators describe the atomically separated situation, while the integral term of $\langle \mathcal{H}_{12} \rangle$ represents the energy contribution of the interaction over the atomic distance $\vec{r}_{12}$ via

$$\langle \mathcal{H}_{12} \rangle = \frac{e^2}{4\pi\varepsilon_0 |\vec{r}_{12}|}\,, \tag{23}$$

$$E_{12} = \iint \Psi^*(\vec{r}_1, \vec{r}_2) \langle \mathcal{H}_{12} \rangle \Psi(\vec{r}_1, \vec{r}_2) \mathrm{d}\tau_1 \mathrm{d}\tau_2 = E_\mathrm{int} \iint \Psi^*(\vec{r}_1, \vec{r}_2) \Psi(\vec{r}_1, \vec{r}_2) \mathrm{d}\tau_1 \mathrm{d}\tau_2\,. \tag{24}$$

This interaction energy is further separable into one part E_Coulomb describing the electrons remaining at the same nucleus and a second part J_ex describing the exchange of electrons between the atoms [13]. While the first part

$$E_\mathrm{Coulomb} = \iint \{\Psi_\mathrm{a}^*(\vec{r}_1)\Psi_\mathrm{b}^*(\vec{r}_2)\} \langle \mathcal{H}_{12} \rangle \{\Psi_\mathrm{a}(\vec{r}_1)\Psi_\mathrm{b}(\vec{r}_2)\} \mathrm{d}\tau_1 \mathrm{d}\tau_2 \tag{25}$$

resembles a classical COULOMB interaction, the second part

$$J_{\mathrm{ex}} = \iint \{\Psi_{\mathrm{a}}^*(\vec{r}_1)\Psi_{\mathrm{b}}^*(\vec{r}_2)\}\langle\mathcal{H}_{12}\rangle\{\Psi_{\mathrm{a}}(\vec{r}_2)\Psi_{\mathrm{b}}(\vec{r}_1)\}\mathrm{d}\tau_1\mathrm{d}\tau_2 \tag{26}$$

results in an additional energy term with no classical analogs, since classical physics does not expect an energy difference upon the exchange of electrons. This energy term directly affects the ordering of the electron spins. Considering the spin wave function of the electrons $\xi(\vec{s}_1, \vec{s}_2)$, the total wave function is

$$\Psi_{\mathrm{tot}} = \Psi(\vec{r}_1, \vec{r}_2) \cdot \xi(\vec{s}_1, \vec{s}_2)\,, \tag{27}$$

whereby the spin wave function can be expressed as a linear combination of the single spin wave functions $\xi_{\mathrm{a}}(\vec{s}_1)$, $\xi_{\mathrm{b}}(\vec{s}_1)$, $\xi_{\mathrm{a}}(\vec{s}_2)$, and $\xi_{\mathrm{b}}(\vec{s}_2)$ analogously to Eq. (19). The spin wave function is either symmetric (parallel spin arrangement) or antisymmetric (antiparallel spin arrangement) and thereby compensates the symmetry of the wave function $\Psi(\vec{r}_1, \vec{r}_2)$ guaranteeing an asymmetric overall wave function Ψ_{tot}, effectively shifting the asymmetric wave function condition for the interchangeability of electrons to the spin function.
This enables the reformulation of the Hamiltonian $\langle\mathcal{H}_{12}\rangle$ of the exchange integral in Eq. (26) in terms of the spins

$$\langle\mathcal{H}_{12}\rangle = -2J_{12}\frac{1}{\hbar^2} \cdot \vec{s}_i \cdot \vec{s}_j = -2J_{12}s^2 \cdot \cos\theta\,. \tag{28}$$

For a parallel arrangement of the spins $\cos(\theta = 0°) = 1$, the scalar product of these is positive and for their antiparallel arrangement $\cos(\theta = 180°) = -1$ it is negative, resulting in a ferromagnetic (parallel) arrangement for a positive exchange constant $J_{\mathrm{ex}} > 0$ and an antiferromagnetic (antiparallel) arrangement for a negative exchange constant $J_{\mathrm{ex}} < 0$. This exchange term is directly dependent on the distance between the nuclei $\vec{r}_{12}$, transforming the sign condition into a distance dependence in the so-called BETHE-SLATER curve. This curve displays ferromagnetic (positive region) and antiferromagnetic (negative region) coupling in dependence on the atomic distance.
In crystals, the many-electron system is treated as the sum of all the i and j pairs of electrons, whereby this is mostly restricted to the nearest neighbors [14]. The exchange stiffness

$$A_{\mathrm{ex}} = \frac{n\langle S^2\rangle}{a} \cdot J_{\mathrm{ex}} \tag{29}$$

is introduced as a practical variable, whereby n represents the lattice symmetry ($n = 1$ for simple cubic, $n = 2$ for bcc, and $n = 4$ for fcc) and a the lattice constant. It, therefore,

resembles a one-dimensional energy density originating from the average of exchange integrals in Eq. (26) with the nearest neighbors. The samples to investigate possess an exchange stiffness of around $A_{\mathrm{ex}} = 1.6 \cdot 10^{-11}\,\mathrm{J/m}$ [16].

Other Exchange Interactions

Besides the aforementioned exchange mechanisms, there are further mechanisms like the implicit exchange interactions according to Kondo or RKKY (Ruderman-Kittel-Kasuya-Yoshida) treating the materials respond to localized magnetic perturbations in the form of a damped oscillatory variation of polarization [13].

Another quantum mechanical interaction between dipole moments, which, contrary to the direct exchange interaction, does not involve a direct overlap of the wave functions is the indirect exchange interaction. The hopping model, in which an energetic balance between Coulomb repulsion and delocalization of the electrons is considered, is capable of explaining this mechanism.

The last exchange mechanism to be mentioned here is the so-called antisymmetric exchange interaction or Dzyaloshinskii-Moriya interaction (DMI). This exchange interaction is mediated by a third partner and is characterized by requiring a non-centrosymmetry of the system [1, 2]. Since this exchange mechanism is the basis of this work, the complete section 2.3 is dedicated to it.

2.1.3 Magnetism in Matter

This section deals with the magnetic responses of materials, primarily solids. Magnetic responses refer to the material's behavior during and after exposure to an external magnetic field $\vec{H}$. Based on this behavior, the materials are classified into the magnetic groups of diamagnetism, paramagnetism, ferromagnetism, antiferromagnetism, and ferrimagnetism.

The magnetic response manifests as the field-dependent magnetization $\vec{M}(\vec{H})$ of the material, in the following stated as $\vec{M}$, which specifies the average density and direction of magnetic moments in the matter. Magnetization also contributes to the overall strength of the magnetic field. Therefore, the magnetic field flux density or magnetic induction referring to the superimposed sum of all magnetic contributions in space is introduced. It is thus given by

$$\vec{B} = \mu_0 \cdot \left(\vec{H} + \vec{M}\right) \quad [14] \tag{30}$$

inside of materials with magnetization $\vec{M}$. In a vacuum, this equation simplifies to equation $\vec{B} = \mu_0 \cdot \vec{H}$. Since the magnetization of the material represents its response to an external

magnetic field, its relation is expressed via the material-specific susceptibility χ as ratio coefficient via

$$\vec{M} = \chi \vec{H} \leftrightarrow \chi = \frac{\vec{H}}{\vec{M}} \quad [14] \; . \tag{31}$$

Applying the expression in Eq. (31) to Eq. (30) and the relative $\mu_r = 1 + \chi$ yields

$$\vec{B} = \mu_0 \cdot \left(\vec{H} + \chi \vec{H} \right) = \mu_0 \cdot (1 + \chi) \, \vec{H} = \mu_0 \cdot \mu_r \cdot \vec{H} \, . \tag{32}$$

The materials are classified according to their susceptibility χ into the mentioned classes. An essential difference between the first two classes of dia- and paramagnetism and the other classes is the susceptibility, which is constant with the external field $\frac{\mathrm{d}\chi}{\mathrm{d}\vec{H}} = 0$, originating from independent individual magnetic moments. According to this, the magnetization depends linearly on the external magnetic field and is $\vec{M}(\vec{H} = 0) = 0$ in the absence of the external magnetic field and independent of the history, i.e., the pretreatment, of the material. The other three classes describe the collective phenomena of magnetic moments, mediated by the interactions in section 2.1.2.

Uncoupled Magnetism

Materials with uncoupled or no permanent magnetic moments of electrons possess constant susceptibility, allowing a distinction between the two different cases of the susceptibility being either negative or positive.

Diamagnetism

For a negative susceptibility $\chi < 0$, the material's magnetization opposes the external magnetic field, meaning that the magnetization $\vec{M}$ is oriented antiparallel to the external field $\vec{H}$. This case is called diamagnetism and its small susceptibility is usually in the range of $\chi \approx -10^{-5}$ since diamagnetic materials do not contain magnetic moments [13, 14]. The opposing reaction of diamagnetic materials is based on the mechanism of electromagnetic induction of the external field on the orbital electrons, accelerating these. According to Lenz law, the magnetic dipoles induced by this acceleration are opposing its origin, i.e., the external magnetic field [13]. In principle, this mechanism occurs in all matters. However, in the presence of permanent magnetic moments, this mechanism is overshadowed by the interactions affecting these [13, 14].

Paramagnetism

The case of uncoupled magnetic moments in a material is called paramagnetism and is characterized by a constant, positive magnetic susceptibility $\chi > 0$ in the order of $10^{-5} < \chi < 10^{-2}$ [13]. In principle, the coupling mechanisms, discussed in section 2.1.2, also apply to the magnetic moments. In paramagnetic materials, however, the individual moments are separated from one another over a sufficiently large spatial distance so that their interaction is not appreciable and they are considered independently from one another [13]. An independent magnetic moment $\vec{\mu}$ tends to align itself with the external magnetic field $\vec{H}$ to minimize its free energy given by the ZEEMAN-energy

$$E_{\text{zeeman}} = -\vec{\mu} \cdot \mu_0 \vec{H} = -\mu \cdot \mu_0 H \cdot \cos\theta \quad [13] \; . \tag{33}$$

In addition, there are thermal fluctuations due to the thermal energy, which is usually above the ZEEMAN potential field energy at room temperature and contributes to a statistically distributed, non-directional magnetization [13]. Since these two energy terms counteract each other in the alignment of magnetic moments, the susceptibility has a reciprocal dependence on the absolute temperature according to CURIE's law

$$\chi_{\text{para}} \propto \frac{1}{T} \quad [13, 12, 14] \; . \tag{34}$$

On average over time, the fluctuating N_0 dipole moments contribute to the magnetization along the external magnetic field via

$$\vec{M} = N_0 \cdot \vec{\mu} \cdot \langle \cos\theta \rangle \, , \tag{35}$$

whereby $\langle \cos\theta \rangle$ is the time-averaged orientation angle whose distribution follows the BOLTZMANN distribution [14] and N_0 is the density of magnetic moments.

Collective Magnetism

Collective magnetism refers to materials with strong connections between their magnetic moments, mediated by the interaction mechanisms in section 2.1.2. Directly affecting a single moment influences all other magnetic moments or at least the one in its immediate vicinity may result in ordered magnetic structures. The most important interaction here is the strong direct exchange interaction, which arises the difference between ferromagnetism with parallel coupled magnetic moments and antiferromagnetism and ferrimagnetism with antiparallel coupled magnetic moments. For all three cases, the collective behavior only occurs below

a characteristic temperature, which is the CURIE temperature T_C in the case of ferromagnetism and the NÉEL temperature T_N in the case of antiferromagnetism and ferrimagnetism. Above this temperature, the collective behavior disappears and all these types of collective magnetism transition to paramagnetic behavior. Additionally, the collective behavior alters the relationship in Eq. (31) into a non-linear equation with $\frac{\partial \chi}{\partial \vec{H}} \neq 0$.

Ferromagnetism

The minimization of the energy in the potential of the external magnetic field according to ZEEMAN and its counteracting phenomenon of thermal fluctuations known from paramagnetism also applies to ferromagnetic materials. In this case, however, the coupling of the magnetic moments among one another must also be taken into account, which, essentially consists of strong direct exchange interaction. This interaction can be understood as an internal molecular field [14], which aligns the magnetic moments in addition to the external field and also in its absence. Considering its energy term in Eq. (28), the exchange energy E_ex of a magnetic moment $\vec{\mu}_i$ with spin $\vec{s}_i$ with z closest neighbors is

$$E_\mathrm{ex} = -2J_\mathrm{ex}\vec{s}_i \cdot \sum_j^z \vec{s}_j = -2zJ_\mathrm{ex}\vec{s}_i\langle\vec{s}_j\rangle \quad [13,\, 14] \tag{36}$$

with a magnetization $\vec{M}$ of

$$\vec{M} = -N_0 g\mu_\mathrm{B}\frac{1}{\hbar}\langle\vec{s}_j\rangle \quad [13,\, 14] \tag{37}$$

following Eq. (6), if the magnetic moments solely originate from spins. Combining both equations over $\langle\vec{s}_j\rangle$ results in

$$E_\mathrm{ex} = -\left(-g\mu_\mathrm{B}\frac{1}{\hbar}\vec{s}_i\right)\cdot\frac{2zJ_\mathrm{ex}}{N_0 g^2\mu_\mathrm{B}^2}\vec{M} = -\vec{\mu}_i\cdot\vec{B}_\mathrm{ex} \tag{38}$$

$$\text{with} \quad \vec{B}_\mathrm{ex} = \frac{2zJ_\mathrm{ex}}{N_0 g^2\mu_\mathrm{B}^2}\vec{M} \quad [13,\, 14]\,. \tag{39}$$

This internal molecular field amplifies the external field

$$\vec{B}_\mathrm{eff} = \vec{B}_0 + \vec{B}_\mathrm{ex}\,. \tag{40}$$

The molecular field $\vec{B}_\mathrm{ex}$ depends on the already existing order via $\langle\vec{s}_j\rangle$ and thus on the history and the pre-treatment of the material. This results in the dependence of the susceptibility $\chi(\vec{H}, \vec{M}, T)$ on the magnetization $\vec{M}$ or its history, which is expressed in more complex curves for the projection of the magnetization against an external magnetic field. In general, these curves reflect the direction- and pre-treatment-dependent (history) macroscopic behavior of

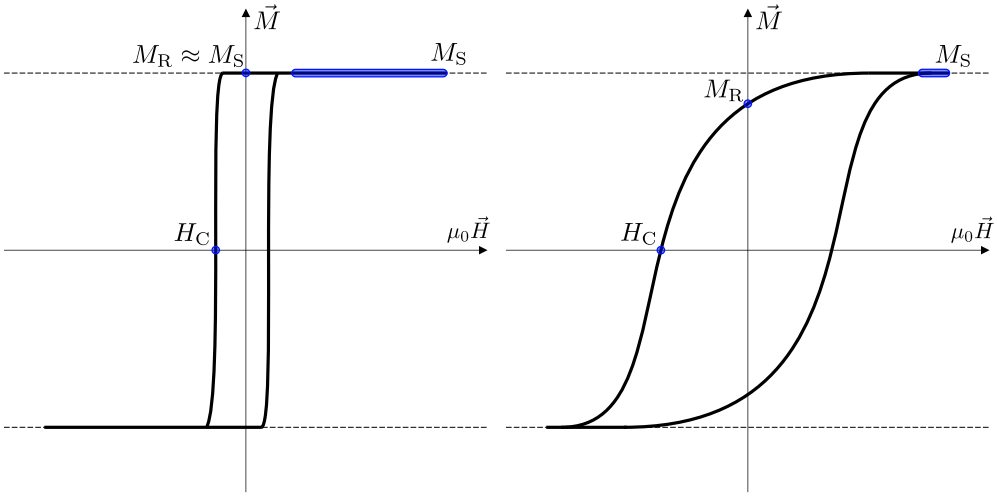

(a) Hysteresis curve along an easy axis.

(b) Hysteresis curve along a hard axis.

Figure 1: Schematic illustration of the hysteresis curves of the multi-domain samples of this work along an easy axis in 1a and along a hard axis in 1b. The most important quantities, the saturation magnetization M_S, the remanent magnetization M_R and the coercive field H_C are depicted for both cases. The hard axis is characterized by a larger coercive field, a smaller remanence, and a larger enclosed area. Adapted from [14] and measurements in appendix section 9.2.

a ferromagnet to an external magnetic field and are referred to as hysteresis curves [13, 14]. This behavior is limited to a field range up to which all magnetic moments are aligned parallel to the external magnetic field, reaching saturation magnetization M_S, the maximum magnetization of the sample. For the samples of interest, the saturation magnetization is expected to be around $M_\mathrm{S} = 600\,\mathrm{kA\,m^{-1}}$ [16]. Above the saturation magnetization, $\chi \simeq 0$ applies and the magnetization remains approximately constant. If an ordered state like the saturation magnetization is reached, a residual magnetization at $B_0 = 0$ remains, which is referred to as remanence magnetization $M_\mathrm{R} \neq 0$. At the beginning of a magnetization reversal process along one magnetic field axis, $\vec{B}_\mathrm{ex}$ and $\vec{B}_0$ are oriented antiparallel to each other and the external field must first overcome the internal one. For this reason, the so-called coercive field $|H_\mathrm{C}| > 0$ is required to reach the state of no magnetization $\vec{M} = 0$ again. In addition, (limited) information about magnetization dynamics can be extracted from the hystereses, e.g., its gradients, enclosed loop, or characteristic quantities. Magnetization reversal processes include coherent rotation of the magnetization, nucleation of magnetic domains with the consecutive movement of domain walls, and spin flipping. Domains are individual areas with $|\vec{M}| = M_\mathrm{S}$, which are separated from one another by domain walls. The total magneti-

zation of the sample results from the size and directional distribution of these domains (c.f., section 2.2). Each of these mechanisms affects the slope of the hysteresis, i.e., χ, differently. Spin flipping is associated with abrupt, coherent rotation with gradual changes. Nucleation and domain wall movement require sufficient field strengths associated with energy barriers and appear less abrupt in the hysteresis curve than spin flipping [17].
In addition, there is a directional dependency for the hysteresis and the magnetization processes, which origins are treated in section 2.1.4. The discussed approach assumes localized magnetic moments, i.e., localized electrons as their origin. This neglects the mostly metallic character of ferromagnetic materials, for which delocalized conducting electrons are assumed in the band model. These also contribute to the ferromagnetic behavior and are responsible for some effects such as the GMR (giant magnetoresistance). In the context of this work, however, these effects play no considerable role, and therefore the discussed model of localized magnetic moments is expected to be sufficient.

Antiferromagnetismus and Ferrimagnetismus

As discussed in the section on direct exchange interaction 2.1.2, there exists parallel and antiparallel coupling, depending on the distance of the magnetic moments. Therefore, in addition to ferromagnetism, materials with coupled magnetic moments can also show antiparallel coupled magnetic moments, which are referred to as antiferromagnetic if the magnetic moments cancel each other out completely and ferrimagnetic when net magnetic moments remain. Antiferromagnetic materials possess a susceptibility of the same magnitude as paramagnetic materials [13]. Ferrimagnetic materials possess similar but weakened properties compared to ferromagnetic materials. Since there are no antiferromagnetic or ferrimagnetic materials in the material system under investigation, its properties will not be discussed further here.

2.1.4 Magnetic Anisotropy Effects

In ferromagnetic samples, the magnetic properties possess an anisotropy, i.e., they, as well as the free magnetic energy, vary depending on the observed direction [13, 14]. In the sample material, there are energetically preferred spatial orientations (easy axes) of the magnetic dipoles arising from the sample composition, its crystalline structure, sample geometry, and surface as well as other external impacts. For shifting the magnetization towards less favored axes appropriately oriented external magnetic fields are required. The energetically least

favorable axes are refereed to as the hard axis. The magnetic anisotropy is usually described by the difference in the energy density $F_{\text{anis}} = F_{\text{hard}} - F_{\text{easy}}$ between the free energy of the easy axis F_{easy} and the free energy of the hard axis F_{hard} as well as the number of hard and easy axes, i.e., the symmetry of the anisotropy. The anisotropy is usually expressed as a density by reducing it to the volume V via $f_{\text{anis}} = \frac{F_{\text{anis}}}{V}$. The total magnetic anisotropy results as the sum of the individual anisotropy contributions. These contributions are discussed in detail below.

Magnetocrystalline Anisotropy

The magnetocrystalline anisotropy is a crystallographic contribution of the sample's crystalline structure to its anisotropy. The symmetry of the magnetocrystalline anisotropy directly reflects the crystalline symmetry, which follows from the origin of this anisotropy [13]. Since all spins rotate collectively with the magnetization, $\theta = 0°$ in Eq. (28) remains true and the exchange interaction is invariant in rotation and thus isotropic. Instead, the magnetocrystalline anisotropy directly emerges from the comparable weak spin-orbit coupling (see section 2.1.2) [13, 14]. Upon rotation of the spins, interconnected by the strong exchange interaction, these exert a torque on the orbital momentum, mediated by this weak spin-orbit coupling. This torque in turn causes a rotation of the orbital momenta. If electrons occupy anisotropic orbitals, like d- and f-orbitals of transition elements, this rotation changes the effective overlap of the electron wave functions and thus indirectly also the otherwise isotropic exchange interaction.

Due to insufficient theoretical description, magnetocrystalline anisotropy is often described by employing an empirical, phenomenologically appropriate power series of the directional cosines α_i. The directional cosines indicate the direction of the magnetization in Cartesian space in the form of the angle enclosed between the magnetization $\vec{M}$ and the respective unit vector $\vec{e}_i$. It is implied that this power series is invariant for the symmetry operations of the crystal lattice, which is often accompanied by a reduction of coefficients, simplifying the power series [14]. Albeit deriving the magnetocrystalline anisotropy typically in terms of the directional cosines in the Cartesian coordinate system, they are often described via the polar angle θ and the azimuth angle φ after reduction via the symmetry operations.

In the investigated ferromagnetic material, a cubic crystal lattice (nickel [14, 12]) and a hexagonal crystal lattice (cobalt [14, 12]) occur in spatially separated areas (see Fig. 3). The

phenomenological power series of these crystal structures are given by [14]

$$f_{\text{cubic}} = K_1 \left(\alpha_1^2\alpha_2^2 + \alpha_2^2\alpha_3^2 + \alpha_1^2\alpha_3^2\right) + K_2\alpha_1^2\alpha_2^2\alpha_3^2 + \ldots \tag{41}$$

$$f_{\text{hex}} = K_1 \sin^2\theta + K_2 \sin^4\theta + K_3 \sin^6\theta + K_4 \sin^6\theta \sin^6\phi + \ldots . \tag{42}$$

Note, that the magnetocrystalline anisotropy of the cubic crystal structure is given in the directional cosines α_1, α_2, and α_3 of the crystal orientations while the anisotropy of the hexagonal crystal structure is given in the polar coordinates θ and ϕ. This inconsistent specification originates in the crystal-specific choice of the coordinate system to describe the anisotropy in the most convenient way [14]. The neglected zeroth term of the power series is constant and has therefore no impact on the directional dependency.

As mentioned, the total anisotropy of a sample results from the superposition of all anisotropy contributions, which also applies to the two different crystal anisotropies of nickel and cobalt. The previously discussed magnetocrystalline anisotropy considers monocrystalline ferromagnets, whereby polycrystalline material is expected in the thin film samples here. In a polycrystalline sample, the magnetocrystalline anisotropy results from the contributions of the individual grains depending on their size and crystal orientation, largely averaging the magnetocrystalline anisotropy to zero if no preferential crystal orientation exists. The remaining anisotropy is considered, for example, by the random anisotropy model [18].

Shape Anisotropy

The shape anisotropy arises from the long-ranging magnetic dipole-dipole interaction (see section 2.1.2). Uncompensated magnetic moments on surfaces and interfaces, given by the macroscopic shape, as well as inhomogeneous magnetization, result in stray fields outside of the sample volume, which provide an additional energy contribution. The strength and thus also the energy of the stray fields depends on the relative alignment between the magnetization $\vec{M}$ and the surface normal $\vec{n}$, which results in preferred alignments of the magnetization by minimizing the energy of the stray fields. For an idealized thin film with infinite lateral extent, the energy density of the stray field landscape is given by

$$f_{\text{shape}} = -\frac{1}{2} \cdot \mu_0 \cdot M_{\text{S}}^2 \cdot \cos^2\theta \quad [14] \ . \tag{43}$$

with M_{S} as the saturation magnetization and θ as the angle between the surface normal and magnetization [14]. With an angle of $\theta = 90°$, i.e., a magnetization inside of the thin film plane, this energy density results in its minimum of $f_{\text{shape}}(\theta = 90°) = 0$. Accordingly,

the geometry of the thin film favors one direction of magnetization in the film. For the calculation of this anisotropy component, the equally strong demagnetization field inside the sample is often used instead of the stray field. The demagnetization field is mathematically more convenient due to the spatial limitation of the sample volume.

Surface Anisotropy and Ultra-Thin Films

In addition to the shape anisotropy based on dipole-dipole interaction, a second effect occurs on surfaces. This is based on the surface states to be found there, which have different properties than the states inside the volume due to the broken translational invariance [14]. It especially concerns the orbital moments of surface states. For a thin film with a thickness of t and two surfaces, this surface anisotropy f_{Surf} contributes to the overall anisotropy via

$$f_{\mathrm{Surf}} = \frac{2}{t} K_{\mathrm{Surf}} \sin^2\theta \quad [19] \; . \tag{44}$$

Since this contribution concerns surface A, it is expanded by $\frac{t}{t}$ to be able to be related to volume $V = A \cdot t$. As a result, this contribution to the energy density of the anisotropy possesses a reciprocal dependency on the layer thickness t, whereby this uniaxial anisotropy becomes increasingly important with decreasing layer thickness. Depending on the changes in the surface states, this anisotropy may favor an out-of-plane anisotropy ($K_{\mathrm{Surf}} > 0$) or an in-plane anisotropy ($K_{\mathrm{Surf}} < 0$) [19].

By defining the anisotropy energy along the surface normal to $f(\theta = 0°) = 0$, the anisotropy in the sample surface is, according to [19, 20], given by

$$K_{\mathrm{eff}} = K_{\mathrm{V}} + \frac{2}{t} K_{\mathrm{Surf}} \, , \tag{45}$$

where K_{V} represents the constant combination of all volume anisotropies and is always negative due to the shape anisotropy preferring an in-plane alignment. If the surface anisotropy favors an out-of-plane anisotropy ($K_{\mathrm{Surf}} > 0$), there is a critical layer thickness $t_{\mathrm{crit}} = 2K_{\mathrm{Surf}}/|K_{\mathrm{V}}|$ with $K_{\mathrm{eff}} = 0$. For every layer thickness below t_{crit}, the effective anisotropy constant in-plane is positive relative to the out-of-plane (oop) anisotropy, meaning that the sample has effectively an out-of-plane easy axis. For all larger layer thicknesses or $K_{\mathrm{Surf}} < 0$, the thin film sample possesses an in-plane (ip) easy axis.

For the ultra-thin film samples considered here, the layer thickness is severely below its critical value, resulting in an effective out-of-plane anisotropy with $K_{\mathrm{eff}} = 2 \cdot 10^5 \, \mathrm{J\,m^{-3}}$ [16]. The easy axis is thus collinear with the surface normal and the anisotropy can be expressed as

$$f^3_{\mathrm{anis}} = K_1 \cdot \sin^2\theta + K_2 \cdot \sin^4\theta + K_3 \cdot \sin^4\theta \cos 4\varphi \quad [15] \tag{46}$$

in polar coordinates. Hereby, the equation represents the power series developed up to the third coefficient K_3. The neglected zeroth term of the power series is constant and has therefore no impact on the directional dependency.

In [9], a correlation between the effective anisotropy constant K_{eff} and the out-of-plane anisotropy constant K_{oop}, is given by

$$K_{\text{eff}} = K_{\text{oop}} - \frac{\mu_0 M_{\text{S}}^2}{2} \quad [9] \ . \tag{47}$$

The separation in this equation is for example important for a model of domain growth in dependence of the domain wall in Tab. 2. Since the anisotropy contributions are difficult to separate from one another experimentally [13], the experiments carried out here determine the effective anisotropy K_{eff} directly.

Further Anisotropies

With the magnetocrystalline, the shape, and the surface anisotropies, the most important magnetic anisotropy contributions for the samples examined here are completed. In addition to these, there are further contributions that may have an impact on the overall anisotropy. There is magnetoelastic anisotropy describing the change in the free energy of remagnetization upon elastic deformation of ferromagnetic materials [13, 14]. Its inverse effect, the deformation via changes in the magnetization direction is called magnetostriction.

The second effect, the so-called exchange bias anisotropy, arises from a ferromagnetic surface coupling with an antiferromagnetic surface. This contribution has a special characteristic compared to the hitherto mentioned anisotropies, since it does not cause an axial anisotropy like the others, but a unidirectional anisotropy. This unidirectional anisotropy can be used, for example, to produce magnetic samples that have a constant direction of magnetization in the absence of an external magnetic field, regardless of their pretreatment [14].

Other, more exotic anisotropies are caused, for example, by preferential crystal growth or surface roughness and structures [21]. It is also possible to induce anisotropies, for example, by thermal annealing or photon irradiation [13].

2.2 Magnetic Domains and Domain Walls

In ferro- and ferrimagnetic materials domains are formed as magnetic microstructures [21]. The domains are spatially confined volumes of uniform magnetization with domain-specific orientation, separated by domain walls [13] and they result from the minimization of energy, especially the magnetostatic energy of the stray field, which energy density is given by

$$\varepsilon_{\text{stray}} = -\mu_0 \cdot \vec{H}_{\text{stray}} \cdot \frac{\vec{M}}{2} \,. \tag{48}$$

The term $\vec{H}_{\text{stray}}$ denotes the field strength of the stray field emerging from the sample. Additionally, within a domain, the magnetization is saturated with $|\vec{M}| = M_{\text{S}}$. The total energy density also includes the already mentioned exchange energy ε_{ex} , the anisotropy energy $\varepsilon_{\text{anis}} = f_{\text{anis}}$, and the ZEEMAN energy $\varepsilon_{\text{zeeman}}$. The exchange energy favors parallel alignment of all dipole moments in ferromagnets, the anisotropy energy favors alignment along certain sample axes and the ZEEMAN energy favors alignment along an external field. The magnetization of the domains aligns according to these first three energy contributions. In general, the stray field energy is proportional to the volume of the causative domain [14]. A reduction in volume is thus accompanied by an energy reduction. Simultaneously, decreased domain volumes lead to an increase in the interface area of domains, the so-called domain walls. In these domain wall regions, a rotation between the magnetization of the enclosing domains takes place, which is accompanied by an increase in energy due to the broken anisotropy and exchange interaction contributions.

The concurrent reduction in the stray field landscape and the increase in the domain wall energy results in the micromagnetic structures known as domains [14]. Depending on the sample properties, the balancing of both energy contributions may be very complex and result in many different domain patterns and types [14, 21].

2.2.1 Magnetic Domains

Due to the perpendicular magnetization anisotropy of the thin film samples, the magnetization of the domains to be observed is either parallel or antiparallel to the sample surface normal. Two possibilities for domain patterns in such samples are the cylindrical bubble domains or domain stripes [21, 9]. The formation of bubble domains requires a quite large perpendicular magnetization anisotropy which has to fulfill condition

$$K_{\text{eff}} \geq \frac{1}{2} \cdot \frac{M_{\text{S}}^2}{\mu_0} \quad [21] \,. \tag{49}$$

Lower perpendicular magnetic anisotropies, which do fulfill Eq. (49) on the other hand, lead to stripe domains, which can also be observed here in the experiments (see Fig. 5). The stripe domains that can be observed here are highly branched, which are therefore also referred to as maze stripe domains, labyrinth domains or dendrimeric domains [16]. The individual branch ends can be assumed to be hemispheres or half bubbles [16].

2.2.2 Bloch and Néel Domain Walls

In the intermediate area between two domains, the magnetization changes by the rotation of the magnetic moments in this area. Since only perpendicularly oriented domains occur here, the walls are planar 180° walls according to the angle of rotation. There are two different possibilities for rotation [14]:

1. Néel domain wall with a rotation along an axis parallel to the domain wall
2. Bloch domain wall with a rotation along an axis perpendicular to the domain wall.

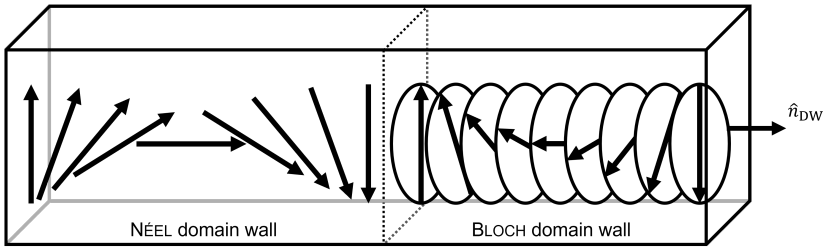

Figure 2: Schematic illustration of the two different kinds of domain walls, based on [21]. In the Néel domain wall, the magnetic moments (black arrows) rotate along a plane parallel to the domain wall normal $\hat{n}_{\mathrm{DW}}$, and in the Bloch domain wall, they rotate in a plane perpendicular to the domain wall normal $\hat{n}_{\mathrm{DW}}$. The latter is highlighted with rotating discs to increase visualization of the rotation axis.

In general, Bloch walls are energetically favored in bulk materials. However, in thin films like the ones here, a Bloch domain wall causes the magnetization to leak from the sample surface and thus an additional contribution of energy via the stray field appears. This favors Néel walls as layers become thinner. In addition to this, the Dzyaloshinskii-Moriya interaction, which has not yet been discussed, also promotes Néel walls [9] and therefore only domain walls are to be expected in the samples considered [22, 23, 16].
The energy density σ of a Néel domain wall with associated DMI, giving rise to an internal in-plane field H_{DMI}, is

$$\sigma(H_x, \psi) = \sigma_0 + 2K_{\mathrm{D}}\lambda\cos^2\psi - \pi\mu_0 M_{\mathrm{S}}\lambda\,(H_x + H_{\mathrm{DMI}})\cos\psi \quad [9]\ . \tag{50}$$

In this equation K_D is the energy density of the domain wall associated with the anisotropy and ψ is the angle enclosed by the domain magnetization direction $\vec{M}$ and the external magnetic field $\vec{H}_x$ in-plane. The term σ_0 summarizes all energetic quantities independent from an external in-plane field and λ describes the 180°-domain width via

$$\lambda = \sqrt{\frac{A_\mathrm{ex}}{K_\mathrm{eff}}} \quad [9] \ . \tag{51}$$

The relation given in Eq. (51) is an estimation of the domain wall width based on the two energy contributions of the exchange stiffness A_ex and the effective crystal anisotropy K_eff, which affect the rotation of magnetic moments in the domain walls [21]. However, it is an approximation, since this equation is considering Bloch domain walls.

2.3 Dzyaloshinskii-Moriya interaction DMI

The Dzyaloshinskii-Moriya interaction (DMI), also called antisymmetric exchange interaction, describes a form of exchange interaction that energetically favors canted, i.e., non-collinear, alignment of adjacent spins and thus differs strongly from Heisenberg's direct exchange interaction with parallel and antiparallel alignment. This interaction enables or rather stabilizes many exotic topological structures such as skyrmions or chiral domain walls [9, 3]. The energy of this interaction can be calculated based on the Hamilton operator

$$\mathcal{H}_\mathrm{DMI} = \vec{D}_{ij} \cdot (\vec{s}_i \times \vec{s}_j) \quad [2, 9] \ . \tag{52}$$

Moriya treated this antisymmetric exchange interaction as a combination of spin-orbit coupling and exchange interaction [2] and resulting in the expression in Eq. (52) which thus scales linearly with the spin-orbit coupling [2].

For this anisotropic interaction to be non-zero, the sample to be investigated has to possess low symmetry, which especially refers to a broken inversion symmetry [2]. The magnitude of the contribution to the isotropic interaction can be estimated using $\frac{g-2}{g}$ [2]. Phenomenologically, this interaction was already postulated by Dzyaloshinskii before Moriya [1, 2] in the form of parasitic ferromagnetism in antiferromagnetic materials. Dzyaloshinskii already attributed this to the broken symmetry but was not yet able to explain it [1].

The vector $\vec{D}_{ij}$ tends to align along the crystallographic axes and its sign determines the chirality of chiral objects [9].

2.3.1 Interfacial DMI

The original papers by Dzyaloshinskii [1] and Moriya [2] solely assume samples in which the inversion symmetry is broken on an atomic level, i.e., in the unit cells of the crystal structure, resulting in $\mathcal{H}_{\mathrm{DMI}} \neq 0$ and hence an effective DMI. Recent investigations show that the DMI can also occur via a macroscopically broken inversion symmetry, for example through an antisymmetric arrangement of layers in a multilayer system [9]. In such samples, the DMI may occur as an interface coupling phenomenon between a ferromagnetic layer (FM) and a heavy metal layer (HM) with strong spin-orbit coupling [9]. Such an interfacial DMI is shown schematically for the FM/HM interfaces in the samples here in Fig. 4.

In such a case of interfacial DMI, the vector $\vec{D}_{ij}$ can be reduced to an interface and material-specific single scalar DMI value $\vec{D}_{ij} = D$ [9]. With $D < 0$, left-handed Néel domain walls are favored, while $D > 0$ favors right-handed Néel domain walls. In the asymmetric bubble expansion technique experiment, which has not yet been discussed, a positive D manifests as an increase in domain wall velocity along the external magnetic field for a background saturation antiparallel to the surface normal [9].

Thereby, the DMI is describable as an additional in-plane field, affecting domain walls and their energy density (see Eq. (50)). The DMI can be calculated as follows, with a more detailed description following in section 3.2.3

$$|D| = \left| \mu_0 \cdot H_{\mathrm{DMI}} \cdot M_{\mathrm{S}} \cdot \sqrt{\frac{A_{\mathrm{ex}}}{K_{\mathrm{eff}}}} \right| . \tag{53}$$

This equation provides the basis for the evaluation of this work, as it describes the dependence of the DMI D on the important quantities H_{DMI}, M_{S}, A_{ex}, and K_{eff}. Except for the exchange stiffness A_{ex}, these variables are determined depending on the ion bombardment to quantify the DMI and its modification by the ion bombardment. For the determination of the exchange stiffness mostly experimental setups and methods for interaction with spin-waves are required, which are not possible at the University of Kassel. For this reason, only a literature value is used for the exchange stiffness, which is introduced in sections 2.1.2 and 2.4.

Negative signs of the DMI correspond to counterclockwise (ccw, left-handed) domain walls, while positive signs suggest a clockwise (cw, right-handed) domain walls [9]. The sign of the DMI is also directly observable in the asymmetric bubble expansion technique [9] which will be introduced in section 3.2.3.

2.4 Multilayered Thin Film Material System

The investigated samples consist of a $[Pt/(Ni/Co)_3/Ir]_2$-multilayered thin film material system with nominal layer thicknesses in the sub-nm range with Fig. 3 schematically displaying the sequence of layers and their nominal thicknesses. The layer system was fabricated and provided by the group of Material Science and Engineering at Carnegie Mellon University (CMU) [23]. The multilayer system consists of triple alternating sequences of

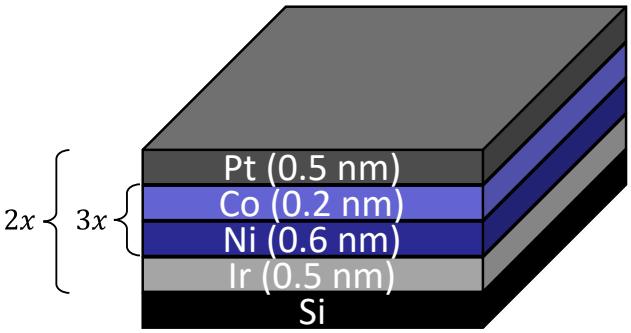

Figure 3: Schematic illustration of the nominal $[Pt/(Ni/Co)_3/Ir]_2$-multilayered thin film system provided by the group Material Science and Engineering at the CMU university [23].

ferromagnetic cobalt and nickel layers, which are enclosed by a platinum layer on top and an iridium layer underneath. Two of these enclosed subsequences with structural inversion asymmetry are stacked on top of each other.

The layers consisting of platinum or iridium are heavy metals with large spin-orbit coupling, which, as described in section 2.3, result in an interfacial DMI $\vec{D}_{ij}$ as schematically depicted in Fig. 4. Thereby the materials and their sequence were selected in such a way that the occurring interfacial DMIs possess the same directions and thus behave additively resulting in an increased total DMI as also indicated in the same figure [23]. However, there are controversial results regarding the DMI of iridium interfaces [9] and therefore this increasing effect is not guaranteed. The high DMI is associated with predominantly Néel-like internal domain wall structures instead of magnetostatically favorable Bloch domain walls [22, 23, 16].

Due to the resolution limit of all experiments performed here only the collective magnetic behavior of all ferromagnetic layers is observable. Thus the important magnetic properties M_S, K_{eff}, and A_{ex} are exhibited by all cobalt and nickel layers altogether. The ultrathin layers result in particularly strong dipole energy contributions which favor stochastically distributed labyrinthic or dendrimer-like domain textures as visible in Fig. 5 [23]. Additionally,

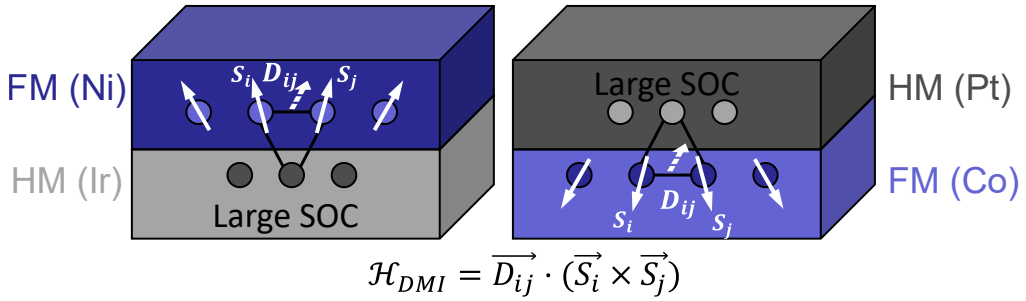

Figure 4: Schematic illustration of the two distinct heavy metal (HM) - ferromagnetic (FM) interfaces of the layer system at which an interfacial DMI occurs according to Eq. (52) in section 2.3 [9]. Due to the choice of materials and their sequence, the two contributions to the total DMI are expected to behave additively resulting in an increased overall DMI [23]. The vectorial DMI in the displayed HAMILTONIAN operator is simplified to the scalar value of D.

the ultra-thin film thickness results in a perpendicular magnetization anisotropy according to Eq. (45) and the related discussion. Literature values are known for the exchange stiffness $A_{\mathrm{ex}} = 1.6 \cdot 10^{-11}\,\mathrm{J/m}$, the saturation magnetization $M_{\mathrm{S}} = 600\,\mathrm{kA\,m^{-1}}$, and the effective crystal anisotropy $K_{\mathrm{eff}} = 2 \cdot 10^{5}\,\mathrm{J\,m^{-3}}$ of comparable samples [16]. There, typical values for the DMI are specified as well, which range from $D = 0.2$ to $1.5\,\mathrm{mJ\,m^{-2}}$ [16].

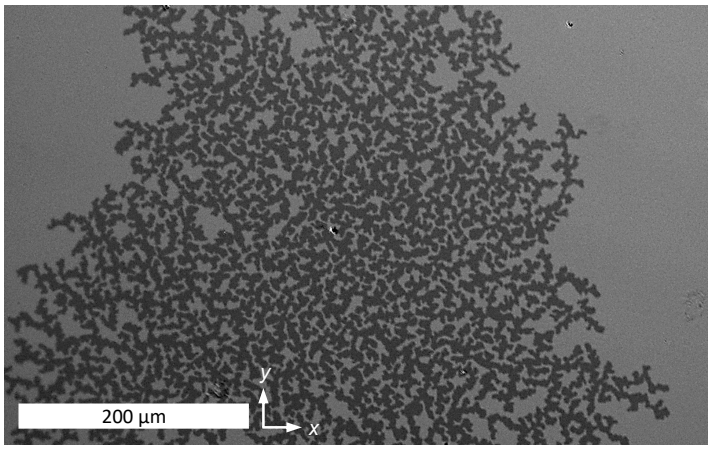

Figure 5: Exemplary domain image of a perpendicularly magnetized sample taken with a KERR microscopy setup. The image has been post-processed to increase contrast. The darker shaded region corresponds to magnetization in the drawing plane (antiparallel to the surface normal) and the light gray regions correspond to the magnetization out of the drawing plane (parallel to the surface normal).

3 Characterization Methods

The investigation of the interfacial DMI and its modification via ion bombardment requires the examination of the thin-film system's magnetic properties. The saturation magnetization and the effective crystalline anisotropy were determined by a vectorial vibrating sample magnetometer (VVSM). For analyzing the effective DMI field, an experimental self-constructed setup based on a commercial wide-field KERR microscope has been assembled. In the following, the characterization methods with the corresponding experimental setup and functional principles will be presented.

3.1 Vectorial Vibrating Sample Magnetometer

The vectorial vibrating sample magnetometer (VVSM) is a specialized version of the classical vibrating sample magnetometer (VSM). A VSM is a setup for the detection of the sample's total magnetization as a function of an external controllable magnetic field [17]. The signal of the total magnetization is caused by a position-dependent integration over the volume of the ferromagnetic material [17] and is detected based on eddy currents in pickup coils according to FARADAY's law of induction [17]. Accordingly, the VVSM detects the magnetic moment exhibited by the complete sample instead of its magnetization. FARADAY's law of induction states that temporal changes in the magnetic flux Φ_B of area $\vec{A}$ enclosed by a closed conductive path or coil with N repetitions induces an electromotive force in the form of a voltage V_ind, following

$$V_\mathrm{ind} = -N \cdot \frac{\mathrm{d}\Phi_\mathrm{B}}{\mathrm{d}t} \quad \text{with}\, \Phi_\mathrm{B}(t) = \int \vec{B}(t) \cdot \mathrm{d}\vec{A} \tag{54}$$

with the directed magnetic field $\vec{B}(t)$ which depends on the time t [17]. In the case of the VVSM, the closed coils are integrated into the setup with a fixed area and number of repetitions [17]. Consequently, the induced voltage inside the pickup coils originates from changes in the magnetic field passing through the coils. With well-calibrated VVSMs, this voltage originates solely from the sample or more specifically from its magnetic moment, for this purpose the sample is excited to vibrate in the vicinity of the pickup coils [17]. The oscillation, i.e., the frequent changes in the sample position results in periodically induced voltages, which can be allocated to magnetic moments with an appropriate calibration [17]. A simplified schematic sketch of a typical VVSM setup is depicted in Fig. 6. To highlight the vectorial part, which distinguishes a VVSM from other VSMs, attention should be directed toward the rotation axis of the sample holder as well as the orthogonally arranged pickup coils

around the sample material. In the commercial VVSM from the company *MicroSense*, the sample is glued to a glass rod (sample holder) which itself is mounted to a vibrator on top of the VVSM. The vibrator and thus the sample is freely adjustable in all 3 dimensions enabling a central positioning of the sample in between the detecting pickup coils. The coils themselves are surrounded by a large set of electromagnets creating external magnetic fields $\vec{H}_{\text{ext}}$ up to 2.4 T along the x-direction. The biaxial pickup coils are placed in a plane parallel to the rotation plane and perpendicular to the vibration direction of the sample. The first two coils are placed parallel to the applied external field (x-coils, sensitive to the parallel magnetization component $m_{\parallel}$) and the remaining two y-coils are oriented perpendicular to the external field (sensitive to the perpendicular magnetization component $m_{\perp}$). With this biaxial, vectorial arrangement, the magnetization components parallel and orthogonal to the external magnetic field are detected at the same time providing knowledge about the angular dependence of the magnetization vector $m_{\text{total}} = \sqrt{m_{\parallel}^2 + m_{\perp}^2}$ if combined with angular resolved sample rotation of the [17, 24].

3.1.1 Hysteresis Loops - Saturation Magnetization

Plotting the magnetic moment extracted from the calibrated coils against the externally applied field in a sufficiently large field loop results in a typical hysteresis curve if a ferromagnetic specimen is sampled. Note that in this hysteresis loop the sample's magnetic moment $m(\vec{H}_{\text{ext}})$ and not its magnetization $M(\vec{H}_{\text{ext}})$ is measured as a function of the external magnetic field. As mentioned beforehand, the magnetic moment results from the integral of the magnetization M over the volume V of the ferromagnetic material. Assuming that variations of the magnetic properties in the small sample volumes are minor and remagnetization processes are distributed uniformly over the entire sample, this integral can be simplified as the product of the mean magnetization and the volume of the ferromagnetic material

$$m_{\text{total}} = \int_V M \cdot \mathrm{d}V = M \cdot V \quad [13] \; . \tag{55}$$

Of particular interest is saturation magnetization M_{S}, which describes the density of magnetic dipoles in the ferromagnetic material. As the name suggests, saturation magnetization M_{S} represents the maximal, constant (saturated) magnetization of a ferromagnetic material, which can be reached by a sufficiently strong external magnetic field. This occurs when all of the microscopic magnetic dipole moments are aligned parallel in the same direction. In a hysteresis curve, a saturated magnetization appears as a field region in which the magnetic

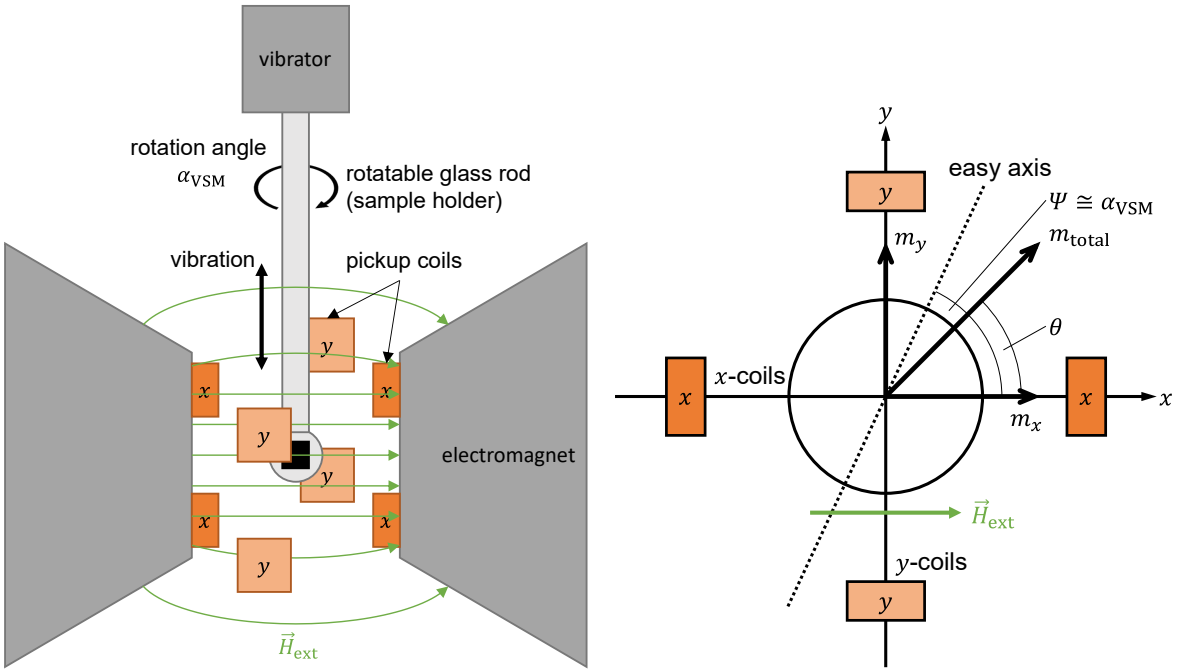

(a) Simplified schematic illustration of the *MicroSense* VVSM setup in side view.

(b) Arrangement of the magnetization components and the angles in top view. Based on [17].

Figure 6: Schematic illustration of the setup of the *MicroSense* VVSM. The external magnetic field ($\vec{H}_{\mathrm{ext}}$, green) lies in the drawing plane and passes through the sample (black) attached to the rotatable glass (rotation angle α_{VSM}, light gray) rod which is excited to vibrate by a vibrator. The pickup coils are colored orange and lie within the rotation plane with the lighter y-coils perpendicular to the external magnetic field and the x-coils parallel to it. Therefore, the y-coils are sensitive for the perpendicular magnetization $m_{\perp}$ and the x-coils for the parallel magnetization $m_{\parallel}$, respectively. The angle Ψ states the angle between the externally applied magnetic field and the easy axis of the sample. The angle between the vectorial magnetic moment m and the applied magnetic field is stated as θ.

moment remains constant with increasing absolute field strengths. The quantification of this maximum magnetic moment and thus of the saturation magnetization requires a calibrated characterization method that is sensitive to the magnetic moment, i.e., the calibrated VVSM. In saturation, the magnetic moment is composed of the saturation magnetization and the volume of the magnetic material as depicted in Eq. (55), whereby the volume can be separated into the area A and the thickness of all ferromagnetic layers in the multilayer system, t_{FM},

$$m_{\mathrm{total,\,S}} = M_{\mathrm{S}} \cdot V = M_{\mathrm{S}} \cdot A \cdot t_{\mathrm{FM}}\,. \tag{56}$$

Consequently, by extending the VVSM measurements with information about the sample volume, the saturation magnetization can be easily determined with hysteresis measurements.

The possibility of rotation and the biaxial arrangement of the pickup coils of the VVSM splitting the total magnetization vectorially, enables torque-curve measurements providing information about the sample's magnetic anisotropy [17].

3.1.2 Torque Curves - Magnetic Anisotropy

As referred to at the beginning of this thesis, the magnetic anisotropy F_{anis} describes the dependence on the orientation of magnetic properties due to preferred spatial orientations of the magnetic dipoles in the sample material. Hereby, the magnetic anisotropy is defined as the energy difference between the easy axis (energetically most favorable orientation) and the hard axis (energetically most unfavorable orientation). Analogous to saturation magnetization M_{S}, this energy is usually reduced to a volume element resulting in an energy density $\frac{F_{\text{anis}}}{V} = f_{\text{anis}}$ [13].

There are several parameters affecting both, the absolute value of this energy as well as the spatial orientations of the easy and hard axes. As already introduced in section 2.4, the samples to be examined possess an easy magnetization axis perpendicular to the sample surface which is usually labeled as (bidirectional or uniaxial) out-of-plane anisotropy or perpendicular magnetic anisotropy. The hard axes lie within the sample plane. Consequently, the effective magnetic anisotropy f_{anis} is the energy required to direct the magnetic moments from out-of-plane to the in-plane hard axis and is composed of the magnetocrystalline anisotropy f_{cryst} and the surface anisotropy f_{S}. The anisotropy contributions are commonly expressed as a power series of sine functions with even exponents representing the directional energy dependence if it is considered in polar coordinates [21]. The anisotropy of the investigated samples with uniaxial symmetry is thereby expressed as

$$f^{(1)}_{\text{anis}}(\theta) = K_1 \cdot \sin^2(\theta) \tag{57}$$

$$f^{(2)}_{\text{anis}}(\theta) = K_1 \cdot \sin^2(\theta) + K_2 \cdot \sin^4(\theta)\,, \quad [14] \tag{58}$$

if only rotation in a plane along the easy axis is considered with θ being the angle between magnetization $\vec{m}$ vector and easy axis [17]. The exponent in brackets indicates the power of the power series and therefore how many magnetic anisotropy constants K_i are included as coefficients.

The essential idea of the torque-curve analysis is a targeted deflection of the magnetization $\vec{m}$ in the energy landscape given by the anisotropy f_{anis} via rotation of the sample relative

to the external magnetic field $\vec{H}_{\text{ext}}$ [17]. The potential energy contribution E_m caused by the external magnetic field favors a parallel alignment of the magnetization while the energy landscape contribution E_f of the anisotropy favors an alignment along its minima, i.e., the easy axes. The temperature-dependent total energy E_{total} in this situation is

$$E_{\text{total}} = E_0 + E_f + E_m = E_0 + E_f\left(\frac{\vec{m}}{|m|}\right) - \vec{m}\cdot\mu_0\vec{H}_{\text{ext}} \quad [17]\ . \tag{59}$$

In this equation, all direction-independent and thus isotropic components are summarized in the constant term E_0. Reducing the energy contributions by the volume results in

$$\begin{aligned}\frac{E_{\text{total}}}{V} &= \frac{E_0}{V} + f_{\text{anis}}\left(\frac{\vec{m}}{|m|}\right) - \vec{M}\cdot\mu_0\vec{H}_{\text{ext}} \\ \frac{E_{\text{total}}}{V} &= \frac{E_0}{V} + K_1\cdot\sin^2(\theta) + K_2\cdot\sin^4(\theta) - M\cdot\mu_0 H\cdot\cos(\alpha+\theta) \quad [17]\ ,\end{aligned} \tag{60}$$

whereby the mutual alignment between rotation, easy axis, and magnetization is expressed by the angles θ and the rotation angle α [17]. During all experiments, the sample has been aligned so that $\alpha = 0°$ corresponds to a parallel alignment of the external magnetic field and the easy axis.

In the equilibrium state, the contributions from the external magnetic field and the anisotropy balance each other out, whereby an energy minimum with condition $\frac{\mathrm{d}E}{\mathrm{d}\theta} = 0$ is met. Hence, the equations

$$\begin{aligned}\frac{\mathrm{d}E}{\mathrm{d}\theta} &= \frac{\mathrm{d}E_f}{\mathrm{d}\theta} + \frac{\mathrm{d}E_m}{\mathrm{d}\theta} = 0 \\ \frac{\mathrm{d}f_{\text{anis}}}{\mathrm{d}\theta} &+ \frac{\mathrm{d}\left(-\vec{M}\cdot\mu_0\vec{H}_{\text{ext}}\right)}{\mathrm{d}\theta} = 0 \quad [17]\end{aligned} \tag{61}$$

hold true. For an anisotropy power series with the first two coefficients $f^{(2)}_{\text{anis}}(\theta)$, the second equation in (61) results in

$$\begin{aligned}L(\theta) = \quad & \frac{\mathrm{d}f_{\text{anis}}}{\mathrm{d}\theta} && = && -\frac{\mathrm{d}\left(-\vec{M}\cdot\mu_0\vec{H}_{\text{ext}}\right)}{\mathrm{d}\theta} \\ L(\theta) = \quad & (K_1+K_2)\cdot\sin(2\theta) - 2\cdot K_2\cdot\sin(4\theta) && = && \mu_0 H\cdot M\sin(\theta+\alpha) \quad [17]\ .\end{aligned} \tag{62}$$

The left part of this equation represents the torque $L(\theta)$ which is caused by the anisotropy. The term $M\sin(\theta+\alpha)$ of the magnetic field contribution is equal to the magnetization component perpendicular to the external field $M_\perp(\alpha)$. Thus, the magnetic anisotropy, i.e., the power series coefficients K_i, are quantified by a least mean square fit of angle-dependent measurements of the magnetization component perpendicular to the applied constant magnetic field $\vec{H}_{\text{ext}}$

$$(K_1+K_2)\cdot\sin(2\theta) - 2\cdot K_2\cdot\sin(4\theta) = \quad \mu_0 H\cdot M_\perp(\alpha) \quad [17]\ . \tag{63}$$

For ensuring angle-dependent comparability, the external magnetic field must fulfill at least the following two conditions:

1. The field has to be sufficiently large to ensure an approximately uniform magnetization for all angles meaning that every measured value of $M_{\perp}(\alpha)$ always represents the magnetization component of the whole sample volume. It should be particularly highlighted that this method does not require saturation along the hard axis, i.e., perfect uniform magnetization [25]

2. One single large domain should be present in the sample so that energy contributions of the domain landscape are negligible [25].

In general, both requirements agree with larger external magnetic fields enabling higher precision of this measurement method [25, 24]. There are two possibilities for performing these kinds of measurements [17]

1. Rotation of the sample in a constant external magnetic field while recording its perpendicular magnetization component

2. Several hysteresis loops with different rotation angles at which the perpendicular magnetic moment is compared at a fixed field strength.

Another estimation method for the determination of the anisotropy constant is the measurement of the field at which the saturation magnetic moment μ changes by 0.5 times the Δm uncertainty of m. Based on this field, the anisotropy field of the hard axis H_K can be estimated, which enables the calculation of K_{eff} via

$$K_{\text{eff}} = \frac{H_K \cdot \mu_0 \cdot M_{\text{S}}}{2} \quad [9] \ . \tag{64}$$

3.1.3 VVSM - Measurement Procedure

To determine both, the saturation magnetization and the magnetic anisotropy, a small piece of the sample was cut out of the wafer and broken into three parts with roughly equal volume, resulting in negligible sample-to-sample variations. All three samples were measured once without being bombarded ($D_{\mathrm{IB}} = 0 \cdot 10^{13}\,\mathrm{cm}^{-2}$) and once with sample-specific ion doses of $D_{\mathrm{IB}} = 7.5 \cdot 10^{13}\,\mathrm{cm}^{-2}$, $1 \cdot 10^{14}\,\mathrm{cm}^{-2}$, and $1 \cdot 10^{15}\,\mathrm{cm}^{-2}$ (see section 5). Based on these four ion dose values, the dependence of the saturation magnetization and magnetic anisotropy on the ion dose will be approximated via interpolation. Due to the limited available sample material, it has been opposed to obtaining more data points.

In the VVSM, the magnetization components in x- ($m_{\parallel}$) and y-direction ($m_{\perp}$) were determined as a function of the rotation angle, with external fields along x-direction in ranges of up to $\pm 1000\,\mathrm{mT}$ for $\alpha = 80 - 100°$ and $260 - 280°$ and ranges up to $\pm 100\,\mathrm{mT}$ for all other angles. The higher field strengths around 90° and 270° are required to obtain saturation along the hard axis.

For the $|\vec{H}_{\mathrm{x,\,ext}}|_{\mathrm{max}} = 100\,\mathrm{mT}$ measurements, the field strength was varied in 2 mT steps for regions clearly outside the expected out-of-plane coercivity ($|\vec{H}_{\mathrm{x,\,ext}}| > 40\,\mathrm{mT}$) and in 0.5 mT steps within this region. For the measurements with $\pm 1000\,\mathrm{mT}$ as the maximum field strength, the field has been changed in correspondingly 10 times larger steps. Due to the long measurement time of almost one hour per hysteresis loop, the rotation angle was only roughly altered in steps of 10° between 0 and 360°. Before each measurement series, the VVSM was calibrated with a specific nickel calibration sample. For each sample, this results in 37 hystereses without IB and 37 hystereses with the sample-specific ion dose, which is declared in section 5. Additionally, each hysteresis measurement contains its component-wise information resulting in one hysteresis of $m_{\parallel}$ and one of $m_{\perp}$. Section 9.2 contains more information on the measurement procedure and exemplary hysteresis loops of a non-bombarded sample.

3.2 Magneto-optical Kerr Microscopy

Magnetic domains can be imaged locally on a reflective sample surface with a magneto-optical Kerr microscopy setup which is based on the eponymous underlying magneto-optical Kerr effect (MOKE). Hereby, each pixel intensity of a captured image represents its location-dependent magnetization in the form of a grayscale or contrast value. Thus the resulting grayscale image outlines the surface magnetization in the investigated field of view (FOV)

via grayscale contrasts.

While applying external magnetic fields, the KERR microscopy is a suitable tool for time-resolved investigations of dynamic magnetization processes, on the condition that the spatial resolution and the frame rates are sufficient for the length and time scales of the dynamic process. One of these dynamic magnetization phenomena is a surface hysteresis loop whose measurement can be performed by MOKE-magnetometry. In this measurement method, the average grayscale value of the FOV is recorded in dependence on the external magnetic field. Another dynamic magnetization process, which is by far more relevant for this work is the asymmetric bubble expansion method. Therefore, this method is dealt with specifically in section 3.2.3.

In general, magneto-optical KERR microscopy is a quite popular examination method which is attributed to the required optical components being comparatively affordable as well as its applicability towards high temporal resolution and a wide temperature range [13].

This thesis is mainly focused on MOKE microscopic experiments and their associated evaluation and interpretation. Therefore, the following sections are intended to discuss the physical effects, the partly self-constructed setup, and measurement procedures as well as the extraction of the desired information in this order in detail.

3.2.1 Magneto-optical Effects

Magneto-optical effects are based on light-matter interactions of polarized light with a magnetic sample [21, 13] and thereby enable the observation and visualization of magnetic domain structures [21].

Thereby, the domain observation via magneto-optical effects is based on small rotations of the light's polarization plane upon reflection (magneto-optical KERR effect) and transmission (magneto-optical FARADAY effect) in magnetic material which is transferred to intensity changes in polarization microscopy. The differences in the polarization of originally linearly polarized light caused by these effects are often described in the form of a magnetic circular birefringence [21]. Hereby, it is assumed that linear polarization of light manifests as the superposition of left and right circularly polarized light in an equivalent ratio [17]. Both of these circular polarization states interact spin-specifically with the electronic system of the matter resulting in slightly different absorption coefficients (magnetic circular dichroism) and refractive indices (magnetic circular birefringence) for magnetic samples. This is due to magnetic exchange interactions affecting the electronic system spin-specifically as well [14]. The

interaction is described via polarization-dependent refractive indices, the real part of which results in different velocities and thus in a phase difference, i.e. a change in polarization (circular birefringence). The imaginary part describes different absorption coefficients (circular dichroism). In the following, only the real parts are discussed.

Besides the aforementioned two magneto-optical effects which linearly depend on the sample magnetization, there is also the magneto-optical VOIGT effect, which scales quadratically with the magnetization and has a possible contribution to the MOKE imaging [21]. The magneto-optical VOIGT effect occurs upon linear birefringence of light on magnetized materials and is also known as linear magnetic birefringence or the CUTTON-MOUTON effect [21]. Table 1 gives an overview of these magneto-optical effects as well as the associated ordinary optical effects. Ferromagnetic samples are rarely composed of transparent materials which

Table 1: Overview of magneto-optical effects and their related ordinary optical effects for non-magnetic materials [21, 17].

Magneto-optical effect	related optical effect with non-magnetic matter
magneto-optical KERR effect	circular birefringence and dichroism in reflection
magneto-optical FARADAY effect	circular birefringence and dichroism in transmission
magneto-optical VOIGT effect	linear birefringence in transmission and reflection

are required for the magneto-optical FARADAY and VOIGT effects. This also typically applies to thin film systems which, however, often possess exquisite reflective properties due to their flat and clean surfaces. Therefore, the magneto-optical investigation of thin film samples is essentially based on the magneto-optical KERR effect which thereby limits the characterization of the sample's surface magnetization.

Nonetheless, the magneto-optical FARADAY and VOIGT effects often occur in MOKE microscopy as distorting side effects originating in the diamagnetic and paramagnetic properties of optical elements and surrounding air in the presence of sufficiently strong external magnetic fields. All of these three magneto-optical effects can be collected in a generalized tensor description of the dielectric permittivity ε via [21]

$$\varepsilon = \varepsilon_0 \varepsilon_\mathrm{r} \begin{bmatrix} 1 & -\mathrm{i}Q_\mathrm{V} m_{z0} & \mathrm{i}Q_\mathrm{V} m_{y0} \\ \mathrm{i}Q_\mathrm{V} m_{z0} & 1 & -\mathrm{i}Q_\mathrm{V} m_{x0} \\ -\mathrm{i}Q_\mathrm{V} m_{y0} & \mathrm{i}Q_\mathrm{V} m_{x0} & 1 \end{bmatrix} + \begin{bmatrix} B_1 m_{x0}^2 & B_2 m_{x0} m_{y0} & B_2 m_{x0} m_{z0} \\ B_2 m_{x0} m_{y0} & B_1 m_{y0}^2 & B_2 m_{y0} m_{z0} \\ B_2 m_{x0} m_{z0} & B_2 m_{y0} m_{z0} & B_1 m_{z0}^2 \end{bmatrix} . \tag{65}$$

The first term, composed of the relative and vacuum permittivity ε_r and ε_0, is extended by a second tensor describing the rotation of the polarization plane caused by the KERR or FARADAY effect, which scales with the magnetization direction $\vec{m}_0 = (m_{x0}, m_{y0}, m_{z0})^T = \frac{\vec{M}}{|\vec{M}_\mathrm{S}|}$ of the sample, as well as the material and wavelength specific VOIGT constant Q_V. In the second term of Eq. (65), the components of the direction of magnetization are included quadratically since this is the contribution of the VOIGT effect to the rotation of the polarization plane. The constants B_1 and B_2, describing the strength and contribution of the VOIGT effect, typically differ from each other in cubic crystal structures while they are equal in amorphous or isotropic media [21].

Since the VOIGT-effect scales with the magnetization squared it is important for samples with large magnetization. With a rather low magnetization, the magnetic circular effect dominates over the linear one, which simplifies the equation Eq. (65) to the first term, resulting in a dielectric displacement field $\vec{D}$ of

$$\vec{D} = \varepsilon_0 \varepsilon_\mathrm{r} \left(\vec{E} + \mathrm{i} Q_\mathrm{V} \vec{m}_0 \times \vec{E} \right) \quad [21,\ 17]\ , \tag{66}$$

per MAXWELL's equations. The electric field $\vec{E}$ along $\vec{n}_0$ of linear polarized light can be described by a plane wave following the function

$$\vec{E} = \vec{n}_0 E_0 \cdot e^{\mathrm{i}(\vec{k}\cdot\vec{r} - \omega t)} \quad [17], \tag{67}$$

with the amplitude E, the angular frequency ω, and the wavenumber k in dependence on the spacial coordinate r along the propagation direction with $\vec{r} \perp \vec{n}_0$ and the time t. The tensor structure of ε originates in the magnetization $\vec{m}_0 \neq 0$ and causes the matter to interact anisotropically. This means that with $\vec{m}_0 \neq 0$, i.e., non-zero off-diagonal tensor elements, the displacement field inside the matter and the incoming electric field are not parallel to each other and a rotation of the polarization occurs [17].

A comparable tensor results for the magnetic permeability of the sample. However, these gyromagnetic contributions are about two orders of magnitude smaller than the gyroelectric in the visible frequency range [21]. The dielectric displacement vector in Eq. (66) therefore represents a simplification, which is nevertheless able to explain the majority of the effects.

Magneto-optical Kerr Effect

A mathematically detailed consideration of the KERR effect as circular birefringence and circular dichroism can be found, for example, in [17]. In this section, only the geometrical effects on the KERR effect will be dealt with. Hereby, the KERR effect is strongest when the electric field component and the magnetization are at right angles to each other [21, 17]. Therefore, the spatial arrangement between the angle of incidence, the electric field component, and the magnetization are of particular importance for the rotation of the polarization plane and thus for the signal detection in MOKE setups. The extreme cases of orthogonal and parallel arrangement of these are referred to as polar, longitudinal, and transverse KERR effects, whereby these denominations state the magnetization direction relative to the plane of incidence and the surface normal. In the polar KERR effect, the magnetization points normal to the surface as shown in Fig. 7. This is the relevant geometry for all magneto-optical measurements in this work since it is the only geometry sensitive to magnetizations parallel to the surface normal (compare Fig. 7 and Fig. 8). In the longitudinal and transverse

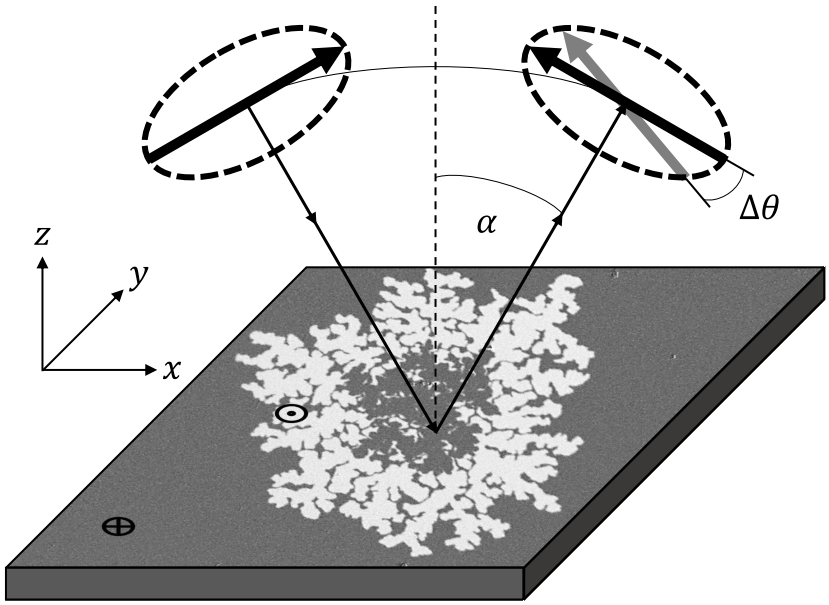

Figure 7: Schematic illustration of the polar MOKE effect. The angle α depicts the angle of incidence and the angle difference $\Delta\theta$ depicts the rotation of the polarization axis after reflection. The magnetization state is given by grayscale shading and arrows, whereby brighter/$\odot$ refers to an upwards directing magnetization and darker/$\otimes$ refers to a downwards directing magnetization, respectively.

geometries, the magnetization is parallel to the surface, whereby the magnetization in the longitudinal arrangement is additionally parallel to the plane of incidence. In the transverse arrangement, it is orthogonal to the plane of incidence. All of these three geometries are

depicted in Fig. 8. In the longitudinal arrangement, the orientation of the incoming linear polarization causes two possible variations: longitudinal ∥ and longitudinal ⊥. As mentioned,

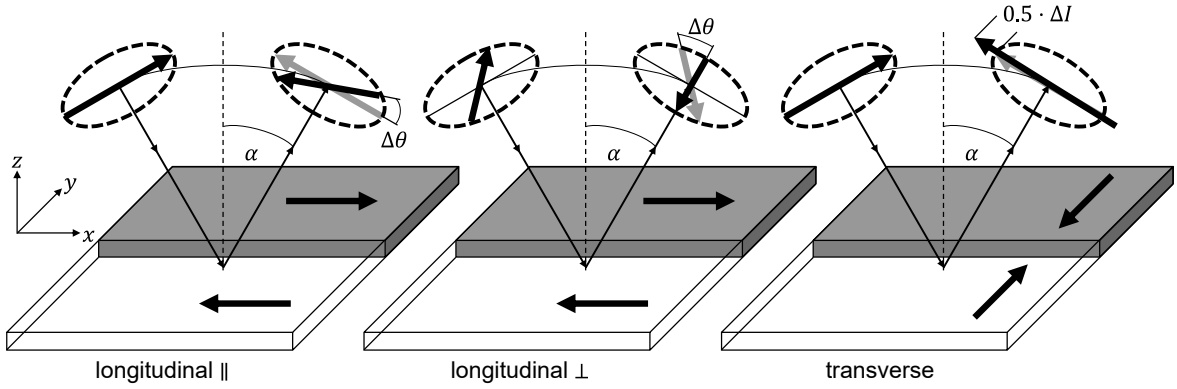

Figure 8: Schematic illustration of the other geometric arrangements in which the MOKE effect occurs. These are the parallel and perpendicular longitudinal configurations as well as the transverse configuration. The transverse configuration differs from the other arrangements because there is no change in polarization but an amplitude fluctuation of ΔI [21, 17]. The angle α depicts the angle of incidence in all configurations and the angle change $\Delta\theta$ depicts the rotation of the polarization axis after reflection for the longitudinal cases. The magnetization of the sample is indicated by the white and gray shading whereby the direction is given by the black arrows.

the magneto-optical effects appear strongest when the electric field of the incoming wave and the magnetization are orthogonal to each other [21, 17]. For the relevant polar MOKE effect, it is therefore favorable to work with a small angle of incidence α. In the setup, the light is focused onto the sample via a crosswise arranged array of LEDs (see Fig. 9a), which only have a small angle of incidence $\alpha \approx 0$. As a result, a high KERR contrast is possible, which allows the domains and their dynamics to be viewed without further digital image processing. This is of great advantage as it allows in-situ observation and control of the measurement.

Magneto-optical Faraday Effect

In principle, the considerations of the magneto-optical KERR effect also apply to the FARADAY effect but for light transmitted through magnetic matter. Thus, the FARADAY effect requires transparent samples. In these, the FARADAY effect is usually more pronounced than the KERR effect, since the interaction volume between light and matter is significantly larger in transmission than in reflection [17]. In the case of reflection, the interaction volume is may be described by the penetration depth, which in turn is determined by an evanescent wave that decays exponentially in the matter [17].

However, the FARADAY effect rarely occurs in ferromagnetic materials and ferromagnetic thin films because most of them are not transparent [21, 17]. Therefore, the magneto-optical FARADAY effect only appears as a parasitic effect in magneto-optical microscopy and magnetometry. Hereby, the optical elements cause a FARADAY rotation in the presence of magnetic fields. This FARADAY rotation is superimposed on any light rotation being caused by the magnetism of the microscopically investigated sample surface [17]. This effect is induced by external fields which reach the optical elements and thus especially apply to measurements with large external magnetic fields. Since only weak external fields[1] have been applied, the Faraday effect was weak and could be estimated and removed using linear functions in the saturation range. For stronger field strengths, suggested solutions have been listed in a bachelor thesis [26].

Magneto-optical Voigt Effect

While the first-order KERR and FARADAY effects are sensitive to the magnetization direction, the VOIGT effect is sensitive to the magnetization axis due to its quadratic dependence on the magnetization. Additionally, the VOIGT effect mainly causes elliptical polarization states, while the first-order effects primarily affect polarization rotations. For this reason, a compensator is required for magneto-optical measurements based on the VOIGT effect, while in MOKE microscopy, the compensator is essentially only used to increase the contrast (see Fig. 9a).

A crucial prerequisite for the VOIGT effect is a magnetization component perpendicular to the propagation vector $\vec{k}$ of the incoming light [17]. Due to the out-of-plane magnetization of the samples and the almost normal incidence of the light beam, it is assumed that the VOIGT effect also occurs as a parasitic effect. This is probably coupled to the external in-plane field since this is perpendicular to the propagation vector $\vec{k}$.

[1] Referring to oop field strengths which were mainly below $|H_z| \leq 15\,\mathrm{mT}$. The ip field strengths were up to $|H_x| \leq 180\,\mathrm{mT}$. However, the ip field has less impact on the optical elements due to the arrangement visible in Fig. 9b.

3.2.2 Wide-field Kerr Setup

The KERR images recorded in this work are based on a partially modified wide-field KERR microscope of the company EVICO MAGNETICS which is schematically illustrated in Fig. 9a.

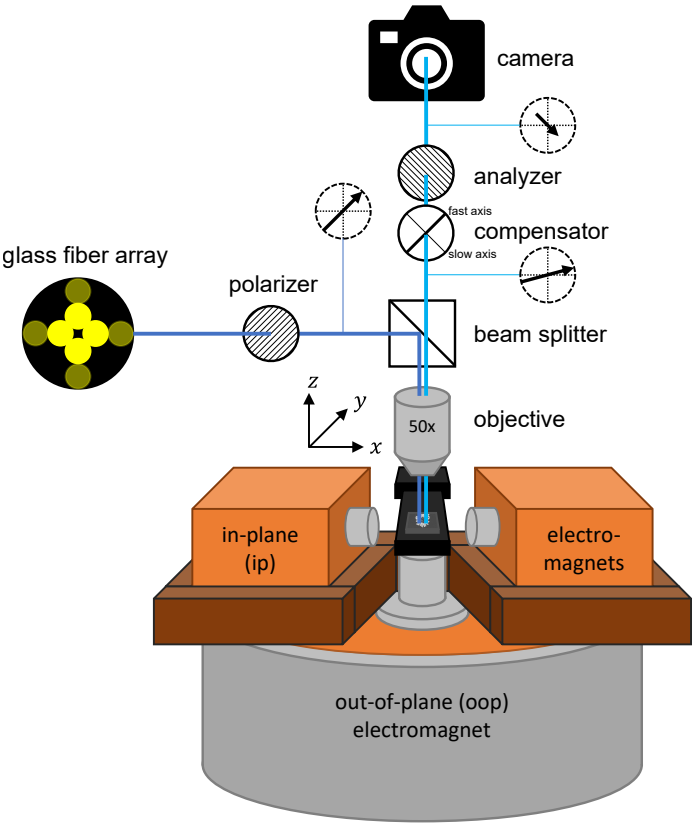

(a) Simplified schematic illustration of the modified KERR microscopy setup.

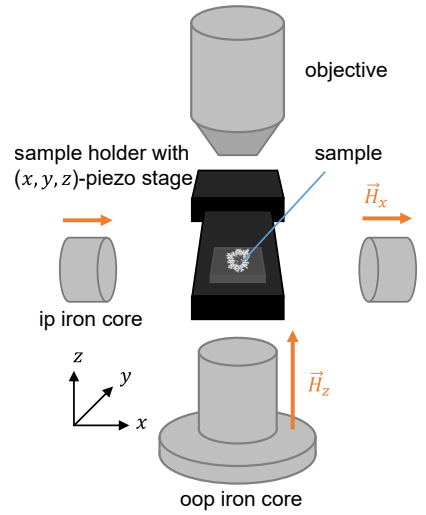

(b) Mutual arrangement of sample and external magnetic fields.

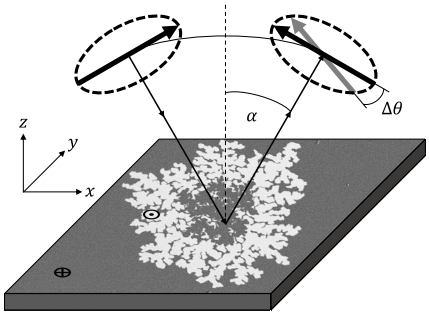

(c) Schematic drawing of the *polar* MOKE effect.

Figure 9: A simplified schematic illustration of the modified KERR microscopy setup with controllable oop ($\vec{H}_z$) and ip magnetic fields ($\vec{H}_x$) is shown in Fig. 9a. Hereby, the sample is located in the center of several electromagnets (orange), whose magnetic fields are focused into the sample volume via iron cores (light grey). The optical path (blue) consists of a light source, polarizer, beam splitter, objective, reflective sample, compensator, analyzer, and camera, whereby the incident light is indicated by a darker shade than the reflected light. The mutual orientation of the sample surface and magnetic fields is highlighted in Fig. 9b. The underlying *polar* MOKE effect enabling the domain imaging is sketched in Fig. 9c which is equal to the image in Fig. 7.

The most important components of the optical system of this setup and their functionalities are introduced in the following list with an order corresponding to the optical path starting from the light source (1) and ending with the camera (8):

1. **light source, LED array** - providing controllable, bright, and uniform illumination of the sample in a wavelength range of 420 to 680 nm
2. **first polarization filter (polarizer)** - generates a predefined polarization state of the incoming light beam
3. **the beam splitter** - separation of incoming and reflected beam paths
4. **objective, 50x (NA 0.8) or 100x (NA 1.3, immersion oil)** - focuses the incident beam onto the sample surface
5. **magnetic sample surface** - reflecting the incoming beam with a changed polarization state depending the magnetization of the sample
6. **(birefringent) compensator** - compensates phase shifts in elliptical polarization states arising from secondary effects like the VOIGT effect or imaginary absorption coefficients [17]
7. **second polarization filter (analyzer)** - blocks the predefined polarization state, while light with changed polarization passes
8. **camera** - laterally resolved pixel by pixel detection of reflected light.

The most crucial component of MOKE microscopy is the polarizer-analyzer pair, which converts changes in the polarization state, i.e., the KERR effect, into intensity changes. In the experiment, these, as well as the compensator, are adjusted to achieve maximum contrast between the different directions of magnetization.
Besides the image recording optical system, the sample's magnetization state can be varied precisely by the controllable magnetic fields of the implemented electromagnets. The electromagnets are arranged as depicted in Fig. 9b, in order to address the parallel (x-direction) and perpendicular (z-direction) components of the external magnetic field separately. This is the only experimental precondition to enable the asymmetric bubble expansion method with typical wide-field KERR microscopes [9]. There is one large electromagnet generating the out-of-plane field component and a pair of electromagnets additionally generating the

in-plane field component, whereby the magnetic field is focused on the sample volume by the iron cores. For the componentwise control of the magnetic field in the volume of the samples, the orientation of the electromagnets, or rather their fields relative to the sample surface is of particular interest. The stacked positioning as well as the orientation are realized by 3D printed components designed specifically for this purpose. Within this work, two further modifications were assembled to the setup, which designs are depicted in Fig. 53 in the appendix section 9.3.

The first modification is an improved out-of-plane iron core offering more support with a larger area, resulting in more homogeneous fields with better experimental reproducibility. The second modification is an extension to the sample holder with a stability-enhancing crossbar which intentionally enables mechanical tilting of the sample. Without this tilt correction, a spurious out-of-plane field component can be present when an in-plane field is applied, which would distort the results [9].

3.2.3 Asymmetric Bubble Expansion Method

The DMI can be measured by, for example, Brillouin light scattering (BLS) measurements based on spin waves [9]. However, another measurement method based on MOKE microscopy is more promising as a standard measurement method in the future because it requires lower-cost setups and sample preparation compared to other measurement methods [9].

For thin films with perpendicular magnetization, the scalar DMI strength D is describable by an effective in-plane field H_{DMI} acting on NÉEL domain walls

$$\mu_0 \cdot H_{\mathrm{DMI}} = -\frac{D}{M_{\mathrm{S}} \cdot \lambda}\,, \tag{68}$$

with M_{S} as the saturation magnetization in the thin film and λ as the domain wall width [9, 22]. This field lies within the sample and promotes NÉEL domain walls over BLOCH domain walls [22, 23, 16].

Since the domain walls here consist of a 180° rotation of magnetic moments, its width can be estimated from $\lambda = \sqrt{\frac{A_{\mathrm{ex}}}{K_{\mathrm{eff}}}}$, resulting in

$$\mu_0 \cdot H_{\mathrm{DMI}} = -\frac{D}{M_{\mathrm{S}} \cdot \sqrt{\frac{A_{\mathrm{ex}}}{K_{\mathrm{eff}}}}}\,, \tag{69}$$

$$|D| = \left|\mu_0 \cdot H_{\mathrm{DMI}} \cdot M_{\mathrm{S}} \cdot \sqrt{\frac{A_{\mathrm{ex}}}{K_{\mathrm{eff}}}}\right| \quad [9,\, 23,\, 16]\ . \tag{70}$$

This DMI in-plane field H_{DMI} affects the domain wall energy, enabling a domain wall velocity-based measurement method of the DMI field: the asymmetric expansion of a bubble domain

in presence of an in-plane applied magnetic field [9]. Hereby, a domain is expanded in the creep regime [9], in which the expansion velocity of the domain wall depends on the domain wall energy density according to the ARRHENIUS creep law [9, 16]. The energy density in turn depends on the DMI field and the in-plane field as shown in Eq. (50), which is repeated here

$$\sigma(H_x, \psi) = \sigma_0 + 2K_\mathrm{D}\lambda\cos^2\psi - \pi\mu_0 M_\mathrm{S}\lambda\,(H_x + H_\mathrm{DMI})\cos\psi \quad [9]\ . \tag{71}$$

For BLOCH domain walls, the contributions of the DMI field and the external field to the energy density vary from this formula [27]. The contribution to the energy density and thus to the velocity depends on the relative orientation of the domain wall and the external in-plane field as well as the sign of the DMI [9, 27]. The orientation dependence is considered by the angle ψ between domain wall-normal and external in-plane field and the sign of the DMI affects the sign of H_DMI as shown in Eq. (68).

The asymmetric bubble expansion method is usually performed in MOKE microscopy in the polar configuration of samples with perpendicular magnetic anisotropy. This enables direct visualization of the perpendicularly magnetized domains as well as the asymmetric expansion [9]. The experiment requires a separate, pulsed control of the in-plane and out-of-plane field strengths of the external field. Thereby, the sample is saturated in an out-of-plane direction before a reversely magnetized domain is nucleated in the FOV. This domain is then asymmetrically expanded with several individual oop pulses and in the presence of an ip field, whereby the domain grows typically in the tens of micrometers [9]. More precise details of the experimental operation are discussed in section 3.2.4. The theory and evaluation of the method will be discussed further below.

Arrhenius Creep Law

Applying moderate magnetic fields ($H_\mathrm{ext} \simeq H_\mathrm{C}$) to a perpendicular magnetized thin film sample at room temperature leads to domain wall movement velocities according to the so-called ARRHENIUS creep law

$$v = v_0 \cdot e^{-\zeta\cdot(H_\mathrm{z})^{-\mu}}\ , \tag{72}$$

with a creep scaling exponent of $\mu = 0.25$ [28, 29, 22, 9]. This creep law describes the propagation of an object (here the domain wall) in a disordered potential landscape, which is essentially governed statistically and thus thermally by overcoming local energy barriers [28].

The scaling coefficient $\zeta(\mu_0 \cdot H_\mathrm{ext})$ can be expressed in terms of the in-plane field-dependent

domain wall energy density σ as

$$\zeta = \zeta_0 \left[\frac{\sigma(H_x)}{\sigma(0)}\right]^{0.25} \quad [27] \ . \tag{73}$$

With this scaling coefficient, the ARRHENIUS creep law is expressed as

$$v = v_0 \cdot e^{-\zeta_0 \left[\frac{\sigma(H_x)}{\sigma(0)}\right]^{0.25} \cdot (H_z)^{-0.25}} \quad [27] \ . \tag{74}$$

In principle, the evaluation by the MOKE microscopy enables simultaneous measurement in all directions. However, in the experiment, the domain wall velocities are typically determined along both bubble sides parallel and antiparallel to the externally applied field ($+x$ and $-x$-direction) [9]. Hereby, the angle ψ in Eq. (71) equals zero, simplifying this equation to

$$\sigma(H_x) = \sigma_0 + 2K_\mathrm{D}\lambda - \pi\mu_0 M_\mathrm{S}\lambda\,|H_x + H_\mathrm{DMI}| \quad [9, 27] \ . \tag{75}$$

This equation demonstrates that the domain wall velocity has a minimum at $H_\mathrm{ext} = -H_\mathrm{DMI}$ and is symmetrical around this field strength. The internal DMI field is therefore directly accessible by experimental determination of the velocity minimum.

In some samples, for example with domains possessing large domain wall roughness [9]. In these samples, there may be a pronounced asymmetry around the minimum $H_x \approx -H_\mathrm{DMI}$, i.e., by being flat [9]. Additionally, the asymmetry might not be the strongest parallel to the applied field [9].

In these cases, the model based on the standard creep law is not able to reproduce the domain wall velocity profile. Several other models are known for the description of the asymmetric domain velocity dependence on the external field but adequate classification, of which model is feasible for which case, is missing [9]. A summary of some of these models is shown in Tab. 2. With exception of the most simple, phenomenological quadratic model, all models are extensions of the basic creep law in which additional dependencies of the domain wall energy density are considered. In the third model, a varying domain wall width λ is considered, while the last two models consider the propagation velocity along an arbitrarily chosen angle and thus can describe the propagation in all directions. The difference between the model of arbitrary angle propagation and dispersive stiffness is that the latter also considers an anisotropic energy density dependence, given by the curvature of the domain wall via σ_{xy}.

Since this work is limited to a basic implementation of the method due to time constraints, only the basic creep law has been applied here. In future works, the method might be improved by applying more accurate fit functions, with the ones listed here intended to provide

Table 2: Overview of various fit models for the description of asymmetric bubble expansion velocity in the creep regime based on [9]. Besides the quadratic model, all models are extensions of the basic creep law with modifications in the domain wall energy density. For this reason, only the equation for the domain wall energy is given, which has to be inserted in Eq. (74) [9].

model	**formula**
quadratic	$\nu = \nu_0 \cdot (H_{\mathrm{ext}} + H_{\mathrm{DMI}})^2$
creep law	$\sigma(H_x, \psi) = \sigma_0 + 2K_{\mathrm{D}}\lambda\cos^2\psi - \pi\mu_0 M_{\mathrm{S}}\lambda\,(H_x + H_{\mathrm{DMI}})\cos\psi$
creep law (varying λ)[2]	$\sigma(H_x, \psi, \lambda) = 2\left(\frac{A_{\mathrm{ex}}}{\lambda} + K_{\mathrm{oop}}\lambda\right) + 2K_{\mathrm{D}}\lambda\cos^2\psi - \pi\mu_0 M_{\mathrm{S}}\lambda\,(H_x + H_{\mathrm{DMI}})\cos\psi$
arbitrary angle propagation	$\sigma(H_x, \psi, \theta) = \sigma_0 + 2K_{\mathrm{D}}\lambda\cos^2\psi - \pi\mu_0 M_{\mathrm{S}}\lambda \times [(H_x\cos\theta + H_{\mathrm{DMI}})\cos\psi + H_{\mathrm{x}}\sin\theta\sin\psi]$
dispersive stiffness[3]	$\tilde{\sigma}(H_x, \psi, \theta) = \sigma(H_x, \psi, \theta) + \sigma_{\theta\theta} - \frac{\sigma_{\theta\psi}^2}{\sigma_{\psi\psi}}\varepsilon(\frac{L}{2\Lambda})$

initial assistance.

It should also be mentioned, that sometimes, especially true for samples bombarded with ions, the slope of the domain growth changes more abruptly at higher in-plane fields [9, 30, 11]. This might complicate the fitting procedure.

With the asymmetric bubble expansion method, the sign of the DMI is conveniently determined as long as attention is paid to the mutual direction. For a positively pre-saturated sample and a positive in-plane field, the growth to the left is larger than the growth to the right $v_{\mathrm{l}} > v_{\mathrm{r}}$ for $\mu_0\vec{H}_{\mathrm{x}} > 0\,\mathrm{mT}$, indicating a positive DMI [9]. This behavior was experimentally observed for all domains and therefore all determined DMI values of this work carry a positive sign. For the assignment of the sign of the DMI, the terms $v_{\uparrow\downarrow}$ and $v_{\downarrow\uparrow}$ may be introduced, whereby the arrows indicate the change in the magnetization of the domains separated by the domain walls. I.e., the velocity $v_{\uparrow\downarrow}$ refers to the growth velocity of the NÉEL domain wall separating an upwards and a downwards pointing domain from the left to the right. This definition is thereby coupled to the direction of the in-plane field, which makes the specification of pre-saturation direction redundant. In this work, however, the saturation and velocity direction will always be specified in regard to the setup given in Fig. 9b.

3.2.4 MOKE - Measurement Procedure

The experimental procedure of the domain wall velocity-based method of the asymmetric bubble expansion consists of three separate steps [9]:

1. saturation in one of the two out-of-plane magnetization directions
2. nucleation of a bubble domain with magnetization opposite to the saturation
3. pulsed growth of the bubble domain by simultaneously applying a continuous in-plane field and several out-of-plane field pulses.

The first step just requires a sufficiently large out-of-plane field whose field strength can be determined by an oop hysteresis loop. Therefore, before the actual asymmetric bubble expansion method, this and other initial parameters are identified by performing a standardized measurement of an oop hysteresis loop. These oop hysteresis loop measurements were performed by a short python code, in which the external magnetic field has been altered stepwise and an image was taken at every field step. The field strengths, the associated images, and the mean grayscale values, i.e., intensity, of each image are recorded. Since the grayscale value correlates with the magnetization of the sample surface at the applied magnetic field, a hysteresis curve is generated by plotting the mean grayscale value against the external magnetic field. The other two process steps were way more time-consuming than the first step due to the given domain texture of the samples.
For the saturation, field strengths of about three times the coercive field were applied along the desired magnetization direction. The nucleation and domain growth were performed subsequently with oop pulses of one-second length and opposite field strengths of about 1.2 and 1.1 times the coercive field, respectively. The exact field strength values were determined individually depending on the sample's response. Hereby the decisive factors were, that the nucleated domain is in the center of the image, occupied about 5% of the FOV at the beginning, and reached the area outside the FOV after at least 12 growth pulses without an applied in-plane field.
These conditions are intended to ensure the comparability of the individual measurement series, but they also significantly increased the required measurement time. This is essential because the domains nucleated only with limited reproducibility, which means that the nucleation pulse usually caused an almost unpredictable number of domains with different spatial and size distributions. Another disturbing and time-consuming factor was domains

that grew into the FOV from outside, which is important in the case of high in-plane field strengths and the resulting increased domain wall velocities (see Eq. (74)).

In practice, therefore, a point on the surface was sought that had the highest possible reproducibility in the nucleation of a single domain of the correct size distribution while as few other domains as possible were present in the domain's surroundings. These locations were often associated with isolated surface defects. In some of these locations, no defects have been optically observed, although it might be possible that they were just too small to be observed microscopically or that they were below the sample surface. In total, this process was very time consuming and required the presence of an experimenter who manually reacts to the limited reproducibility and interfering domains. Another time-consuming factor was vibrations and field-induced changes in the sample height, which both could move the sample surface out of the focal plane over time. Therefore, manual readjustment of the focus was required periodically.

With these time-consuming constraints, one measurement of the asymmetric bubble expansion method in one saturation direction typically required a measurement time of 3 to 7 hours with an actively working experimenter. Most of these measurements were carried out with in-plane field strengths in the range of $-150\,\mathrm{mT} < \mu_0 H_\mathrm{x} < 150\,\mathrm{mT}$ with rather large increments of $\mu_0 H_\mathrm{x} = 5$ or $10\,\mathrm{mT}$. Section 7.3 discusses ways to automate this measurement method, which could enable longer periods of measurement time and thus a correspondingly larger number of data points. This should significantly improve the evaluation. Also, shorter oop field pulse durations would be possible, allowing more images per growth velocity data point and thus a more precise averaging procedure. It would also enable measurements in a larger field range since at high fields, the domain would otherwise grow outside of the FOV in one direction after just one growth pulse (see section 4.3.4).

At this point, it should be noted that the pulse duration t_pulse does not correspond to the time t_{H_z} in which the desired oop field H_z is applied because also the time required to reach this field strength $t_{\Delta H_\mathrm{z}}$ is included. Depending on the field strength, this results in an effective time $t_{H_\mathrm{z}}(H_\mathrm{z})$ in which the field is applied, which is less than the specified pulse duration $t_{H_\mathrm{z}} < t_\mathrm{pulse}$. For the sake of simplicity, $t_{H_\mathrm{z}} = t_\mathrm{pulse}$ was assumed here. In future measurements, however, the program code should be adapted accordingly to enable comparable measurements over large pulsed oop field ranges. An integrated magnetometer could contribute to this since it would allow direct observation of the applied field strength.

Within a series of measurements, the oop field strength of all growth pulses is equal, and

therefore, it is expected that $t_{\Delta H_z}$ is approximately constant, which means that t_{H_z} and t_{pulse} differ by a constant factor. This factor should then also be contained in the fits in Fig. 24, whereby this scalar factor should not have an impact on the determination of the minimum. In the normal bubble expansion method, a bubble domain image is recorded after nucleation, which is then subtracted from grown bubble images as a background. This causes the original bubble to appear as a speck in the growth [9]. The resulting subtraction images then contain the growth as a signal. Due to the dendrimeric shape of the domains in these experiments, this method has been expanded by an additional background image in saturation to characterize the originally nucleated domain. This procedure proved to be necessary during the first experiments since the dendrimeric growth is evaluated statistically and a well-characterized nucleation domain is required as a starting point. A schematic overview of the measurement process is shown in Fig. 15, where also a part of the evaluation for extracting the growth velocity is included.

The absolute and relative pixel values of every recorded image are essentially determined by the magnetization, the exposure time, the brightness of the light source, the mutual orientation of the polarizers and the compensator, the focus adjustment as well as the internal gain of incoming signals of the camera. Therefore they might differ for each measurement series. To extract the growth velocity, the images are post-processed in contrast, brightness, and blur [9]. Additionally, they are binarized, allocating growth purely to white pixels (uint8 value of 255) while all others are colored black (uint8 value of 0). This enables convenient localization of the domain as well as statistical determination of the growth velocity. A large part of the work of this thesis went into the image processing procedure for targeted growth extraction. Therefore section 4.3 deals with each step in detail.

The images and growth values can be re-scaled by the pixel size, depending on the utilized set of camera and objective [9]. All MOKE images and growth velocity data in this work were measured with a $50x$ objective with a numerical aperture of 0.8 without further magnification. This configuration results in a conversion factor of $1\,\mathrm{px} = 516\,\mathrm{nm}$, which can be applied to all MOKE images and growth velocities.

Python

Since the original software from EVICO MAGNETICS was not designed to control in-plane and out-of-plane magnets simultaneously, a homemade *Python* program was designed first in the scope of a previous bachelor thesis [26] was applied for all measurements. For the reproducible control of the external magnetic fields, the electromagnets were recalibrated at regular intervals of two months as well as after all changes to the setup. For this purpose, the individual magnetic field components were measured with a magnetometer as a function of the electromagnet's voltage. The resulting measurement series were then fitted to an empirical arc-tangent function. Figure 10 shows an exemplary calibration plot for the in-plane magnetic field component of the electromagnets. The self-written *Python* program

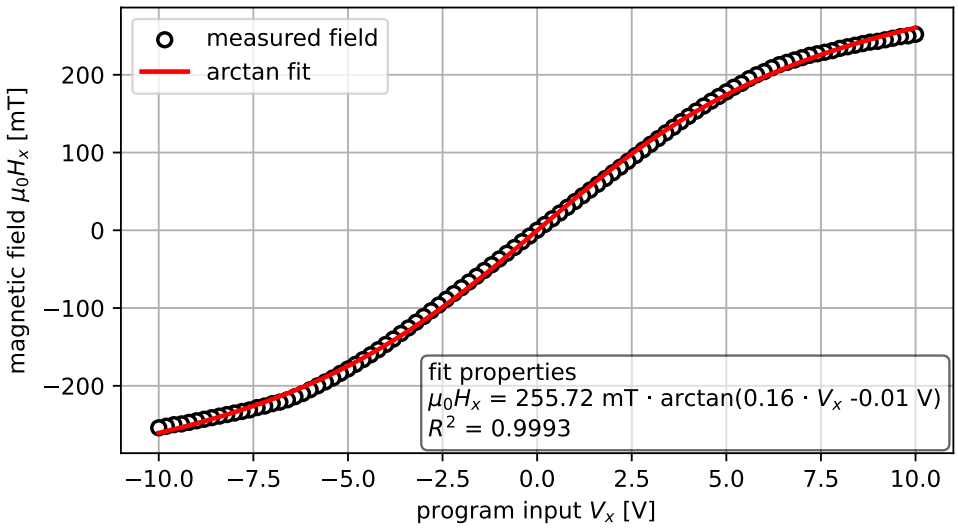

Figure 10: Example for the calibration of the external in-plane magnetic field by fitting experimental measured field strengths against the function $H_x(V_x) = A \cdot \arctan(B \cdot V_x + C)$.

requires a list of field-voltage points from which the output voltage is linearly interpolated by the two field points being closest to the desired field. Therefore, the fit function was utilized to calculate a list of close data points with a short distance of 50 mV or less.

4 Evaluation of the DMI Quantification

In the following sections, the DMI and its sign are determined by extracting the three parameters M_S in section 4.1, K_{eff} in section 4.2, and H_{DMI} in section 4.4 from the experimental data. The dependence of these parameters and thus also of the DMI on the ion dose of the 10 keV He^+ ion bombardment is discussed later in section 6. A special focus is placed on the newly established method, called the asymmetric bubble expansion method in section 4.4 and the associated self-written program for its evaluation in section 4.3. In addition, some other sample properties as well as the feasibility and automatization of the asymmetric bubble expansion method are discussed later on in the section 7.

4.1 Saturation Magnetization

The saturation magnetization M_S is one of the three experimentally available parameters for the determination of the interfacial DMI according to Eq. (52). As mentioned in section 3.1.1, it is contained in the hysteresis curve recorded with the VSM, whereby its extraction requires additional information about the ferromagnetic sample volume V_{FM}.

For the determination of the saturation magnetization, the hysteresis loops of three pieces of the same sample, with thus almost no sample-to-sample variation, have been measured in dependence on the rotation angle α_{VSM} (see Fig. 6). One of these measurements of the magnetization component parallel to the external field $m_{\parallel}$ is depicted in Fig. 11 for a rotation angle of $\alpha_{VSM} = 0°$. With this alignment, the depicted hysteresis curve represents the macroscopic magnetization properties in the out-of-plane direction of the sample system. The hysteresis curve in Fig. 11 possesses a small linearly increasing component, which may be caused by paramagnetic material with a positive magnetic susceptibility [14] or an overcompensation of diamagnetic material like silicon. A small increasing slope might also originate from thermal fluctuations which counteract the alignment due to the Zeeman energy term in an external applied magnetic field. This counteracting behavior becomes less important with increasing field strength, giving rise to a small positive susceptibility in saturation [14]. Additionally, the external field strengths are distorted in the form of a linear shift in the field strength in some of the stored hysteresis files. These linear shifts were not visible in the built-in Hall probe during the measurements. Therefore, it is assumed that the measurement procedures themselves have been successful. The origin of the distortion could not be located. The distortion was only noticed after the ion bombardment of the samples, which

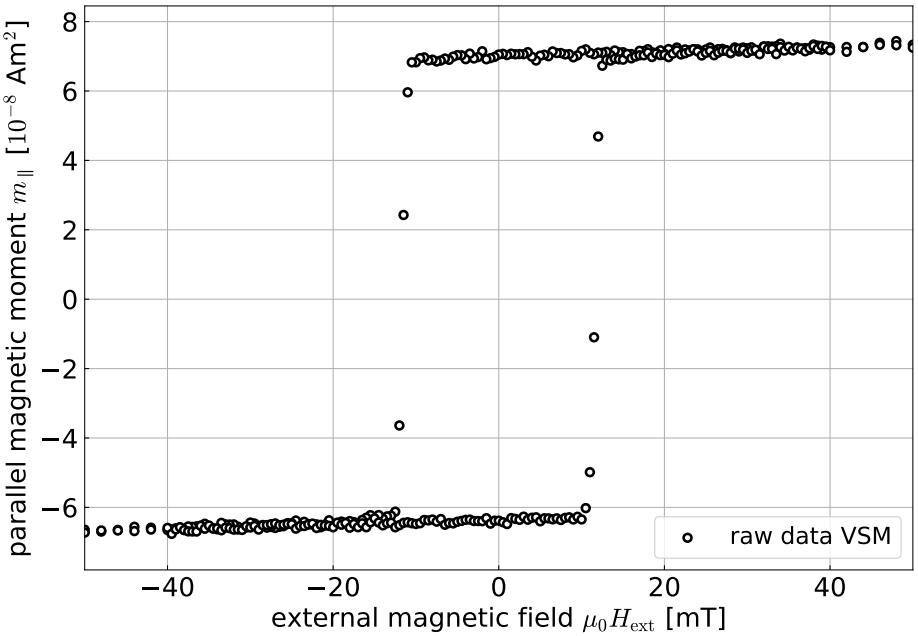

Figure 11: Exemplary raw data of an out-of-plane hysteresis loop measured with the VVSM with a rotation angle of $\alpha_{\text{VSM}} = 0°$.

makes it impossible to repeat the measurements of the same non-bombarded sample material and there was not enough sample material to completely repeat this measurement procedure. Nevertheless, to correct the distortions and comparably interpret all measurement data, all VVSM measurements have been processed equally according to the following criteria:

1. The post-processed VVSM hysteresis curves have to possess a large agreement with the MOKE-magnetometric measurements. Since the performed MOKE-magnetometry is not able to quantify the magnetic moment in absolute values, the hystereses are only compared in shape (qualitatively), coercive field, and saturation field strength H_{S}

2. For the investigated ferromagnetic material in the VVSM, a point-symmetrical hysteresis curve is expected due to the uniaxial perpendicular magnetic anisotropy (PMA). This also applies to the DMI. As long as no additional asymmetry is introduced, for example, by a triangular shape, the interfacial DMI is not expected to alter the macroscopically determined hysteresis curve asymmetrically [31]

3. In the experiment, the external magnetic field is applied in a symmetrical loop. Therefore, a value of 0 mT should result as the equally weighted average over all field strengths if their sign is taken into account. Minor deviations might occur as part of measurement inaccuracies and field fluctuations.

The performed MOKE magnetometry only enables the measurement of out-of-plane hysteresis curves due to the lower maximum in-plane field strengths of around $\mu_0 \cdot H_{\mathrm{x,\,max}} \approx 250\,\mathrm{mT}$ in the KERR microscopic setup, which has been insufficient for achieving in-plane saturation. The first processing criterion was thus solely verified via the out-of-plane hysteresis curves of both methods. For the processing procedure according to the aforementioned criteria, the hysteresis curve was firstly separated into a descending (increasingly negative field strength) and an ascending strand (increasingly positive field strength). A complete magnetic reversal between both saturations takes place in both strands. First, the slope was calculated by

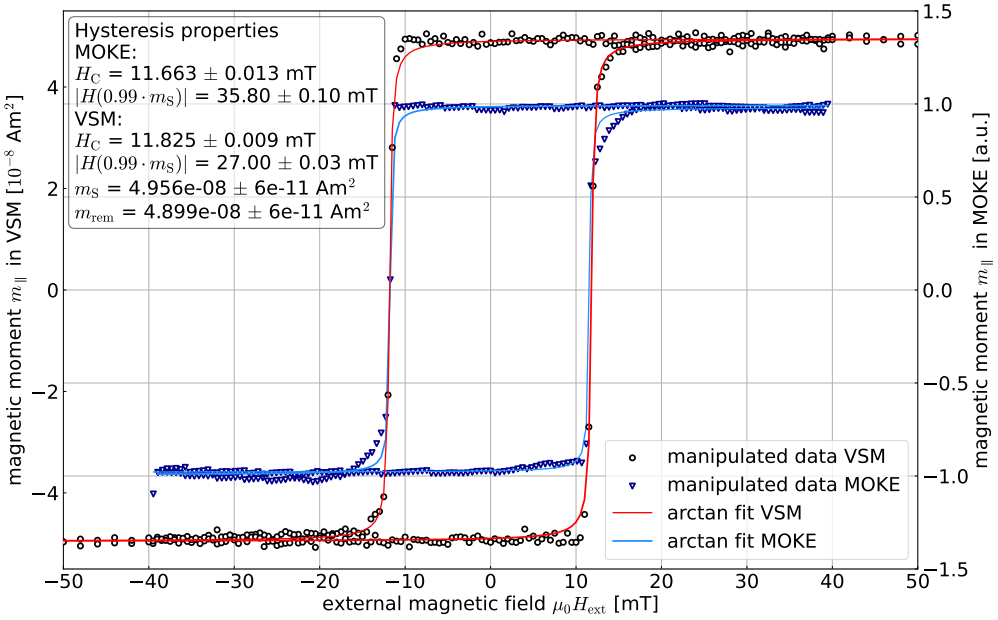

Figure 12: Comparison between out-of-plane hysteresis curves measured with the VVSM (dark circles, red fit) and the MOKE (blue triangles, light blue fit). The most important parameters are calculated based on fitting each strand individually to the empirical fit functions mentioned in the upper left corner.

fitting both saturated regions to a linear equation, whereby the mean slope was then subtracted from the whole hysteresis curve. Afterward, the second and third criteria are met by reducing the field strengths and magnetic moments of both strands by their mean values. This ensures $\mu_0 \overline{H}_{\mathrm{ext}} = 0\,\mathrm{mT}$ and $-m(-H_{\mathrm{ext}}) = m(H_{\mathrm{ext}})$ within measurement inaccuracies. The resulting hystereses have been compared to the MOKE magnetometric out-of-plane hystereses, whereby an exemplary comparison is depicted in Fig. 12. The MOKE magnetometric hystereses have been post-processed as well by eliminating the disturbing magneto-optical FARADAY effect via subtraction of the field-dependent parts of a quadratic function with a

predominantly linear component fitted to the saturated regions. Both, the processed MOKE and VSM hysteresis curves, were fitted strand dependently with an arc-tangent function which empirically possesses a good description for most hystereses loops [12].

As mentioned in the first criterion, the out-of-plane hysteresis curves have been qualitatively compared by their shape as well as quantitatively by the coercive fields and the saturation field strength $H_{\mathrm{S}} = |H(\pm 0.99 \cdot m_{\mathrm{S}})|$, which was here defined by the absolute field strength at which the fit reaches 99% of its minimum or maximum value, depending on whether the descending or ascending strand is considered.

In general, all three comparison parameters are quite similar, even if they do not agree with each other within their assigned uncertainties. However, these minor deviations are most likely attributed to the fact that the MOKE magnetometric method observes the surface magnetization in a limited area of the sample visible within the FOV, while the VVSM method detects the magnetization integrated over the entire ferromagnetic material volume. Smaller deviations might therefore occur due to slightly varying sample compositions and properties as well as the difference between surface magnetization and volume averaged magnetization. It is therefore assumed that the post-processing successfully compensates for the distortions of overcompensation and field shift but does not distort the measured physical properties.

Based on the strand-dependent arc-tangent fits, the component of the magnetic moment in saturation m_{S} and remanence m_{rem}, the coercive field H_{C} and the work carried out by the magnetic reversal E_{hyst}, quantified by the area enclosed by the hysteresis, have been extracted as important properties, of the parallel and perpendicular arranged coils. The following evaluation will solely focus on the components of the magnetic moment in saturation m_{S}.

The saturated magnetic moment is a vectorial quantity and geometrically determinable from both saturated individual components $m_{\parallel,\,\mathrm{S}}$ and $m_{\perp,\,\mathrm{S}}$, which are arranged orthogonal to one another according to the biaxial arrangement of the pickup coils in the VVSM (see Fig. 6). With this alignment, the total saturated magnetic moment results from the square root of the sum of the individual components squared according to the Pythagorean theorem

$$m_{\mathrm{S}} = \sqrt{m_{\parallel,\,\mathrm{S}}(\alpha_{\mathrm{VSM}})^2 + m_{\perp,\,\mathrm{S}}(\alpha_{\mathrm{VSM}})^2} \quad [17] \; . \tag{76}$$

The components of the magnetic moment in saturation are dependent on the rotation angle α_{VSM}. The saturated magnetic moment has been determined for each angle based on its geometric correlation in Eq. (76). This equation requires saturation for all angles for both, the parallel and the orthogonal component. The appendix section 9.2 exemplarily displays

the summarized data of the hysteresis loops of one of the three samples in Fig. 51 and Fig. 52, which state that this saturation condition is met in all measured cases. The saturated magnetic moment $\overline{m_S}$ was then determined by averaging all angle-dependent calculated components of the magnetic moments, which is shown graphically in Fig. 13. In theory, the

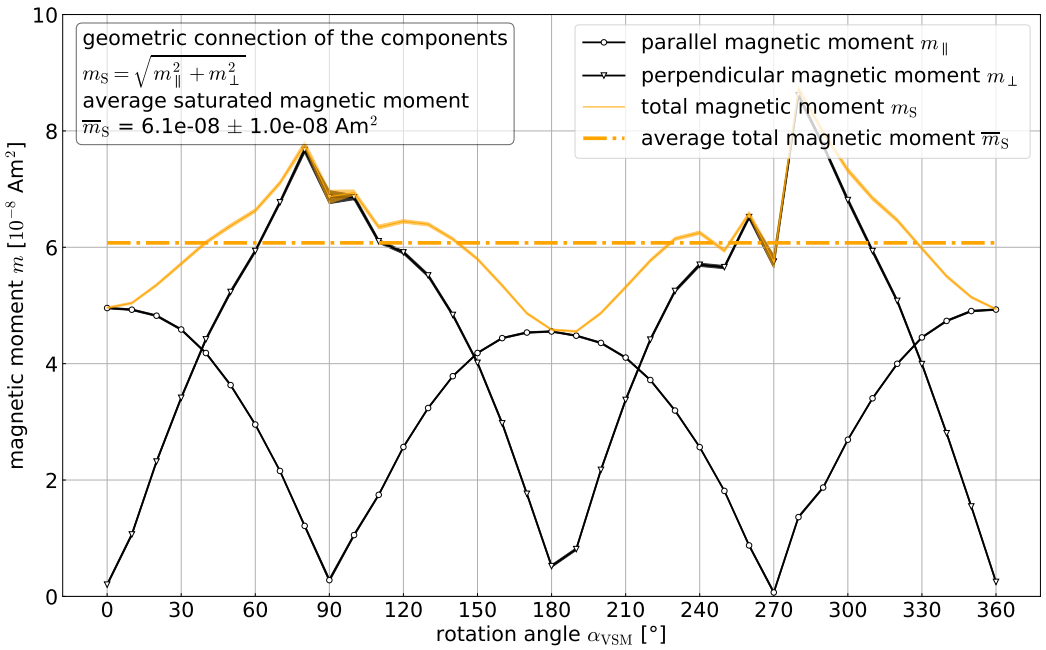

Figure 13: Component of the saturated magnetic moment parallel ($m_\parallel$, circles) and perpendicular ($m_\perp$, triangles) to the external field H_{ext} in absolute values and in dependence on the rotation angle α_{VSM}. Additionally, the total (orange, continuous) and average magnetic moment (orange, dashed) based on Eq. (76), is displayed angle dependently.

saturated magnetic moment should remain constant over all angles within the measurement inaccuracies [17]. However, it turns out that this is not true. In general, both components possess a comparable shape, shifted by $\frac{\pi}{2} = 90°$, whereby the perpendicular component has a higher maximum than the parallel component, which also appears a bit more peak-like. This results in an angular dependency for the magnetic moment, which roughly follows its perpendicular component. However, since saturation has been achieved for all angles and both components (see appendix section 9.2), it is assumed here that this discrepancy was caused either by post-processing, the missing measurement of the third spatial component parallel to the glass rod, or incorrect calibration. In the case of the calibration, two device-internal correction or weighting factors for the components in the parallel and perpendicular directions must be determined in a calibration step using a Ni calibration sample with a known magnetic moment in saturation. Errors in these factors would directly affect their respective

component. Since saturation is achieved in all hysteresis loops, a uniform magnetization is assumed, which was determined as the mean value of the angle-dependent magnetic moments in saturation.

The determination of the saturation magnetization out of this average magnetic moment in saturation is based on Eq. (56), in which the ferromagnetic volume is separated into the layer thickness and sample area. While the layer thickness is ideally known from the nominal layer system in Fig. 4 and amounts to $t_{\mathrm{FM,\,nom}} = 6.8\,\mathrm{nm}$, the sample surface area was experimentally accessed via optical microscopy. Thus, the surfaces of the samples have been experimentally identified with high precision via optical microscopy with a confocal laser scanning microscope (CLSM) of the company KEYENCE. The recorded optical images and their detailed evaluation procedure are described in appendix section 9.1, while Tab. 3 summarizes the determined areas based on this method.

Table 3: Surface areas and magnetic moments of the samples utilized in the VVSM experiments. The surface areas are determined by optical microscopy with a detailed description in appendix section 9.1. The magnetic moments are extracted and averaged as described in Fig. 13. It is noteworthy that sample 1c has a smaller surface area but larger magnetic moment than sample 1a. Sample 1c also deviates the most from a square in shape, which can have an impact on this.

sample label	**1a**	**1b**	**1c**
surface area A	$1.458\,\mathrm{mm}^2$	$1.777\,\mathrm{mm}^2$	$1.344\,\mathrm{mm}^2$
magnetic moment m	$5.48 \cdot 10^{-8}\,\mathrm{A\,m}^2$	$6.68 \cdot 10^{-8}\,\mathrm{A\,m}^2$	$5.88 \cdot 10^{-8}\,\mathrm{A\,m}^2$

Furthermore, the saturation magnetization for samples with the same nominal multilayer system and fabrication process is known and amounts to $M_{\mathrm{S,\,nom}} = 600\,\mathrm{kA\,m^{-3}}$ [16]. Due to typical small variations between samples produced with the same fabrication process, both nominal values for the layer thickness and the saturation magnetization might not represent the actual properties of the investigated sample system accurately. Since neither of the two quantities can be determined unequivocally without an additional suitable experimental method, they both are estimated here based on their nominally expected values.

For this purpose, a pair of saturation magnetization M_{S} and layer thickness t_{FM} values is calculated which possesses the smallest relative deviation from the provided nominal values while simultaneously amounting to the saturated magnetic moments in the VVSM measurements. For the latter condition, the microscopically determined sample areas in Tab. 3 have been included. The calculation was performed by the simple minimization function $f_{\mathrm{min}}(M_{\mathrm{S}}, t_{\mathrm{FM}})$

which is the sum of the relative deviations from the nominal values

$$f_{\min} = \Delta M_{\mathrm{S}} + \Delta t_{\mathrm{FM}} = \frac{M_{\mathrm{S}}}{M_{\mathrm{S,\,nom}}} + \frac{t_{\mathrm{FM}}}{t_{\mathrm{FM,\,nom}}} = \frac{M_{\mathrm{S}}}{M_{\mathrm{S,\,nom}}} + \frac{m_{\mathrm{S}}}{M_{\mathrm{S}} \cdot t_{\mathrm{FM,\,nom}} \cdot A}\,. \tag{77}$$

The pair of values satisfying this minimum is $M_{\mathrm{S}} = 591\,\mathrm{kA\,m^{-3}}$ and $t_{\mathrm{FM}} = 6.7\,\mathrm{nm}$ which thus both deviates from their nominal values by -1.4%, respectively. In addition, there is a deviation of up to 8%, which corresponds to the standard deviation of the angle-dependent saturation magnetization.

4.2 Effective Magnetic Anisotropy

The magnetic anisotropy is the second experimentally available parameter required for the interfacial DMI quantification as stated in Eq. (52). It can be determined from a torque curve measurement as described in section 3.1.2. As also described in this section, the torque curve measurements are recorded simultaneously with the component-wise hysteresis curves of the previous section due to the biaxial alignment of the pickup coils in the VVSM. The perpendicular magnetization component $m_{\perp}$ is directly related to the macroscopic torque L acting on the magnetic dipole moments via Eq. (62) [17]. For feasible torque curve measurements, it is crucial to ensure that sufficient magnetic field strength is chosen so that a uniform magnetization is present [25]. The hysteresis curves in section 9.2 in the appendix display that this condition is only met at absolute field strengths above 300 mT due to the hard axis at $\alpha_{\mathrm{VSM}} = 90°$ and 270°. For this reason, a field strength of $\mu_0 \vec{H}_{\mathrm{ext}} = 300\,\mathrm{mT}$ is chosen for the torque curve measurement, since then the perpendicular magnetization is also almost saturated for the hard axis cases and the condition of uniform magnetization is sufficiently met [25].

However, the hystereses at most rotation angles were only measured in the field strength range up to 100 mT, which is why the perpendicular magnetization component at 300 mT is not experimentally accessible for these angle ranges. However, since the saturation is achieved well below 100 mT for all angles in question, the magnetization at 300 mT is extrapolated as being equal to the magnetization at 100 mT. This extrapolation is based on the assumption that the magnetization in saturation is not or only negligibly changing with increasing external field strength. Besides this extrapolation of the magnetization, another additional assumption is made for the torque curve: The magnetization of the selected, partly extrapolated field strength is uniform which contradicts the angle-dependent variation of the saturation magnetization in Fig. 13. Therefore, this variation is eliminated via normalization by dividing the

angle-dependent magnetic moment $m(\alpha_{\mathrm{VSM}}, 300\,\mathrm{mT})$ by the associated saturated magnetic moment $m_{\mathrm{S}}(\alpha_{\mathrm{VSM}})$ and multiplying it by the average magnetic moment $\overline{m} = 6.1 \cdot 10^{-8}\,\mathrm{A\,m^2}$. The resulting torque curve is displayed in Fig. 14 with two fits representing the magnetic anisotropy as the first two orders of the sin-function power series of Eq. (46). In principle,

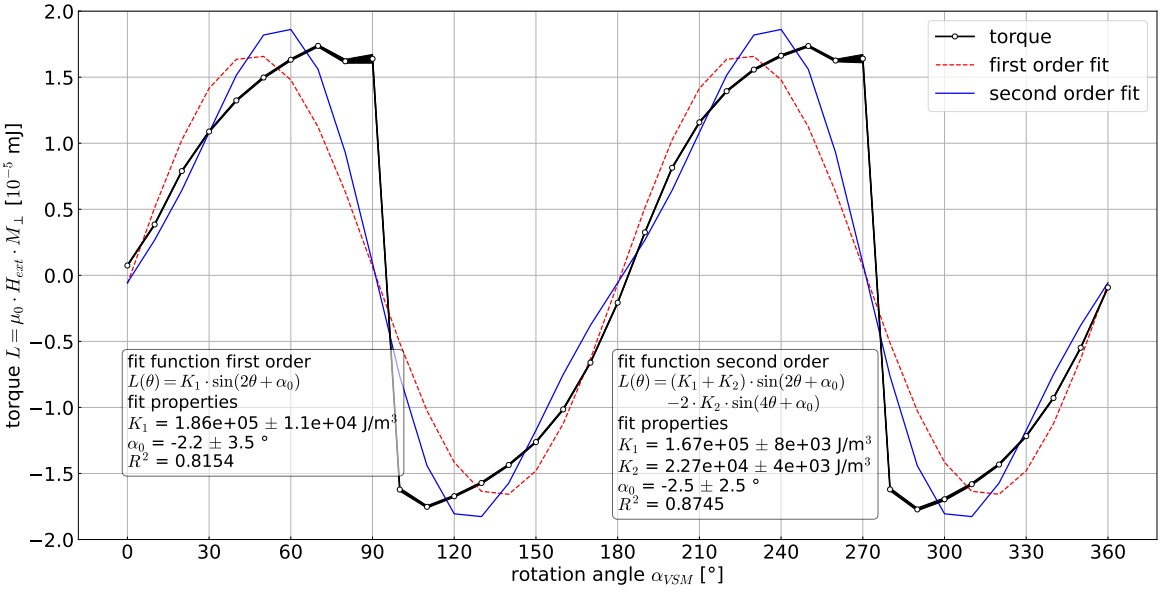

Figure 14: Extrapolated torque curve $L(\theta, 300\,\mathrm{mT})$ with a normalized uniform magnetization as well as two fits corresponding to the first derivative of the first two orders $f_{\mathrm{anis}}^{(1)}(\theta)$ and $f_{\mathrm{anis}}^{(2)}(\theta)$ of the sin-function power series of Eq. (46).

the measurements were aligned so that an angle of $\alpha_{\mathrm{VSM}} = 0°$ corresponds to a parallel arrangement of the easy axis with the external magnetic field and thus the torque should be zero at this angle. Since this alignment was performed by eye, it might be accompanied by uncertainty. Thus, the analytical derivative in Eq. (63) has been expanded by a correction angle α_0. It corresponds to the misalignment between the easy axis and the alignment of $\alpha_{\mathrm{VSM}} = 0°$. Both fits agree to a deviation of about 2° along the specified clockwise rotational movement. This rather small deviation shows that the alignment by eye did work within the large rotational steps of 10° and the correspondingly low number of points. Both fits of the different power series agree that the main component of the magnetic anisotropy, i.e., the first anisotropy constant K_1 is about $2 \cdot 10^5\,\mathrm{J\,m^{-3}}$ which perfectly meets the provided anisotropy constant in [16]. Since a higher power series should generally represent the properties better and the second-order fit has a noticeably higher coefficient of determination, the coefficient K_1 of the second-order fit is more likely to represent the properties of the sample. However, with the effective magnetic anisotropy K_{eff}, the anisotropy is reduced to a single parameter

and thereby to the first power series. Thus, the effective magnetic anisotropy might agree more with the fit of the first power series. To include both arguments, the effective magnetic anisotropy K_{eff} is determined as the mean value of the K_1 parameters of both fits.

4.3 Post-Processing of MOKE Images

The domain growth velocity required for the asymmetric bubble expansion method may be calculated by dividing the growth of a domain along the in-plane field direction by the pulse duration of the pulse that caused this growth. The requirements for the domain images and field pulses have already been addressed in sections 3.2.3 and 3.2.4.

Thus, in each image, the nucleation or growth as well as the withdrawing domain has to be recognized. For clarity, the withdrawing domain is referred to as the background domain in the rest of this work. Since each asymmetric bubble expansion series consist of 400 to 800 images for each saturation direction, an automatized recognition is favorable, especially if automatization of the measurement procedure can be achieved as well, which would lead to an increased amount of images. Therefore, this evaluation approach involves the process of image post-processing which finally terminates with a discretization that assigns pixels to the nucleation/growth or the background. The domain growth velocity is then calculated based on these discretized images. The first step in the image post-procession involves the

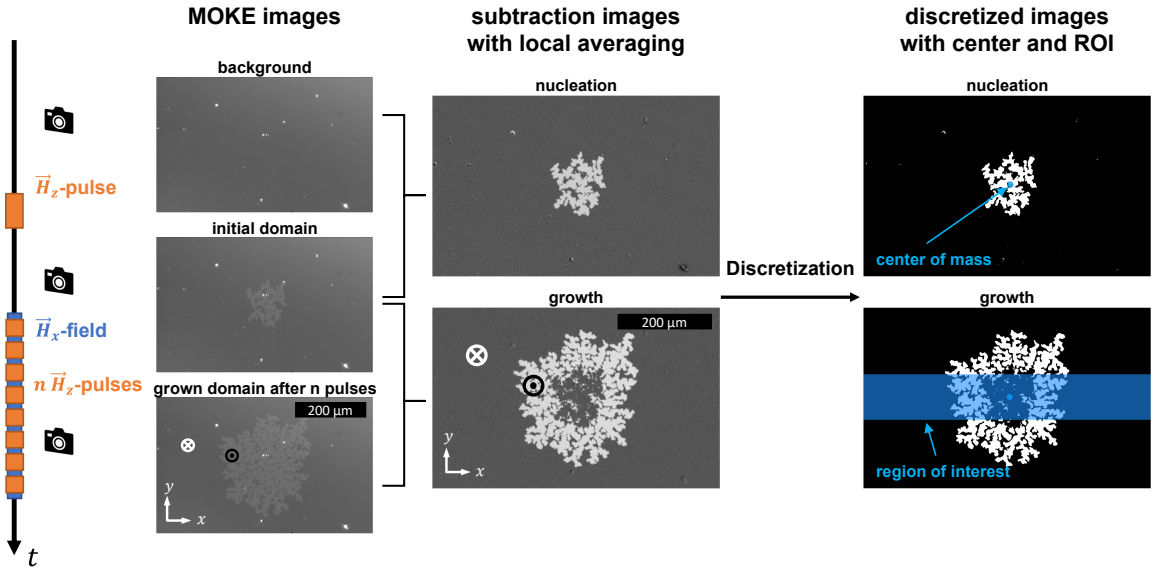

Figure 15: Overview of the individual image recording and post-processing steps. The time axis on the outermost left displays the measurement procedure in a simplified manner. The post-processing steps are ordered from left to right and include contrast enhancement via subtraction and local averaging, discretization for domain recognition, and finally the growth calculation.

subtraction of two consecutive images that are separated in the experiment by a nucleation or growth oop pulse. Since the samples possess a strong perpendicular magnetization anisotropy, solely two oop domains consist of either upwards or downwards magnetization, respectively. This means that there are also only two possibilities for the pixels in the subtraction images:

1. Pixels conserving their oop magnetization. Hereby the signals before and after are practically equal and thus cancel each other out in the subtraction image. These pixels mainly contain the background domain and therefore these are simply called "the background" for the rest of the work. This background also includes the part of the growing domain that was already present before the considered pulse

2. Pixels changing their oop magnetization from either up to down or from down to up depending on the pre-saturation of the sample. Hereby, the absolute signal increases strongly due to the subtraction. These pixels contain the information of nucleation and growth and are thus called "growth pixels" or just "the domain" for simplicity.

Accordingly, the subtraction images display the changes compared to the previous images, which is optimal for the experiment performed here, since the resulting images directly contain the nucleation or the growth of the domain associated with the pulse. Assigning each pixel to the background or the domain enables the determination of the location, area, and growth based on the recorded MOKE images.
The following subsection will hereby discuss this automatized assignment procedure as well as the determination of the growth of the dendrimeric domains. The individual steps are shortly summarized in the overview in Fig. 15.

4.3.1 Enhancement of Kerr Contrast

The images recorded in the MOKE microscopy are contrast images and therefore typically grayscale images. For this reason, the contrast essentially determines the image quality and the visibility of displayed domains [21, 17].
A common method to increase this often called KERR contrast is the aforementioned subtraction or division of two consecutive images [21, 17]. As a result, the background illumination of the image and surface impurities are strongly suppressed. Additionally, this also eliminates signals of constant magnetization, which means that only changes in the sample are visible in the resulting images. This essentially involves changes in magnetization in particular but also e.g., thermal drifts or changes in the illumination.
Nonetheless, the remaining signal practically only consists of changes in magnetization with enhanced visual contrast and therefore this method is perfectly suited for displaying magnetodynamic phenomena including the domain expansion to be examined here [9].
In this specific case of determining the asymmetric pulse-governed domain growth velocity, the image subtraction method is applied to extract the growth caused by each individual out-of-plane pulse, via subtraction of the corresponding image before the pulse. Two consecutive images displaying the domain before and after a sequence of three pulses as well as the subtraction image extracting the growth information are shown in Fig. 16. The difference between three consecutive growth pulses is here just selected to enhance the visualization of the growth. In the actual evaluation, consecutive images, separated by one growth pulse are always subtracted from each other to reduce the impact of, for example, thermal drifts in the focus or the image plane. In principle, the evaluation is also possible by subtracting the nucleation domain from all growth images.
For the subtraction simply the difference in each pixel's grayscale values is taken which is possible because the grayscale values of the raw MOKE images are taken in absolute values from 0 to 4095 displaying the intensity and therefore the magnetization. This method is not or at least less applicable for images with pixel values I_{ij}, with the pixel indices i and j, displaying the relative brightness or intensity (e.g., 0 for the darkest pixel and 4095 for the brightest pixel)

$$I_{ij,\,\mathrm{subtraction}} = \Delta I_{ij} = I_{ij,\,\mathrm{after}} - I_{ij,\,\mathrm{before}}\,. \tag{78}$$

Ideally, two distinct grayscale values should be visible in the images in 16, which represent the changed and persistent magnetization as addressed in the last section. In addition, in-

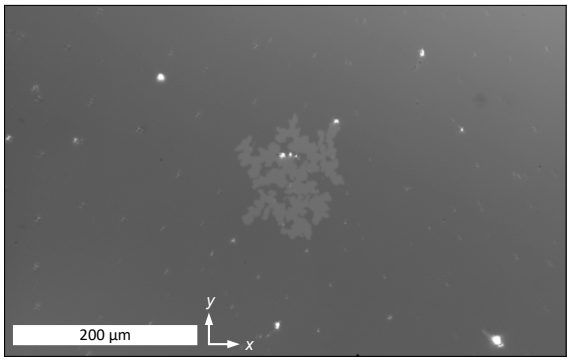

(a) Image of the initial nucleation domain with the intensity I_{before}.

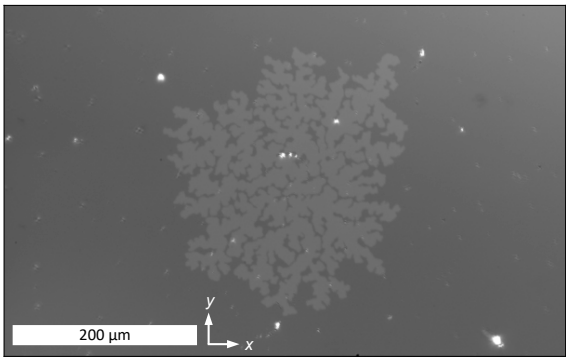

(b) Image of the grown domain after three out-of-plane pulses with the intensity I_{after}.

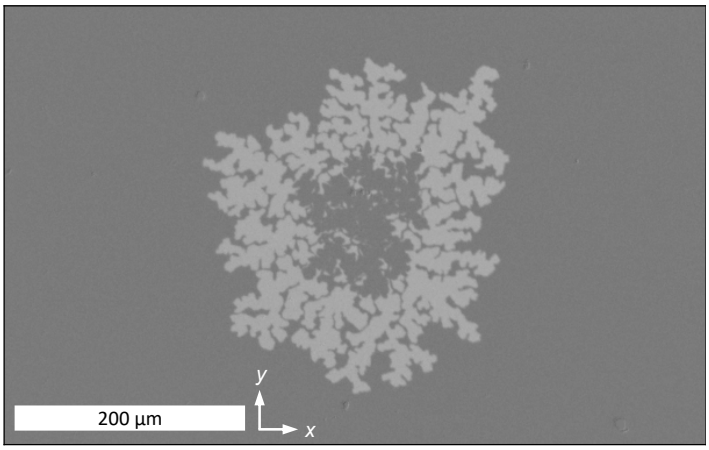

(c) Extraction of the domain growth by subtracting Fig. 16a from Fig. 16b. The intensity of the pixel $I_{ij,\,\text{subtraction}}$ with the indices i and j is given by Eq. (78).

Figure 16: Exemplary extraction of the domain growth in 16c via image subtraction of the MOKE images 16a and 16b.

termediate gray levels should appear in the intermediate areas between two domains, which is partly due to domain walls and partly due to the pixel representing a certain surface area over which the surface magnetization and thus the grayscale value is integrated.

In real MOKE images, however, these signals are noisy, which is reflected in broadened gray scale regions, whereby the noise is mainly caused by statistical phenomena like non-homogeneous sample composition, illumination fluctuations, background light, and camera noise and therefore the signals resemble GAUSSIAN broadened peaks.

By applying a local averaging procedure, i.e., blurring via a 2D-Filter, the signal broadening is reduced by maintaining most of the local information. However, this method will disadvantageously result in widened domain walls due to the averaging over two different domains

or as in this case conserved and changed magnetization. However, this disadvantage is acceptable because it only affects a few pixels, and the resulting narrow distinct GAUSSIAN peaks of the background and the domain are favorable for the next step of automatized domain recognition via the grayscale assignment, i.e. discretization. For the local averaging a

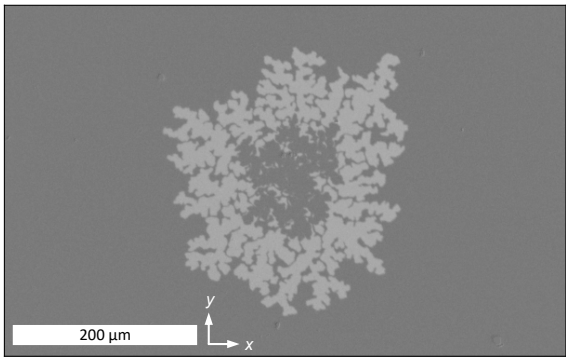

(a) Unprocessed subtraction image.

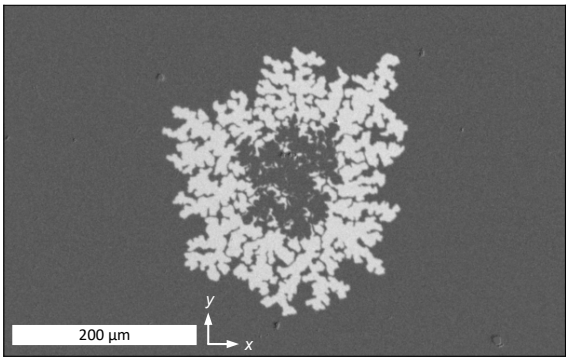

(b) Subtraction image after local averaging.

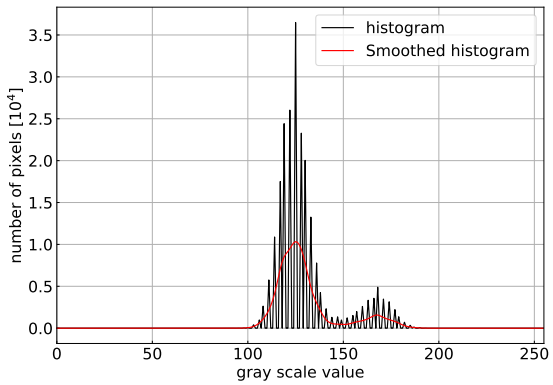

(c) Histogram of the unprocessed subtraction image.

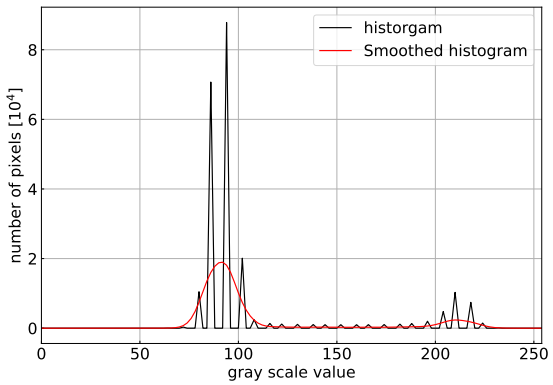

(d) Histogram of the locally averaged subtraction image.

Figure 17: Example for the local averaging procedure utilizing a GAUSSIAN 2D Filter which narrows the distinct GAUSSIAN peaks in relative grayscale values.

GAUSSIAN 2D Filter is applied by convolution of the image with the kernel

$$\frac{1}{273} \cdot \begin{pmatrix} 1 & 4 & 7 & 4 & 1 \\ 4 & 16 & 26 & 16 & 4 \\ 7 & 26 & 41 & 26 & 7 \\ 4 & 16 & 26 & 16 & 4 \\ 1 & 4 & 7 & 4 & 1 \end{pmatrix}, \tag{79}$$

which is essentially a normalized 5×5 GAUSSIAN-weighted matrix. In principle, other odd-dimensional GAUSSIAN matrices are also possible for the convolution step. Hereby, a larger

matrix is able to suppress noise more efficiently, but at the same time, local information is increasingly lost. The 5×5 dimensionalities of the convolution matrix ere decided to be a good compromise between these two factors.

Possibilities for convolution with other matrices have been implemented into the code and also tried out, such as convolution with an unweighted kernel, which is equivalent to a local unweighted averaging procedure. However, the 2D filter with GAUSSIAN weighting was chosen because the local information is well preserved here.

Comparing Fig. 17a to Fig. 17b presents an increase in the contrast which corresponds to the larger peak-to-peak distance in the histograms in Fig. 17. It is important to emphasize that averaging is a purely mathematical operation that does not change the underlying physical phenomena. Therefore, for example, both of the left-hand peaks in the histograms in Fig. 17 display the same, darker background and their peaks should represent approximately equal absolute values. However, displaying the images in relative instead of absolute values increases the contrast because the averaging procedure effectively eliminates the most extreme absolute values. This allows the remaining values to be expressed in relative terms with greater contrast, i.e., GAUSSIAN peaks with a larger peak-to-peak distance in relative values but the same peak-to-peak distance in absolute values as for Figs. 17c and 17d.

It is also very noticeable that instead of displaying GAUSSIAN peaks, the histograms resemble a collection of individual peaks whose envelope is reminiscent of GAUSSIAN peaks. This is most likely caused by the unusual storage format of the MOKE camera where the pixels are assigned to values between 0 and 4095 (uint12). Typical image storage formats include pixel values from 0 to 255 (uint8) or 0 to 65535 (uint16). Upon conversion between the storage formats, there seems to occasionally appear an incorrect assignment, which means that certain pixel values are not displayed at all and neighboring ones are displayed much more frequently, i.e., with a much higher intensity. The reason for this could not be determined.

In the next step of domain recognition, continuous GAUSSIAN-like peaks are required and therefore, the histogram is smoothed using a GAUSSIAN 1D filter with a variance of $\sigma = 2.5$ as default. This slightly widens the peaks, but the discontinuous pixel distribution makes this step inevitable. It has to be clearly pointed out here that this smoothing is only applied to the histogram, but not to the image. This step is only applied to ensure that the program can handle the discretized histograms better in the next step of discretization. Accordingly, the next step only involves the smoothed histograms.

4.3.2 Binarization of MOKE Images

The two GAUSSIAN peaks in Fig. 17c and 17d arise from the changed and preserved directions of magnetization. A clear assignment of these peaks to the change and the preservation, therefore, results in a clear assignment of each pixel to the background or the domain growth. This assignment is based on comparing the grayscale value of each pixel to a threshold.
Applying this assignment procedure of domain recognition terminates with the individual pixels receiving the grayscale values 0 (black) for the background and 255 (white) for the domain growth in dependence on whether their grayscale value is below or above the threshold. In addition, the coloring based on the threshold depends on the pre-saturation of the sample, since the growth should be colored white in all cases. Due to the assignment of two distinct pixel values in this type of discretizing domain recognition, it will be referred to as binarization of the MOKE images for the rest of this work.
This process is based on the evaluation of the smoothed curve shown in the histogram in Fig. 17d. First of all, the local maxima of the two distinct peaks are identified. Then the smoothed histogram is fitted to the sum of two distinct GAUSSIAN peaks, with the position of the maxima of the GAUSSIAN functions being determined and fixed within a 5% deviation by the previously identified peaks.
After a successful fit with a coefficient of determination of typically at least 0.8, the local minimum of the fit function between the two identified peaks, i.e. maximum positions, is determined and set as the threshold value for the binarization assignment. With this threshold, the two GAUSSIAN distributions can be assigned to either the change or the preservation of the magnetization direction if the distance between the GAUSSIAN distributions is sufficient. For this reason, the step of local 2D averaging leads to a significant improvement of the method because the distributions get narrower and more distant from each other if displayed in relative values. For negative saturation, grayscale values below this threshold are colored black and pixel values above this threshold are colored white, as shown in Fig. 18 so that the domain growth is colored in white. For positive saturation, this coloring is reversed. The saturation direction (neg for negative saturation and pos for positive saturation) is an input value in the python program. Due to inhomogeneities in the illumination of the FOV and focus drifts, some images have an additional gradient in their grayscale values, which results in the false allocation of pixels, especially in the outermost edges of the image which then most of the time display an increase in brightness. Therefore, the determined threshold is arbitrarily shifted to lower grayscale values if the peaks possess a distance larger than the doubled

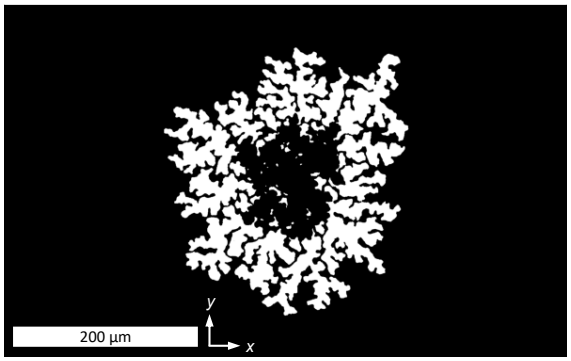

(a) Binarized image of the growth visible in Fig. 16c.

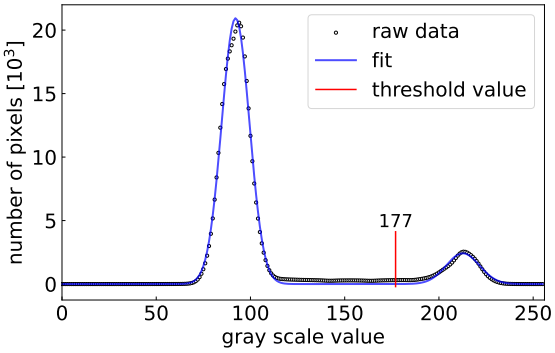

(b) Smoothed histogram of the image in Fig. 17b with the fit of two summed GAUSSIAN peaks and the threshold value for binarization.

Figure 18: Example of the determined threshold between two GAUSSIAN peaks corresponding to the two imaged magnetic domains. Here, all pixels to the right of the threshold value correspond to the growing domain and are colored in white in Fig. 18a and all other pixels are colored in black.

sum of the FWHM (full width at max half) of both GAUSSIAN peaks. A determination of the threshold for the image in Fig. 17 is exemplarily shown in Fig 18.

4.3.3 Growth Determination

The ARRHENIUS creep law in its basic form in Eq. (72) effectively describes domain wall velocity parallel and antiparallel to the externally applied magnetic in-plane field. Thus, with experimental knowledge about the field-dependent domain wall velocities parallel and antiparallel to the in-plane field, which is parallel to the x-axis in the images, the DMI field H_{DMI} is determinable by fitting the function to these experimental values.

The domain is always placed close to the middle of the image by experimental means. Thus, the growth parallel and antiparallel to the field can be converted into growth to the right and the left, depending on its sign. With a positive in-plane field, the growth to the right corresponds to the growth parallel to the applied field.

Since the exact position and shape of the nucleation domain may vary, the growth is always determined along the pixel line parallel to the x-axis which contains the center of mass of the nucleation domain. The center of mass is determined individually for each nucleation domain. For the calculation of the center of mass, the pixels are treated as individual mass points and their gray value as the associated mass. As a result of the binarization, the background pixels possessing a mass of 0 can be neglected. Hence, only white-colored pixels of the nucleation

domain contribute to the center of mass with each holding the same mass of 255. Therefore, calculating the center of mass of the binarized images leads to the identification of the domain center which is the starting point for determining the growth. In the evaluation program, the center of mass is determined once for each nucleation image, and its coordinate is then applied as the starting point for determining the growth in all subsequent growth images of this nucleation domain. For the calculation of the center of mass, the open source package *OpenCV* with its optimized *cv2.moments()*-function is utilized [32]. However, the growth

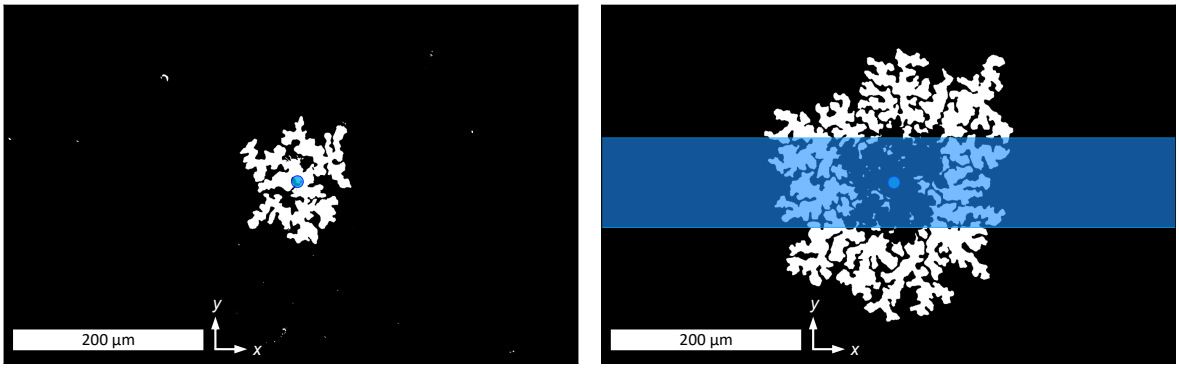

(a) Binarized nucleation image with its center of mass determined with the function *cv2.moments()* of *OpenCV* [32].

(b) Binarized growth image with the center of mass from Fig. 19a and the ROI for calculating the average growth.

Figure 19: Example of binarized images displaying the initial domain and its growth after three pulses. Additionally, the center of mass and the ROI are displayed in blue. Every white pixel within the blue area contributes to the growth to the right and the left depending on whether it is on the right or left side of the center of mass.

of the domains considered here cannot simply be determined along one line parallel to the field axis as usually practiced in the asymmetric bubble expansion method. This is due to the dendrimeric domains exhibiting a statistically distributed non-uniform growth, via the spreading of their branch-like domain parts. The growth determination along a single pixel line parallel to the field axis can lead to large statistical deviations and non-representative growth velocities. Instead, the growth is determined by averaging the growth of several lines parallel to the axis in the form of an area displaying the region of interest (ROI) for the growth. All white pixels z_{ij} in the pixel lines in the range of $\pm y_{\text{width}}$ around the center of mass contribute to the growth calculation. This region is marked in blue in Fig. 19b. Based on this ROI average growth per pixel line along the field axis as well as its standard deviation is calculated. Hereby, all pixels in the ROI left from the center contribute to the growth to the left and all pixels on the right of the center contribute to the growth to the right,

respectively

$$v = \frac{1}{I_{\max} \cdot 2y_{\text{width}} \cdot t_{\text{pulse}}} \begin{cases} \sum_{i<X,\, Y-y_{\text{width}} \leq j \leq Y+y_{\text{width}}} I_{ij} & \text{left side growth} \\ \sum_{i>X,\, Y-y_{\text{width}} \geq j \geq Y+y_{\text{width}}} I_{ij} & \text{right side growth}\,, \end{cases} \tag{80}$$

with X and Y being the coordinates of the center of mass. The following Figs. 19 and 20 display the calculated center of mass as well as the growth to the right for an ROI of $y_{\text{width}} = 200\,\text{px}$. To simplify the form of representation, all of the following figures focus more intensely on the growth to the left. However, all arguments which will be made to the left side growth also apply to the right side growth. Figure 20 presents that there are strong fluctuations in the growth along different pixel lines. This example particularly shows that a significantly lower growth velocity would have been determined if only the line along the center of mass would have been included. Nevertheless, this statistical determination of

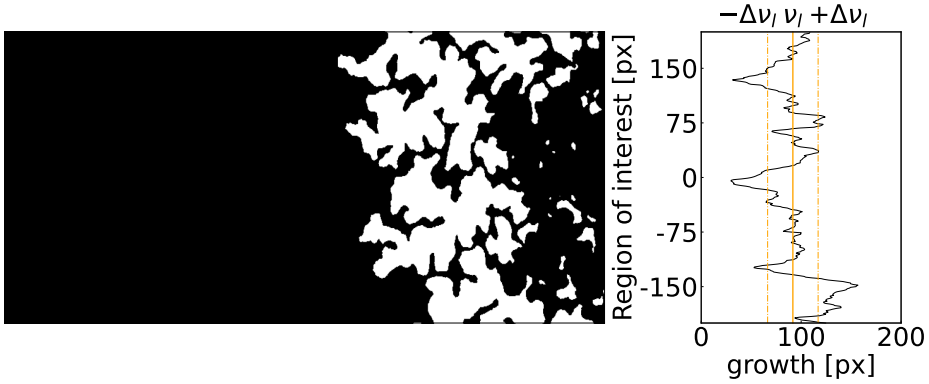

Figure 20: Visualization of the growth determination in the region of interest on the left of Fig. 19b. The right part of this figure is a 90° tilted line histogram. In this, the sum of white-colored pixels (x-axis) is determined for each line (y-axis). Based on this, the mean velocity v and its standard deviation Δv of the growth are then determined. For this purpose, the growth is also divided by the pulse duration of $t_{\text{pulse}} = 1\,\text{s}$.

the growth deviates from the typical asymmetric bubble expansion method [9]. Therefore, the extent of the impact of the ROI on the asymmetric bubble expansion method is briefly checked below in Fig. 21. In this figure, the field-dependent velocity to the right is displayed for several different sizes of the ROI, governed by the parameter y_{width} which is half the ROI. In addition, each of the curves in this figure is fitted by applying the basic creep law, which is discussed in more detail in section 4.4. For the y_{width} shown in Fig. 21, the value of 10 px was chosen as the absolute minimum to guarantee an evaluation based on statistics. There is hardly any difference between the different ROIs and the DMI field strength H_{DMI} taken from

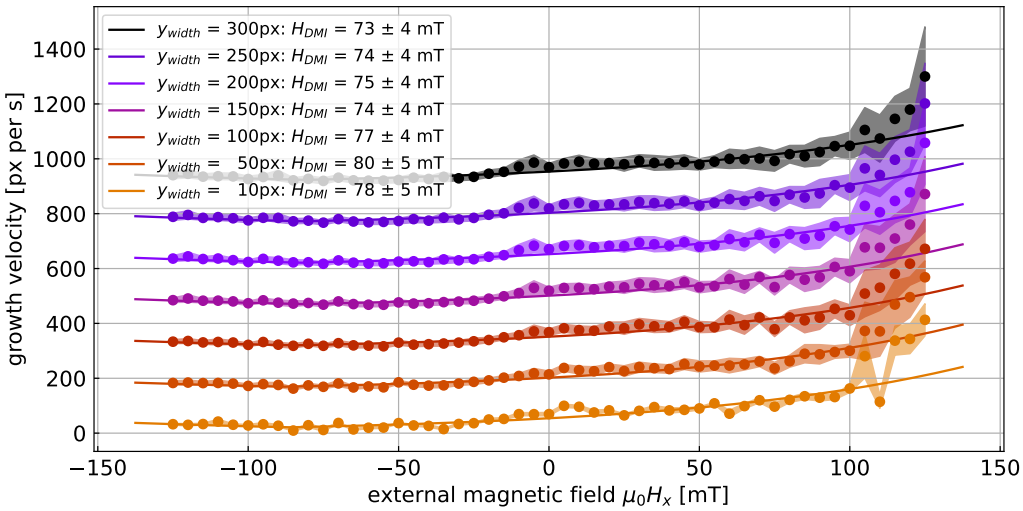

Figure 21: Field-dependent growth velocity to the left for a positively pre-saturated sample. Each color represents another size of the region of interest given by 2 times the y_{width} values in the legend. Besides the smallest ROI, its size seems to have minor effects on the fit and the DMI field strength H_{DMI} extracted from it. The fit is based on the basic creep law in Eq. (74), whereby its mathematically more convenient form in Eq. (81) has been applied.

the fit is also consistent within the specified uncertainties. There is only a slightly noticeable difference for the smallest FOV in which the data points fluctuate a bit more stronger. Based on this figure, the statistical evaluation seems to only possess minor impacts on the fit while it is well able to compensate for the statistical behavior of the dendrimeric domains. Thus, if not stated otherwise, y_{width} has been set to a value of 200 px, which matches the visualized region of interest in Fig. 19b.

4.3.4 FOV and Growth Stability

The evaluation of the domain growth velocity is limited to the area imaged by the KERR microscope camera, i.e., the FOV. The growth outside of this FOV is unknown and thus quantitative statements about the domain growth are limited once the domains have reached the edge of the FOV.

In particular, this limits velocity determination at high in-plane fields above 100 mT, where growth outside the FOV is achieved quite easily due to the exponential impact on the velocity (see ARRHENIUS creep law in Eq. (74)). Measurements in these field ranges are particularly important for the determination of the DMI because at these fields the growth velocity in the unfavored direction increases again. Without this increase, the minimum of the fit function representing the H_{DMI} field cannot be assigned. The fit might result in unreasonably small or large H_{DMI} values.

The aforementioned automatic evaluation of the images is therefore extended by a function checking whether the domain leaves the FOV or whether it is completely contained in it. Domain growths with supposedly significant growth rates outside of the FOV are discarded by the program. Nevertheless, these cases can only be estimated, since the detection is still limited to the information contained in the FOV. There are no pieces of information from outside of the image available. The criterion approximating a significant growth outside of the FOV is therefore chosen so that domains touching the outermost region of the image also grow beyond the FOV. Mathematically speaking, the criterion determines whether the outermost 20 columns of pixels are occupied by the growing domain by at least 25% in the binarized images.

The relatively high threshold of 25% is intended to desensitize this criterion to defects that are partly recognized as growing domains in the binarized images. In addition, a lower threshold might also discard images where the growth is almost completely contained within the FOV. Thus, the high threshold should also prevent excessive data loss. Once this FOV-threshold is reached, the growth of all subsequent pulses in the respective direction is also neglected. Figure 22 schematically displays the calculation of the FOV threshold with an example in which it is not desired to discard Fig. 22b since its growth is still mainly contained in the image. This method of recognizing probable growth outside of the FOV requires that the image of the nucleated domain is subtracted from all growth images instead of consecutive images being subtracted from each other. Hereby, the velocity is determined by extending the time t_{pulse} in Eq. (80) by the number of growth pulses n that have been applied.

The functionality of the automatized detection of growth outside the FOV was verified on several series of measurements by manually determining the pulses which are expected to possess significant growth outside of the image. The threshold of 25% is chosen so that the manual and automatic determination of the growth outside the FOV matched in all tested image series. The velocities shown in Fig. 21 and also all subsequent velocities have been

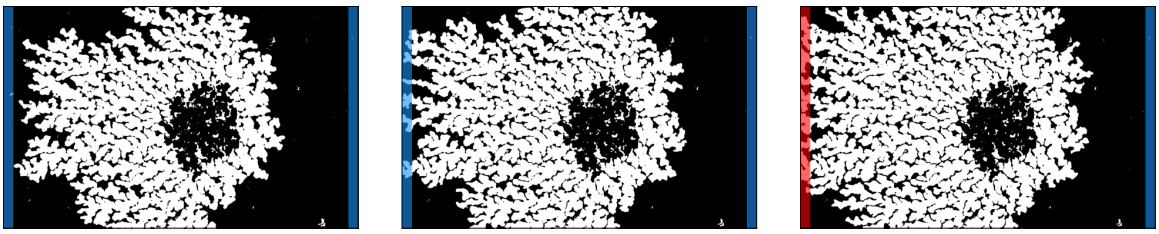

(a) No growth at the border of the FOV.

(b) Negligible growth at the border of the FOV.

(c) Large growth at the border of the FOV.

Figure 22: Example for the determination of whether the growing domain is contained in the FOV or not. The area for calculation of the condition is colored in blue when the domain is expected to be (mainly) inside the FOV and red when it significantly grows outside of the FOV. Solely for enhanced visualization, the FOV has been enlarged to 100 px. This test requires subtraction of the initially nucleated domain image instead of the previous domain image.

determined as averages over all growth pulses whose corresponding growth is located within the FOV. This raises the question of whether the size of the domains has a significant influence on the growth behavior of the domains since this would lead to an additional dependence of the growth on the initial nucleation size, the number of growth pulses as well as the growth velocity itself. In principle, for example, the model of the dispersive stiffness in Tab. 2 possesses an energy contribution of the domain wall curvature, which in principle is affected by the domain size of bubble domains. This is expected to be not true or at least weaker for the dendrimeric domains observed here since the domain walls in this form are already strongly curved by the branch-like structure and no visible change in curvature with a growing domain could be observed.

Therefore, based on the example in Fig. 23 it is checked whether the growth rate changes with the number of pulses and thus with the size of the domain or not. In this figure, the same series of measurements as in Fig. 22 is displayed. In the growth to the right (blue) an almost constant velocity is visible, while in the left-side growth two different regions are visible. The velocity is also almost constant in the first region, while it decreases in the

second region. Analyzing these velocities with the previously introduced method shows that starting from the 6th pulse (Fig. 22c) there is significant growth outside of the FOV, which explains this decrease in the measured velocity.

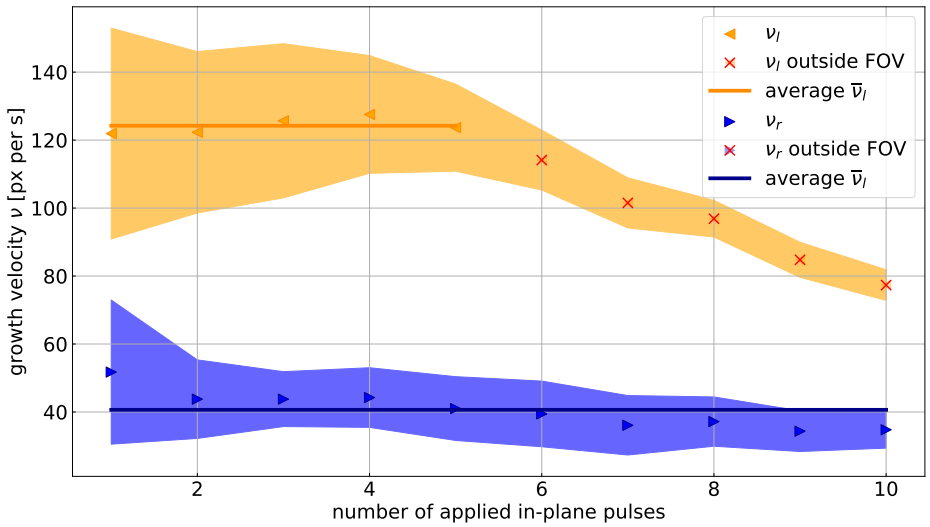

Figure 23: Asymmetric growth velocity of a domain with an in-plane field strength of $\mu_0 H_\mathrm{x} = -20\,\mathrm{mT}$ and a negative pre-saturation. The growth to the right is displayed in blue and possesses a constant velocity with an increasing number of growth pulses or equally increasing domain size. Contrary, the left-side growth velocity is constant to the fifth pulse where an almost linear decrease in velocity is visible. This decrease is associated with an undetectable domain growth outside of the FOV.

Based on Fig. 23, the domain growth is likely constant with the domain size. Therefore, averaging the velocity of all growth pulses is feasible.

4.4 Intrinsic DMI Field

According to the last section 4.3, the determination of the domain growth velocity can be summarized to:

1. Subtraction, contrast enhancement, and binarization of the recorded MOKE images according to Figs. 16 to 18

2. The growth velocity is then pulse-specifically determined to the left and right of the center of the nucleation domain in an ROI according to Fig. 20

3. The determined growth velocities are averaged over all contributing pulses, whereby direction-specifically contributions with significant growth outside of the FOV are neglected, according to Fig. 23.

With this evaluation process, the field-dependent asymmetric expansion velocities in Fig. 24 for negative (Fig. 24a) and positive saturation (Fig. 24b) are extracted from the measurements described in section 3.2.4. The measured field-dependent domain growth velocities are

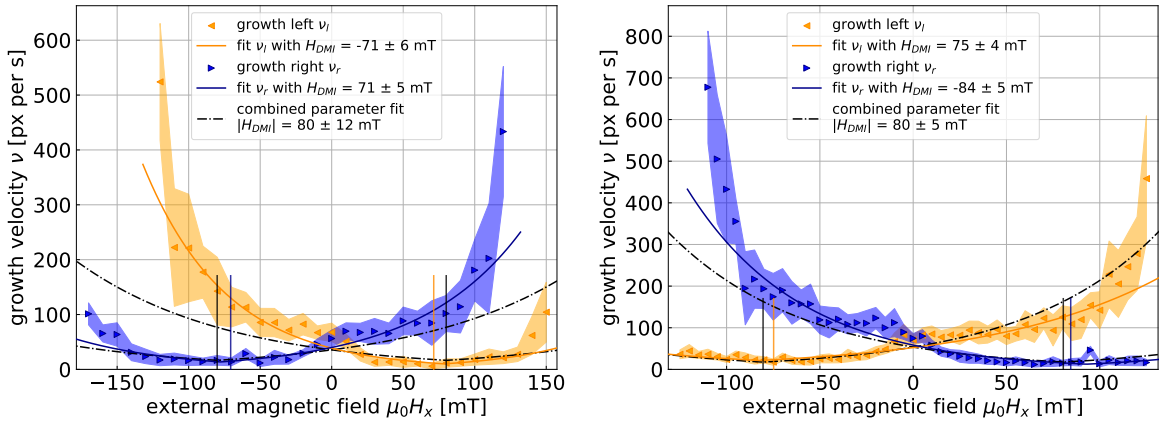

(a) Asymmetric growth in dependence on the in-plane field $\vec{H}_x$ for negative saturation (antiparallel to the surface normal).

(b) Asymmetric growth in dependence on the in-plane field $\vec{H}_x$ for positive saturation (parallel to the surface normal).

Figure 24: Asymmetric growth velocity of the non-bombarded sample in dependence on the in-plane field $\vec{H}_x$ for positive (parallel to surface normal, 24a) and negative saturation (antiparallel to surface normal, 24b). The growth to the right is presented in blue while the growth to the left is presented in yellow.

direction-dependently fitted to the basic creep model in Eq. (74), whereby the basic creep

model has been simplified to

$$v(H_\mathrm{x}) = v_0 \cdot \exp\left(\alpha_0 \cdot \left[\frac{B \cdot |\mu_0 H_\mathrm{z} + \mu_0 H_\mathrm{DMI}| + C}{B \cdot |\mu_0 H_\mathrm{DMI}| + C}\right]^{0.25} \cdot H_\mathrm{z}^{-0.25}\right) . \tag{81}$$

Hereby, the parameter B equals $-\pi M_\mathrm{S}\lambda$ and C equals $\sigma_0 + 2K_\mathrm{D}\lambda$ as shown in Eq. (75). However, since this method is only intended to determine the intrinsic DMI field H_DMI, these parameters, as well as v_0 and α_0, are not discussed with their physical meaning. They are here only considered as fitting parameters allowing the calculation of the DMI field, although the fitting parameter B might give insight into the domain wall width λ.

In the asymmetric bubble expansion method, a measurement of the domain wall velocity as a function of the external oop field H_z and without an in-plane field is sometimes performed to determine the parameters v_0 and α_0. These can then be applied as initial parameters for the fit of the actual measurement series [9].

Since all fit parameters depend on the nature of the sample, they should be identical for both growth velocities to the left and the right. Thus, a third fit is performed in which the fit parameters are constrained to be identical for both directions. This third fit is referred to as a combined parameter fit. The DMI field is determined as the mean of all three fits. For the sample shown in Fig. 24, the DMI field amounts to

$$\mu_0 H_\mathrm{DMI} = 78 \pm 19\,\mathrm{mT}\,. \tag{82}$$

In combination with the experimental saturation magnetization $M_\mathrm{S} = 591 \pm 55\,\mathrm{kA\,m^{-1}}$, the effective crystalline anisotropy $K_\mathrm{eff} = 2 \cdot 10^5\,\mathrm{J\,m^{-3}}$ as well as the literature value for the exchange stiffness $A_\mathrm{ex} = 1.6 \cdot 10^{-11}\,\mathrm{J\,m^{-1}}$ the scalar DMI amount to

$$D = +0.41 \pm 0.14\,\mathrm{mJ\,m^{-2}} \tag{83}$$

in accordance to Eq. (70). This value is in the same order of magnitude but slightly above other DMI values that were determined based on the asymmetric bubble expansion method [9]. The positive sign of the DMI is derived from the mutual arrangement of domain magnetization, ip field direction and the direction of the dominant domain expansion as described in section 3.2.3. With this value, it is verified that the quantification of the DMI with the dendrimeric domains is possible, even if both the measurement and the evaluation method can still be optimized in many respects.

5 Modification of the Interfacial DMI via IB

Besides the quantification of the DMI, this work also focuses on the modification of the DMI. A critical parameter for the DMI, which can be influenced after the fabrication procedure, is the interface roughness between the heavy metal and the ferromagnetic layer [9]. This can be achieved by ion bombardment (IB) with light ions such as He^+, whereby the modification might be attributed to interfacial intermixing [8]. Other working groups have already modified the DMI in other sample systems by He^+ ion bombardment, whereby an increase of the DMI could be achieved with lower doses and a decrease of the DMI again with higher doses [8]. These low and high ion dose ranges differ from sample to sample. For example, in [8], the samples have been bombarded with doses up to $4 \cdot 10^{16}\,\mathrm{cm}^{-2}$ with an increase of the DMI in the region up to $2 \cdot 10^{16}\,\mathrm{cm}^{-2}$ and in [11], and [33] the samples have been bombarded up to $1.6 \cdot 10^{14}\,\mathrm{cm}^{-2}$, and $3 \cdot 10^{15}\,\mathrm{cm}^{-2}$ respectively. In the last case, the general dependence of the domain wall velocity was investigated and not the DMI explicitly.
In a previous bachelor thesis [26] it has been shown that the resolution of the MOKE microscopic investigation is limited to ion doses up to $D_{\mathrm{IB}} = 2.5 \cdot 10^{14}\,\mathrm{cm}^{-2}$. The reason is discussed in more detail in section 7.2. For this reason, the ion bombardment experimental series is limited to $D_{\mathrm{IB}} \leq 2.5 \cdot 10^{14}\,\mathrm{cm}^{-2}$. The minimum dose in normal incidence is experimentally limited to about $D_{\mathrm{IB}} = 1 \cdot 10^{13}\,\mathrm{cm}^{-2}$. In principle, lower ion doses could be achieved with a bombardment in tilted incidence. Due to limited sample material, the tilted ion bombardment is discussed theoretically and not conducted experimentally.

5.1 Ion Bombardment of Solid Materials

Within the scope of this work, the magnetic multilayer thin-film system was bombarded with accelerated He^+ ions with a kinetic energy of 10 keV to alter the magnetic properties, in particular, aiming to modify the interfacial DMI freely. This means, that optimally the ion bombardment enables an increase as well as a decrease of the DMI. To understand the effects of the 10 keV He^+ ion bombardment on the samples, the occurring interactions between energetic ions and target materials are discussed in the following. A special focus is given to the elaborations of J. Ziegler et al, who have combined them in a collection of software programs called *Stopping and Range of Ions in Matter (SRIM)*, enabling a simulation-based theoretical description of the IB. This section's content provides a brief summary, essentially based on their book *SRIM - Stopping and Range of Ions in Matter*, which offers a deeper

insight into this topic [34].

An accelerated ion with kinetic energy starts to dissipate this energy into its environment upon entering matter. This energy transfer proceeds by electronic and nuclear interaction, which decisively depends on the material system as well as on the ion mass and kinetic energy. The transferred energy, i.e., the energy loss $-\mathrm{d}E$ of the ion per unit length $\mathrm{d}x$, called stopping power $S(E)$, and can be described as a function of the kinetic energy E for a specific combination of a material and an ion

$$S(E) = -\frac{\mathrm{d}E}{\mathrm{d}x} = S_\mathrm{n}(E) + S_\mathrm{e}(E) \quad [34] \ . \tag{84}$$

The stopping power in Eq. (84) is separated into the nuclear $S_\mathrm{n}(E)$ and electronic $S_\mathrm{e}(E)$ stopping powers, based on their different underlying mechanism. For low energies, the nuclear stopping power is dominant, as depicted in the double-logarithmic Fig. 25 of energetic helium ions in the alloy $Co_{70}Fe_{30}$, while for higher energies the electronic stopping power predominates.

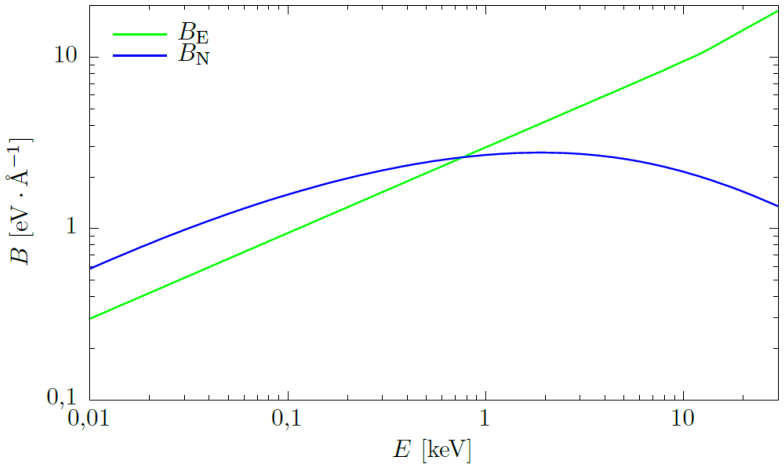

Figure 25: Stopping power for He^+ ions in the alloy $Co_{70}Fe_{30}$ in the region of 0.01 to 30 keV. Taken from [35].

Nuclear Stopping Power

The nuclear stopping power is based on energy transfer during elastic collisions with the target nuclei. For low energies, these collisions excite phonons, while for larger energies, the target atoms can additionally be knocked out of the crystal lattice. This nuclear interaction is describable by the Coulomb interaction of the ion and target nuclei with additional shielding factors considering inner-shell electrons. Thus, each pair of ion and target elements possesses

its interaction potential which J. Ziegler et al approximated with an empirical universal potential [34]. Based on this approximation, the following universal nuclear stopping power is determined by

$$S_{\mathrm{n}}(\varepsilon) = \begin{cases} \frac{\log(1+1.1383\varepsilon)}{2\cdot(\varepsilon+0.01321\varepsilon^{0.21226}+0.19593\varepsilon^{0.5})}, & \text{for } \varepsilon \leq 30\,, \\ \frac{\log(\varepsilon)}{2\cdot\varepsilon}, & \text{for } \varepsilon > 30\,. \end{cases} \tag{85}$$

All material parameters are contained in the transformation from the ion's kinetic energy E to the expression in terms of its reduced energy ε. This transformation was introduced by Jens Lindhard and is also depicted in the book by J. Ziegler et al [34]. For very high reduced energies of $\varepsilon > 30$, the first solution is insufficient of explaining Rutherford scattering phenomena and is therefore substituted for the non-shielded case in the second part of the solution [34].

Electronic Stopping Power

The electric field of the energetic ion is interacting with the free and bound electrons in matter resulting in electrical polarization of the target. The locally polarized target material influences the effective charge of the ion. This interaction transfers energy from the moving ion to the electronic system of the target material and is thus called electronic stopping power. According to Lindhard et al, the electronic stopping power can be approximated by assuming a varying local charge density caused by the ion S_{e} with

$$S_{\mathrm{e}}(\rho,\, v(E)) = \int I(\rho,\, v(E)) Z(v(E))^2 \rho dx^3 \quad [34]\ . \tag{86}$$

In this approximation, the small perturbations of the local charge density ρ are introduced by separating the total volume into many independent elements of volume dx^3 which is calculated by solving the integral in Eq. (86). The total electronic stopping power is obtained by averaging over all integrals weighted by their distribution in the solid. Hereby, the interaction strength $I(\rho,\, v(E))$ and the effective charge of the ion $Z(v(E))^2$ are assigned in dependence on the ions velocity v and thus to the kinetic energy E.

The energy transfer for higher kinetic energies increases exponentially, since increasingly more (inner-shell) electronic states can be excited. If there is sufficient energy transfer, this mechanism is also able to ionize target atoms. However, due to the metallic character of all material systems considered in this thesis, it is assumed that these ions quickly recombine with free electrons and do not remain in the system.

The transition energy between the dominant stopping effect for helium ions depends on the

target system. A more detailed consideration of the stopping powers and a comparison with experimental values can be found in the book by J. Ziegler [34].

Based on the elaborated effects, the core software package *Transport of ions in matter (TRIM)* of SRIM is suitable for simulating the ion bombardment as well as its impacts and consequences on the simulated material system. It combines a MONTE CARLO simulation approach with more than 28000 material parameters, extracted from a large range of experimental research papers.

The target material system is generated as a multilayer system based on the input, whereby the material composition, layer thickness, and state of matter (solid or gaseous) are chosen for each layer individually. The layers themselves are simulated with an isotropic atomic distribution and thus represent amorphous or polycrystalline crystals in the case of solid matter. Besides these inputs, the most important parameters are mass density and binding energies. The mass density directly affects the isotropic distribution of atoms inside of the target material, determining its densities of charges and nuclei. The binding energies are separated into displacement and surface binding energies as well as lattice binding energy and govern what happens with the target material after the energy transfer. The first two energies are basically energy barriers which describe the minimum energy for an atom to leave its lattice site within the target or on its surface respectively. The last parameter describes the energy loss of such a liberated target atom during its escape from the site.

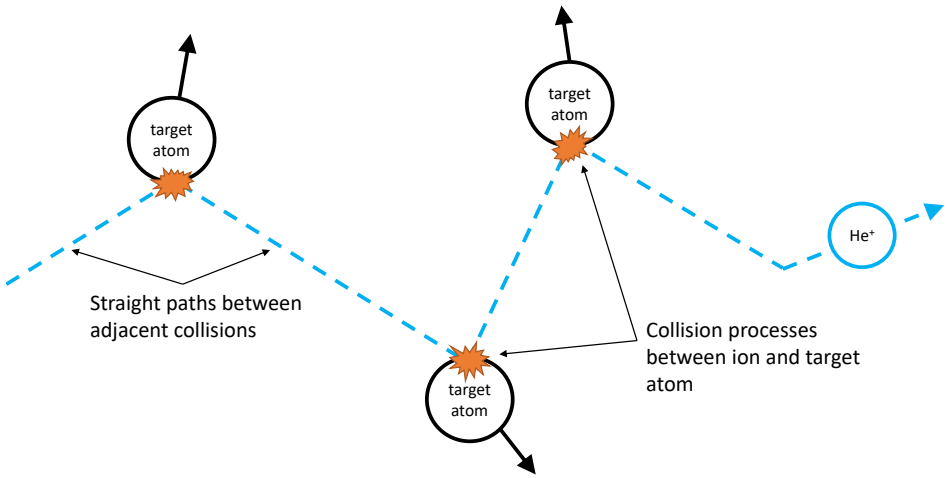

Figure 26: Schematic illustration of independent binary collisions of target atoms with light He ions. The independent collision phenomena are separated by straight paths.

For elemental layers, all of these values are adapted from literature, whereby alloys are interpolated depending on their relative atomic composition. For materials including low atomic

masses, e.g., organic compounds, the bonding situation is also of particular importance, which can be taken into account by a compound correction factor.
The input values for the incident ion beam are the element, kinetic energy, and angle of incidence, with 0° as perpendicular to the target surface. The ion mass is determined as the most abundant natural isotope of the chosen element, instead of the weighted average usually displayed in the periodic table of elements. The mass is alterable to also work for certain isotopes if desired.
For a given ion beam and target material system, *TRIM* can simulate the

- energy input, recoils, defects, and vacancies in the target material,
- ionization phenomena and implantation of ions in the target system,
- reflection and transmission of incident ions,
- and sputter yield of the target material

among other quantities. Besides reflection and transmission of the incident ions, these quantities are also simulated target depth specifically.
As typical for all Monte Carlo Simulations, *TRIM* sequentially calculates individual incident ions one after another. Hereby, the individual ion interactions and transports are not representative of the interaction with the target system. Instead, a sufficiently large amount of incident ions is simulated, enabling feasible statistical evaluations which then are representative of the ion matter interaction.
The Monte Carlo simulation method included in *TRIM* is based on a binary collision approximation. Hereby, the behavior of the energetic ion is approximated by a sequence of independent binary collisions with target atoms and straight paths in between two subsequent collisions as shown in Fig. 26. This enables a separate, independent description of the two stopping powers in Eq. (84). The nuclear stopping power only occurs within the collision phenomena while the electronic stopping power mainly decelerates the ion during its straight paths. By solving the scattering integral of the collision time-dependently, the electronic power can also be applied during the time interval of each collision. The collision and impact parameters of each integral are randomly chosen from a probability distribution depending on the material and its atomic density.
The energy input of the incident ions will finally be converted to heat, independent of the occurring processes. The energy losses only happen during reflection and transmission on

incident ions as well as target atoms emerging from the surface (sputtering). This leads to two final effects after the ion bombardment:

1. Local hyperthermic heating of the sample layer system. The energy input of 10 keV He ions transferred locally into the layered system exceeds the room temperature of about 25 meV by several orders of magnitude. This energy input is, for example, able to free states from local minima, converting them into global minima [36, 35]

2. The atoms released from the lattice intermixing in the layer system. While larger scales of this intermixing usually possess a destructive impact, weak intermixing can be interesting, especially at interfaces. Because interfacial effects are usually altered along with their interface, weak intermixing might directly address these [36, 35].

The impact of both final effects on the layer system of interest here will be investigated and discussed in more detail with suitable simulations in section 5.4.

5.2 Ion Bombardment Facility

The ion bombardment facility (ISA - dt. **I**onen**S**trahl**A**nlage) is a setup for a controlled bombardment of He^+ ions with energies of about 10 keV with a $2 \times 2\,mm^2$ square-shaped beam profile [36]. It consists of a PENNING ion source, several electrostatic lenses for focussing and acceleration, an aperture, and a motorized table with a sample holder, which can move in the xy-plane and controls which area is bombarded. All of these components are contained in a vacuum chamber as shown in Fig. 27. In this, the ion bombardment is conducted at a working pressure of at least $p_{IB} \leq 2 \cdot 10^{-5}$ mbar. Additionally, a FARADAY cup and a mirror can be inserted into the beam path. The mirror blocks the ion beam and replaces it with a light beam approximately visualizing the beam path for *in situ* control during the experiment. The FARADAY cup detects the beam current, i.e. how many ions are bombarded onto the sample per second, determining the ion dose of the current square-shaped beam profile. The square-shaped profile is formed by the aperture and exemplarily depicted in Fig. 28. With a beam blanker, the beam can be blocked during the experiment which, in principle, is also achieved by moving the mirror or the FARADAY cup into the beam path.
The ions are irradiated onto the sample surface, where they interact with the sample as described in section 5.1. The sample holder itself is grounded to avoid charging effects, like deflection after a certain bombardment time. Larger areas can be bombarded by moving the sample during the bombardment. This generates many individual bombardment points

with the ion beam profile given in Fig. 28, which together cover the desired area or line. For the normal incidence displayed in Fig. 27, ion doses in the range of $1 \cdot 10^{13}\,\mathrm{cm}^{-2}$ to

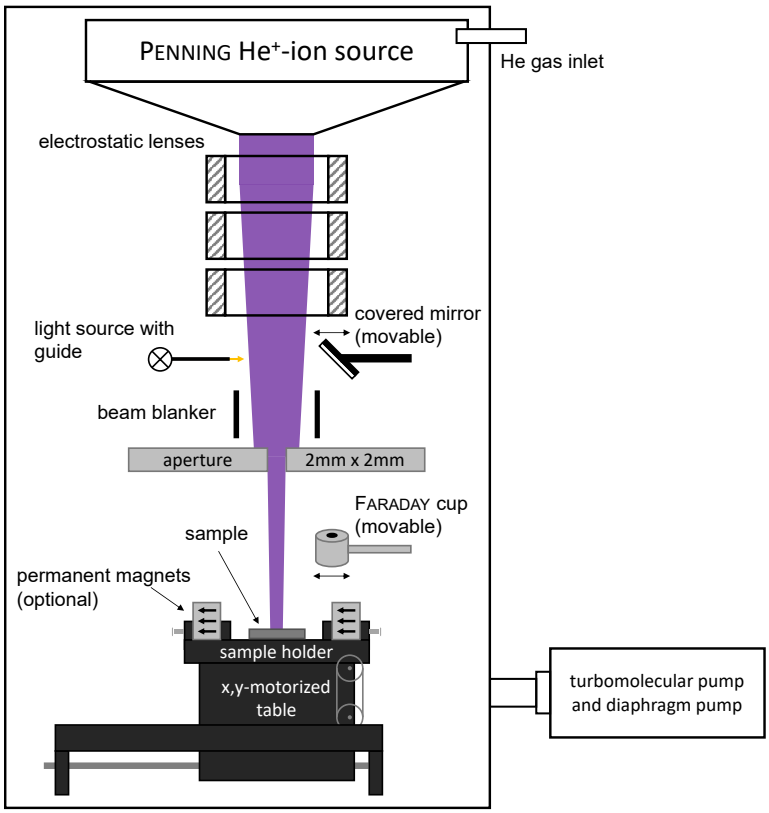

Figure 27: Schematic illustration of the ion bombardment facility (ISA - dt. **I**onen**S**trahl**A**nlage). The entire facility is located in a modular, tower-like vacuum chamber, which achieves working pressures of less than $p_{\mathrm{IB}} \leq 2 \cdot 10^{-5}\,\mathrm{mbar}$ with a serial connected turbomolecular and diaphragm pump. The ions are generated in a PENNING ion source and accelerated and focused by the electrostatic lenses.

$1 \cdot 10^{17}\,\mathrm{cm}^{-2}$ are possible. Larger ion doses are possible as well but they are associated with large bombardment times. However, a previous bachelor thesis [26] demonstrated that even lower ion doses than $D_{\mathrm{IB}} = 1 \cdot 10^{13}\,\mathrm{cm}^{-2}$ are desirable, which has also been observed in the dose-dependent evaluation in section 6. Since $D_{\mathrm{IB}} = 1 \cdot 10^{13}\,\mathrm{cm}^{-2}$ is roughly the minimum ion dose in normal incidence, lower ion doses are only possible by performing the ion bombardment in a tilted sample configuration. Tilting the sample around the angle γ along the y-axis should increase the bombarded initial $2 \times 2\,\mathrm{mm}^2$ area by a factor of $\frac{1}{\cos\gamma}$. Therefore, a rotation angle of, for example, $\gamma = 60°$ results in an area enlarged by a factor of 2. This exact example of a rotation angle is displayed in Fig. 28, in which the initial, experimentally determined ion beam profile (positive x and y coordinates) is projected onto

a plane rotated by 60° around the y-axis (negative x and y coordinates). A new ion beam profile is interpolated based on these projected points, whereby the total charge, given by the 2D integral, has to be conserved. Since the irradiated area is enlarged by a factor of 2, the ion dose is correspondingly reduced by the same factor. This is displayed by the contours in the xz- and xz-plane. Therefore, tilting the sample around an angle could lead to enabling

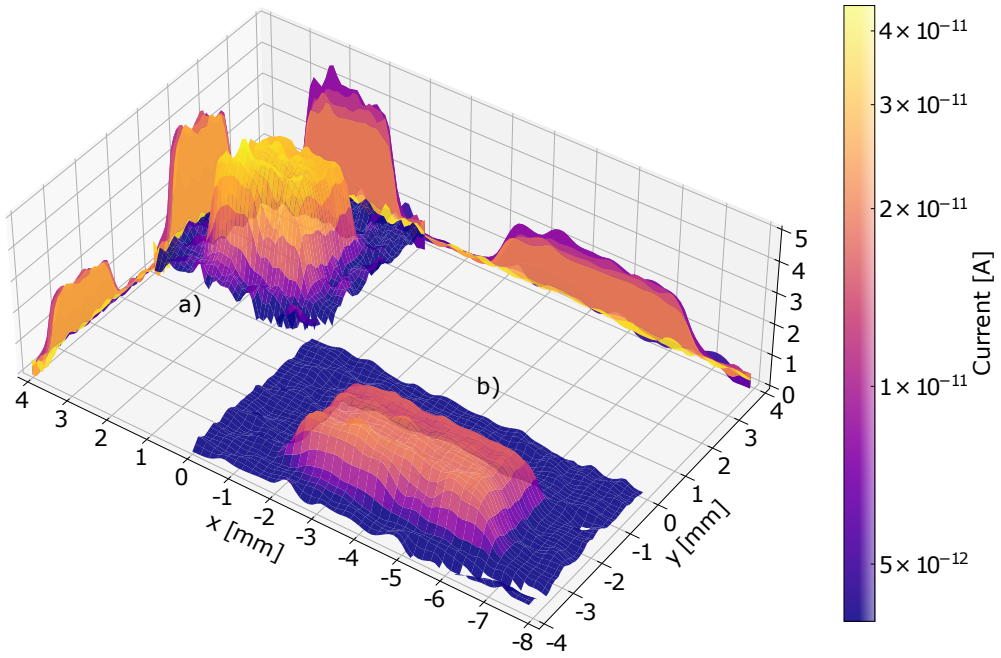

Figure 28: 3D view of the beam profile in normal incidence (positive x- and y-values, a)) and 60° tilted incidence (negative x- and y-values, b)) with a roughly 1.5 V reduced focus voltage of 7 V to achieve a smaller ion doses. Additionally, the yz- and xz-planes display the contour, i.e., the shape of the beam profiles. This ion profile of the tilted incidence is approximated by projecting the normal incidence onto a plane rotated by 60° with subsequent interpolation with the condition of total charge conservation. With the 60° tilt along the y-axis, the bombarded area is about twice as large as in the normal-incidence case, and therefore, the ion dose may be reduced by roughly a factor of 2.

ion doses below $1 \cdot 10^{13}\,\mathrm{cm}^{-2}$. The tilting is enabled in a $-30° \leq \gamma \leq 30°$ range by an in-built rotation mechanism in the motorized table. Larger angles might be possible by an underlying piece of copper with a canted surface with a slope of, for example, 45°. However, it has to be taken into account, that changes in the angle of incidence also alter the interaction of the ion beam with the sample. This is discussed in more detail in section 5.4.

5.3 Ion Bombardment Procedure

For altering the samples with the ion bombardment two separate bombardment procedures have been persecuted. The first one involves three small pieces of samples in which areas are completely bombarded with one homogeneous ion dose of $7.5 \cdot 10^{13}\,\mathrm{cm}^{-2}$, $1 \cdot 10^{14}\,\mathrm{cm}^{-2}$, or $1 \cdot 10^{15}\,\mathrm{cm}^{-2}$. These samples are intended for the investigation of the ion-dose-dependent saturation magnetization and anisotropy in the VSM experiments. The second ion bombardment procedure involves the samples investigated by the MOKE microscope and its bombardment process as schematically depicted in Fig. 29. In this, a large piece of sample is covered with adhesive stripes at repetitive distances leaving roughly 1 mm stripes of the sample surface uncovered. Each of these stripes is bombarded by a specific ion dose as shown in Fig. 29. Additionally a large area is kept non-bombarded being used as a reference.

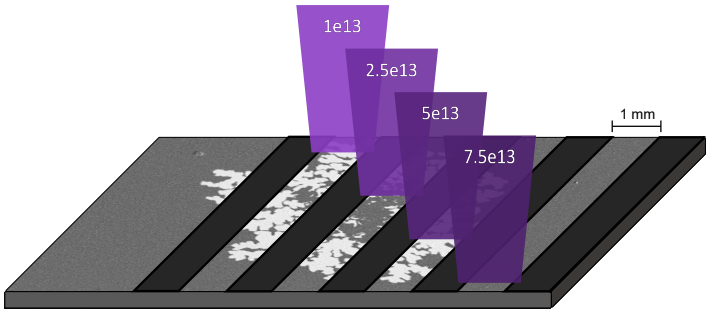

Figure 29: Schematic sketch of the ion bombardments on the sample material with different ion doses between $1 \cdot 10^{13}$ and $7.5 \cdot 10^{13}\,\mathrm{cm}^{-2}$. The bombarded stripes are roughly 1 mm wide preventing gradients in ion dose related to borders of the ion beam profile.

This approach arises from strictly avoiding ion beam gradients, which are for example caused by the edges of the ion beam profile. The closely covered adhesive stripes are intended to cut off the edges to the left and the right of an ion beam traveling along the stripe. The cut ion beam profile is approximately $1 \times 2\,\mathrm{mm}^2$ wide. The resulting homogeneous ion bombardment is critical since earlier attempts in the scope of the bachelor thesis [26] demonstrated that gradients strongly affect domain wall movement. This is related to ion gradients which cause additional changes in the asymmetric domain wall movement since the point of magnetic reversal is strongly dependent on the ion dose as shown in Fig. 54. This has also been observed in the bachelor thesis prior to this work [26]. While this gradient-associated property might be promising to achieve, for example, remagnetization via directed domain wall movement, it is also interfering with the asymmetric bubble expansion method in section 3.2.3. To obtain purely in-field dependent domain wall growth and no ion-gradient

associated domain wall growth, these gradients should be avoided as far as possible.
With the ion bombardment performed as shown in Fig. 29, five spatially separated regions with different ion doses are created. Initially, it has been intended to extend the depicted ion range by higher as well as lower ion doses but this was not conducted due to the limited sample material. In total, a sample area of roughly $2 \times 1\,\mathrm{cm}^2$ has been used for the bombardment experiments.

5.4 Stopping and Range of Ions in Matter - SRIM

The SRIM simulations were performed to clarify the impact of the He^+ ion bombardment, accelerated to the kinetic energy of 10 keV, on the multilayer system presented in Fig. 3. In section 4.1 it was discussed that the magnetic layer system is most likely slightly thinner than in the nominally specified system in Fig. 3, although it is unclear which layer deviates to what degree. Since the deviations are small, the idealized nominal layer system in Fig. 3 is assumed and designed as input for the SRIM simulations. Two particular points should be highlighted:

1. An underlying 1 µm thick Si substrate layer has been added to all simulations. However, for better visibility of the much thinner layers, the Si layer will not be displayed in the subsequent figures. The substrate layer is of particular interest regarding the backscattered or reflected ions moving back into the multilayer system.

2. The system consists of several monolayers, which have been taken into account in the simulation program. Hereby an adapted simulation mechanism is applied which alters the probability distribution discussed at the end of section 5.1. Instead of an isotropic probability distribution, the system is considered to consist of several individual, independent atomic monolayers. The incoming ions are imposed by the constraint of one interaction with each monolayer. This is a necessary approximation for the interaction with very thin layers [34]

Besides these additional points, the literature-related default parameters of SRIM for elementary material systems are integrated into the simulation. In total 99999 helium ions have been simulated iteratively, based on the Monte Carlo simulation approach. The average effect of the ions can be determined by averaging this number of ions statistically, which is exemplarily displayed in Fig. 30 for the energy input and the generation of vacancies per 10 keV He^+ in normal incidence. The two properties shown in Fig. 30 are associated with

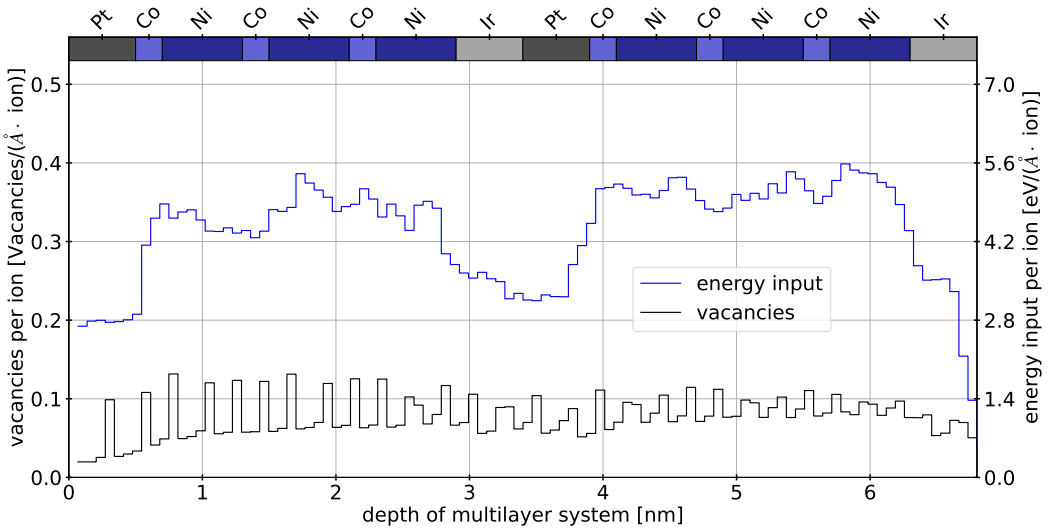

Figure 30: Simulated average energy input in eV (blue) and generated vacancies (black) per 10 keV He^+ ion in normal incidence in the layer system. The peaks of the generated vacancies correspond to the positions of the monolayers. SRIM automatically creates depth distances in which the properties are simulated. These do not necessarily have to match the monolayers or the nominal layer system (on top), in which case the properties of the corresponding depth are then interpolated by the relative proportions of the monolayers above and below.

the energy input and intermixing caused by the ions. The energy between 2 to 5 eV per Å and ion is introduced into the layers, which lies about two orders of magnitude above the thermal energy at room temperature (300 K of $\approx$ 25 meV). The energy input mainly takes place in the ferromagnetic material.

In addition to the energy input, the intermixing of the materials may also have an impact on the DMI. A first indication is shown in Fig. 30 plotting the number of caused vacancies per ion. However, to quantify the degree of intermixing, the released target atoms and ions have been investigated in addition to the vacancies. For simplification, the cobalt and nickel layers are summarized as the ferromagnetic layer and the iridium and platinum layers as the heavy metal layer. The intermixing is determined by the atoms and ions that leave their initial material layer. In the simplified view of solely ferromagnetic and heavy metal layers, this corresponds to the atoms transferred between these two layers. Atoms that remain in their initial material layers have been neglected, even if they may have an influence, e.g. as defects and imperfections. In addition, it was assumed that the light helium ions do not sputter atoms from the material system, which particularly affects the first layers. This assumption is intended to simplify the calculation of the intermixing.

Under these assumptions, the intermixing in Fig. 31 has been calculated in dependence on the bombarded ion dose in normal incidence. The small amount of intermixing for ion doses

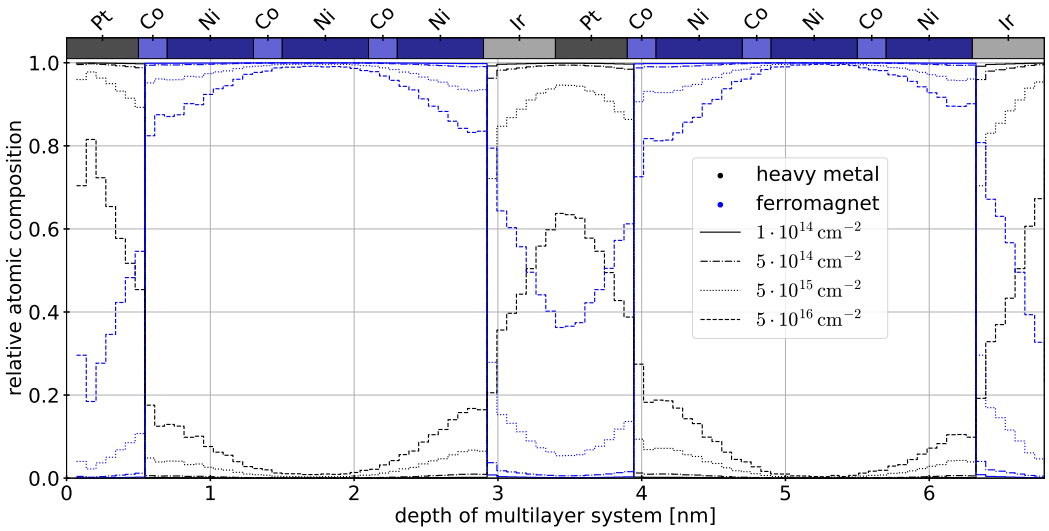

Figure 31: Simplified simulation of the intermixing of the nominal layer system in Fig. 3 (repeated on top) with different ion doses between $1 \cdot 10^{14}$ and $5 \cdot 10^{16}\,\mathrm{cm}^{-2}$. For ion doses below $5 \cdot 10^{14}\,\mathrm{cm}^{-2}$, there is hardly any difference between the bombarded and the non-bombarded sample under the aforementioned assumptions.

below $5 \cdot 10^{14}\,\mathrm{cm}^{-2}$ seems contradictory to the expectation that moderate intermixing might increase DMI [8]. As discussed in the next section 6, there are large changes in the sample properties for ion bombardment doses below $1 \cdot 10^{14}\,\mathrm{cm}^{-2}$, which might not be caused by intermixing, based on this simulation.

However, it has to be promoted, that the intermixing in Fig. 31 only represents a simulation of the ion interaction, which is not able to make direct statements about the dependencies of the magnetic parameters. In addition, the intermixing in the figure has been strongly simplified, combining several layers and neglecting effects like sputtering and ionization. A complete calculation will most likely predict stronger effects. In addition, it is also unclear how the ion bombardment affects the DMI and there exists a small possibility that the low intermixing of these doses is sufficient in explaining the observed effects in section 6.

In section 5.2, in addition to the ion bombardment in normal incidence, an ion bombardment procedure in tilted incidence has been presented. This could enable significantly reduced ion doses and thus reach dose ranges that have been less investigated in the past. This is particularly important for the samples of this work since the doses used here experimentally are already at the lower limit of the ion bombardment facility. Lower doses are therefore

only possible through modifications such as the tilted bombardment. The tilt does not only change the effective ion dose over the enlarged bombarded sample surface, but it also affects the interaction with the sample and in particular the depth profile normal to the sample surface. The latter is related to the fact that the ions have a different momentum normal to the surface if a tilt of the sample is introduced. As a result, the ions penetrate less deeply into the material on average [34]. A tilted ion bombardment can also be simulated with the program package *TRIM* from *SRIM*, with an arbitrary selection of the angle of incidence. Therefore, the simulation depicted in Figs. 30 and 31, was repeated in 5° steps, starting from normal incidence (0°) to 89°. Since orthogonal bombardment with an angle of 90° is not possible, it has been substituted by the glazing incidence angle of 89°.

Figure 32 is an expansion of Fig. 30 including the ion bombardment at an angle of 60°. The energy input and the number of vacancies in the area of the multilayer volume have roughly doubled. The individual ions, therefore, have an increased influence on the layer system,

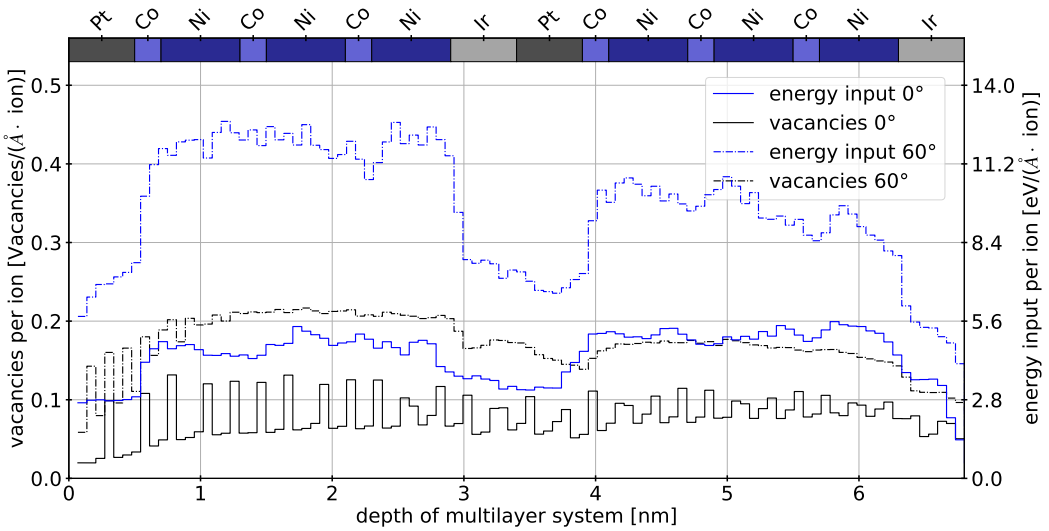

Figure 32: Simulated average energy input in eV (blue) and generated vacancies (black) per 10 keV He^+ ion in normal incidence in the layer system. The peaks of the generated vacancies correspond to the positions of the monolayers.

which counteracts the reduction in ion dose discussed in section 5.2. In the worst case, this could cancel out or at least partially compensate for the reduction in the ion dose, although this has to be verified in corresponding experiments. However, a comparison of the two blue energy curves shows another interesting behavior: In the normal-incidence case, more energy was put into the second ferromagnetic layer. In the case of a 60° angle, it's the other way around. This could make it possible to address the individual interfaces and to provide in-

formation about the question of which interface contributes to what proportion of the DMI. For example, the simulations could be used to calculate the dose and angle at which the introduced energy is kept constant at one interface, while the energy introduced at another interface changes relative to it. By deliberately varying the introduced energies or the intermixing, it might be possible to determine the modification of the DMI of each interface. It might also be possible to determine the DMI of each interface via extrapolation to the non-bombarded case. It could be helpful to perform such a large-scale experiment with another sample system with larger distances between the DMI-causing interfaces. This should increase the effect of the tilted bombardment. In addition, the method could be extended by inverting the sample system, which ideally inverts, for example, the sign of the DMI as well as the relative impact of the ion bombardment on the interfaces. No exact inversion is expected for the latter due to the material-specific stopping powers. Such an experiment would require clear definitions, e.g., about the area around an interface that is taken into account. Due to insufficient information about the effects of ion bombardment on the DMI, no statement about the definitions will be made here. In Fig. 33, the total energy contribution

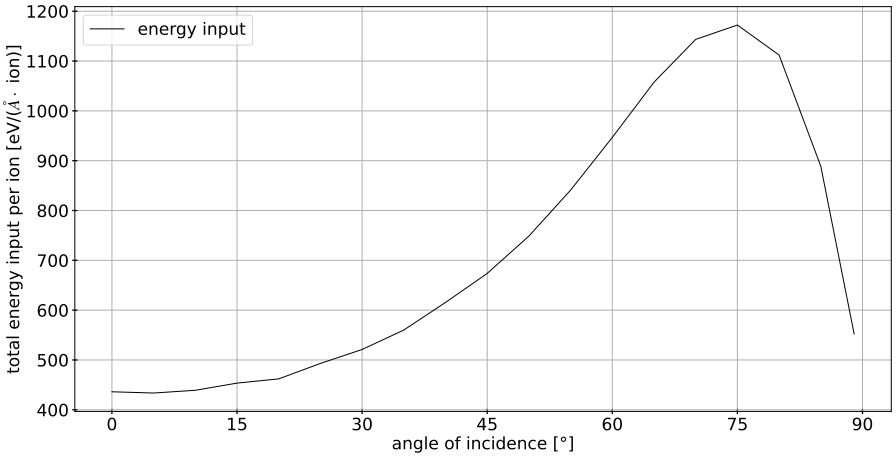

Figure 33: Simulated average energy input per ion and Å into the total multilayer system in dependence on the angle of incidence. At an angle of incidence of around 75°, almost a threefold increase is visible compared to normal incidence.

in the entire layer system is plotted as a function of the angle of incidence, which results in a characteristic curve for this property. The other parameters, like the amount of generated vacancies or ionization phenomena, also follow curves with a similar shape.

6 Evaluation of Modified DMI

As mentioned in section 5.3, two separate 10 keV He^+ ion beam bombardment experiments in normal incidence have been performed to determine the possibility and magnitude of modification of the interfacial DMI in the sample system. To determine the modification of the DMI, the modification of the saturation magnetization M_S, the effective magnetic anisotropy K_{eff} and the intrinsic DMI field H_{DMI} were determined in the sample regions bombarded with different doses. The dependence on the ion bombardment of the exchange stiffness is neglected because it was experimentally not accessible with the available setups. Consequently, it is assumed to stay constant for all doses and amounts to the same value of $A_{ex} = 1.6 \cdot 10^{-11}\,\mathrm{J\,m^{-1}}$ [16], which was presumed for the non-bombarded case. The experiments were

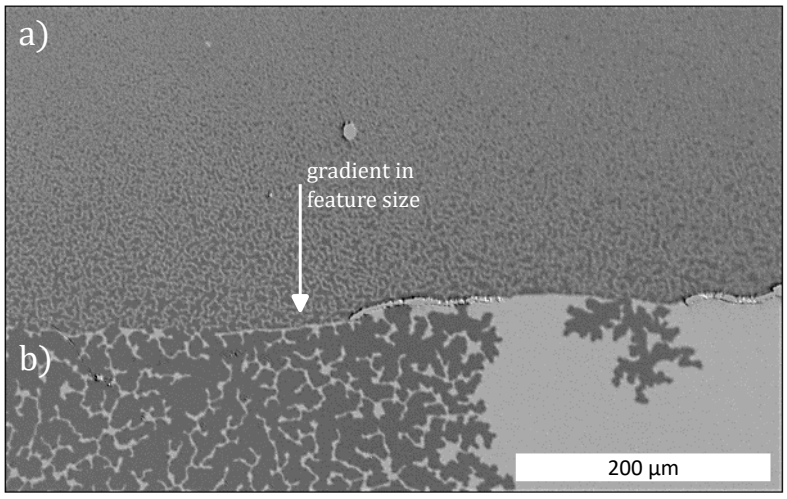

Figure 34: Border between a region bombarded with $D_{IB} = 1{\cdot}10^{14}\,\mathrm{cm^{-2}}$ and a region covered with an adhesive stripe and thus $D_{IB} = 0\,\mathrm{cm^{-2}}$. The image displays the subtraction between a positively pre-saturated state and nucleation after a single nucleation pulse. It has been additionally post-processed via a local 2D filter to enhance contrast as described in section 4.3.

essentially limited to the ion range between $D_{IB} = 1{\cdot}10^{13}\,\mathrm{cm^{-2}}$ and $1{\cdot}10^{14}\,\mathrm{cm^{-2}}$, given by the resolution of the MOKE microscope [26]. This resolution limit is linked to the phenomenon of smaller dendrimeric domain sizes with increasing ion bombardment dose. With ion doses of larger than $2.5 \cdot 10^{13}\,\mathrm{cm^{-2}}$, the domain structures are too small for being resolved by the MOKE microscope [26]. Section 7.2 discusses this phenomenon in more detail. For the determination of saturation magnetization and effective magnetic anisotropy, one sample was

also bombarded with a higher dose of $D_{\mathrm{IB}} = 1 \cdot 10^{15}\,\mathrm{cm}^{-2}$ and measured by the VVSM.
The main goal of this work is the local quantification and modification of the interfacial DMI. The quantification of the DMI field as the main method for determining the DMI is spatially restricted to the size of the FOV on the sample surface. The ion bombardment is limited to a minimum area of $2 \times 2\,\mathrm{mm}$ via focusing of electrostatic lenses with an additional square-shaped aperture. The real interaction volume between the ion beam and the sample is enlarged by scattering processes in the matter. The question of whether the modification via ion bombardment takes place locally in the bombarded region or not is briefly addressed subsequently in a qualitative way. Figure 34 displays a region of a sample with two distinct areas. In the upper area, the sample was bombarded with an ion dose of about $1 \cdot 10^{14}\,\mathrm{cm}^{-2}$, while the lower area was covered with adhesive tapes being used to block the ion bombardment in the covered sample regions. Hence, this area is expected to possess properties equal to a non-bombarded sample region. There are two clear differences between the two areas:

1. The domain structures in the bombarded region (upper area, a)) possess many times smaller feature sizes, while the domains in the region protected by the tape (lower area, b)) are comparable to the non-bombarded domains

2. The bombarded area is completely covered by domains of both oop magnetization directions In the non-bombarded region, distinct segments containing either one (light gray) or both domains (the dendrimeric region with dark gray and light gray) are visible.

Between the distinct areas, a rough border can be seen, which separates this abrupt change in the properties. A slight gradient near the border can be seen in the upper area, indicating that the properties are slightly different near the border. Possible reasons for this are inhomogeneities in the ion beam profile and the lack of bombardment in the lower area. The latter might slightly reduce the effective ion dose.It might also alter the magnetic interactions with the non-bombarded area, in which the magnetic properties are preserved. The image in Fig. 34 is qualitatively in strong agreement with a localized modification.
The following sections deal with the modified parameters, with section 6.1 dealing with the saturation magnetization, section 6.2 with the effective magnetic anisotropy, and section 6.3 with the intrinsic DMI field.

6.1 Modified Saturation Magnetization

To determine the modification of the saturation magnetization $M_S(D_{IB})$ by the ion bombardment, three samples were bombarded with ion doses of $D_{IB} = 7.5 \cdot 10^{13}\,cm^{-2}$, $1 \cdot 10^{14}\,cm^{-2}$, and $1 \cdot 10^{15}\,cm^{-2}$ over the complete sample area. The three samples are those that were previously examined in the VVSM without being bombarded. This area-wide bombardment is crucial because the measured signal in the VVSM setup originates from the total volume between the pickup coils. It is therefore imperative that the entire examined (ferromagnetic) material is bombarded as homogeneously as possible to extract the modification by the ion bombardment and the corresponding ion dose. All bombarded samples were measured in the VVSM identical to their non-bombarded condition. According to this the measurement parameters and rotation angles were the same. Thereby, the field strength is an exception because it has been applied as a loop in the range $|\mu_0 H_{ext}| \leq 1000\,mT$ to ensure that the samples have been saturated in all directions. Further measurement details can be found in section 3.1.3. In Fig. 35 the difference in the oop hysteresis curves ($m_\parallel$, $\alpha_{VSM} = 0°$) for

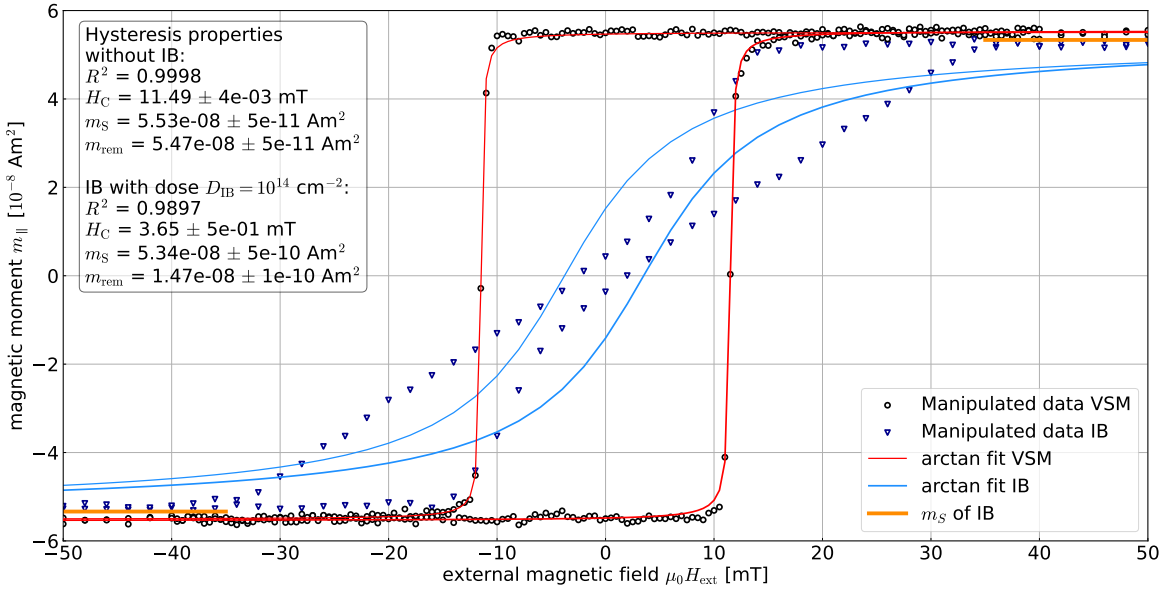

Figure 35: Exemplary depiction of the changes in the oop hysteresis before and after bombardment with an ion dose of $1 \cdot 10^{14}\,cm^{-2}$. While the saturation magnetization slightly decreases, the overall shape of the hysteresis changes, especially observable as a decrease in the coercive field, remanent magnetization, as well as a decrease in the field strength in which the magnetization reversal starts.

the sample with $D_{IB} = 1 \cdot 10^{14}\,cm^{-2}$ is shown exemplarily. Thereby, the black circles and the red lines represent the measurement points and the fitted hysteresis curve known from section 4.1. The dark blue triangles and the light blue line represents the measurement points

and the arc-tangent fit of the bombarded sample, respectively. Since the investigation of the saturation magnetization is based on the components of the saturated magnetic moment, the saturated magnetic moment $m_{\parallel,\,\mathrm{S}}$ determined by the fit is marked in orange at the edges of the plot.

The bombarded hysteresis curve in Fig. 35 possesses four differences compared to the pre-bombarded hysteresis curve. The strength of the respective difference relative to the original hysteresis curve is dependent on the ion dose. The four differences are:

1. The magnetic moment in saturation of the bombarded moment is slightly below the magnetic moment of the non-bombarded sample

2. The shape of the hysteresis curve changed after the ion bombardment. The magnetic reversal takes place over a significantly larger field range, which is reflected in the lower gradients of the magnetic reversal process. In addition, there are two field regions of the magnetization reversal process with different gradients: the first one with a very steep gradient until the coercive field is almost reached and the second region with a significantly lower gradient till the saturation magnetization is reached. Such regions with differing slopes might arise from different magnetization reversal mechanisms. The coercive field is reduced to about a third in comparison to the non-bombarded case

3. The external magnetic field at which the magnetization reversal process starts is significantly reduced. This causes a directional reversal process when ion dose gradients are present in the sample [26]. This effect is in direct competition with the asymmetric bubble expansion method, which is the reason why gradients in the ion bombardment for the MOKE samples have to be avoided

4. The remanent magnetic moment is also significantly reduced. As visible in the plot, this means that with the dose of $D_{\mathrm{IB}} = 1 \cdot 10^{14}\,\mathrm{cm}^{-2}$ and no applied field, a remanent magnetization of $M_{\mathrm{rem}}(\mu_0 H_{\mathrm{ext}} = 0\,\mathrm{mT}) \approx 0\,\mathrm{kA\,m}^{-1}$ is present. Since this state is reached from saturation, it is most likely independent of the pre-treatment with magnetic fields. In comparison to investigations with the MOKE microscope, this state most likely corresponds approximately to the domain structure in the upper region in Fig. 34. For the asymmetric bubble expansion method, this represents an impossible initial state.

Section 6.3 will elaborate on these last two points concerning the asymmetric bubble expansion technique. For the investigation of saturation magnetization, the first two points are

more crucial. In particular, the second point causes that the arc-tangent function may not be fitted accurately for reproducing the remagnetization process. If the magnetization reversal process involves several mechanisms, a sum of several arc-tangent functions might be able to describe the magnetization reversal. However, since the fit can precisely determine the respective component of the magnetic moment in saturation (see orange line in Fig. 35) and this is the only important parameter for determining the saturation magnetization and the effective magnetic anisotropy, the rest of the evaluation is still based on strand dependent fits of simple arc-tangent functions. Note that the arc-tangent fit gets in saturation at higher, not displayed field strengths.

The components of the saturated magnetic moment parallel $m_{\parallel,\,\mathrm{S}}$ and orthogonal $m_{\perp,\,\mathrm{S}}$ to the external magnetic field are again determined for all rotation angles. Based on Eq. (76), an angle-dependent averaging, and Eq. (56), the saturation magnetization is calculated in dependence on the three ion doses mentioned at the beginning of this section. For the sample surface area A, the values given in Tab. 3 are applied sample specifically. The layer thickness has been assumed to be constant and equal to the value $t_{\mathrm{layer}} = 6.7\,\mathrm{nm}$ calculated with the minimization function in Eq. (77). The calculated saturation magnetizations are summarized in Fig. 54 in dependence on the ion dose. The shown values are given in multiples of the saturation magnetization $M_{\mathrm{S}}(0) = 591\,\mathrm{kA\,m^{-1}}$ of the non-bombarded sample. In addition, only the saturation magnetizations for the two ion doses $D_{\mathrm{IB}} = 7.5 \cdot 10^{13}\,\mathrm{cm^{-2}}$ and $1 \cdot 10^{14}\,\mathrm{cm^{-2}}$ are displayed because the last ion dose of $D_{\mathrm{IB}} = 1 \cdot 10^{15}\,\mathrm{cm^{-2}}$ is significantly outside of the region in which the intrinsic DMI field has been determined. Extrapolation over such a large ion dose range with only the available few points might lead to false conclusions about the lower dose range. Originally it was planned to cover a larger ion dose range with all three experimentally available parameters, but this was limited by the amount of sample material. A full plot, including the $1 \cdot 10^{15}\,\mathrm{cm^{-2}}$ dose, can be found in appendix section 9.4. The dose-dependent saturation magnetization is fitted with a linear function (and an additional exponential function in Fig. 54) to describe this dependency. This fit is later utilized to interpolate the saturation magnetization for non-measured ion doses. Since it is based on only three points, its validity should be treated with caution. However, since the saturation magnetization has decreased for all ion doses (see Fig. 54) and the decrease is enhanced with higher ion doses, at least a qualitative statement can be made concerning the interfacial DMI: According to Eq. (70), a decrease in the DMI with the saturation magnetization is expected.

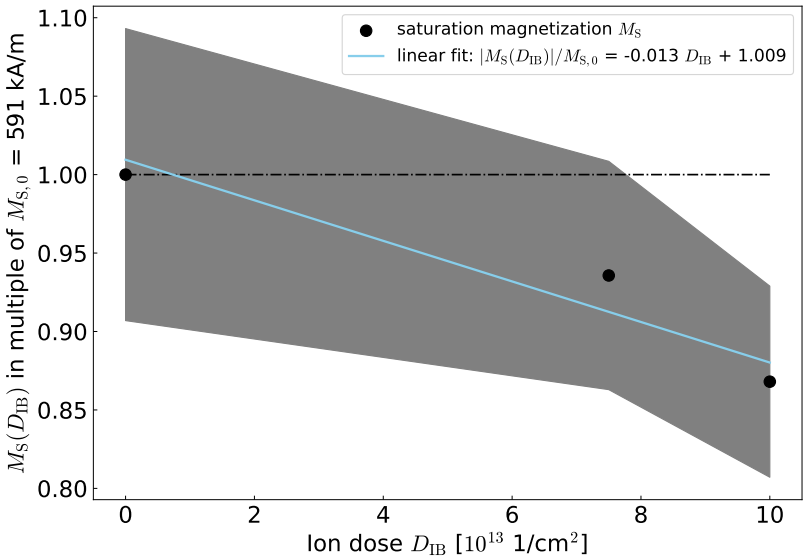

Figure 36: Dependence of the saturation magnetization M_S (black circles) on the ion bombardment dose D_{IB} in the region between $D_{IB} = 0\,cm^{-2}$ and $1 \cdot 10^{14}\,cm^{-2}$ in multiple of $M_S(D_{IB} = 0\,cm^{-2})$. The general dependency is interpolated with the linearly decreasing function (blue) in the legend, whereby its informative value is questionable due to the few data points. In appendix section 9.4, Fig. 54 the ion dose $1 \cdot 10^{15}\,cm^{-2}$ and an exponentially decreasing fit are included.

6.2 Modified Effective Magnetic Anisotropy

The determination of the modification of the effective magnetic anisotropy K_{eff} with the ion bombardment dose D_{IB} is based on the same hysteresis loops described in the last section 6.1. In the last section also the general differences of the hysteresis curves have been discussed. The evaluation and determination of K_{eff} are equal to the process described in section 4.2, whereby the hystereses in this section have been measured in the range of $|\mu_0 H_{ext}| \leq 1000\,mT$. Therefore, this time there is no need of extrapolating the magnetic moment components for the magnetic field strength of $\mu_0 H_{ext} = 300\,mT$ (see section 4.1).

For this field strength, it was confirmed beforehand, that the magnetic saturation was reached. The angular-dependent torque was determined and normalized to the mean saturation magnetization via the associated saturation magnetization. The resulting torque curve is fitted to the derivates of the first two power series for the uniaxial oop magnetic anisotropy in Eq. (46), which is exemplarily depicted in Fig. 37 for an ion dose of $1 \cdot 10^{14}\,cm^{-2}$. The effective magnetic anisotropy constant K_{eff} is again calculated as the arithmetic mean of the constants K_1 of both fits. Comparison with the torque curve in Fig. 14 shows that the general curve and shape are equal, whereby the bombarded torque curve is smoother. However, the anisotropy

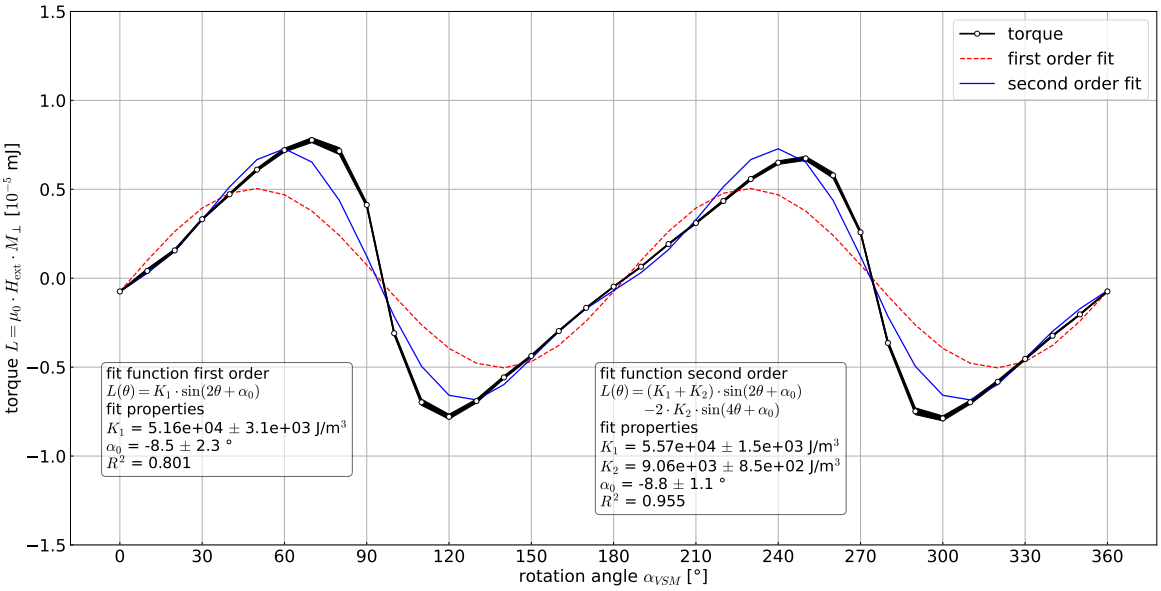

Figure 37: Torque curve $L(\theta, 300\,\mathrm{mT})$ of the sample bombarded with an ion dose of $D_{\mathrm{IB}} = 1 \cdot 10^{14}\,\mathrm{cm}^{-2}$ with a normalized uniform magnetization. The two fits correspond to the first derivative of the first two orders $f^{(1)}_{\mathrm{anis}}(\theta)$ and $f^{(2)}_{\mathrm{anis}}(\theta)$ of the sin-function power series of Eq. (46).

constants K_1 of both fits are reduced to roughly one quarter of the original value which is a considerable modification compared to the saturation magnetization. As for the saturation magnetization, the magnitude of the modification depends on the ion dose. The modification which is almost entirely limited to the anisotropy constants K_1 and K_2. The dependence of the effective magnetic anisotropy on the ion doses in the range of 0 to $1 \cdot 10^{14}\,\mathrm{cm}^{-2}$ is summarized in Fig. 38. A complete plot, also containing a fit of an exponentially decreasing function is displayed in appendix section 9.4 in Fig. 55. Hereby, it should be highlighted that the effective magnetic anisotropy constants of the ion doses $D_{\mathrm{IB}} = 1 \cdot 10^{14}\,\mathrm{cm}^{-2}$ and $1 \cdot 10^{15}\,\mathrm{cm}^{-2}$ differ slightly compared to the overall trend. The strongly decreasing trend in Fig. 38 has two advantages, whereby the quantitative informative value is limited due to the small number of data points. According to Eq. (70), the DMI D is proportional to the reciprocal square root of the effective magnetic anisotropy

$$D \propto \frac{1}{\sqrt{K_{\mathrm{eff}}}}\,, \tag{87}$$

and therefore a decreasing trend in the oop anisotropy leads to an increasing contribution to the DMI. Thus, the change in effective magnetic anisotropy counteracts the change in saturation magnetization. The second reason involves that the strong perpendicular magnetic anisotropy corresponding to Eq. (44) is caused by interface states. Such a large change in

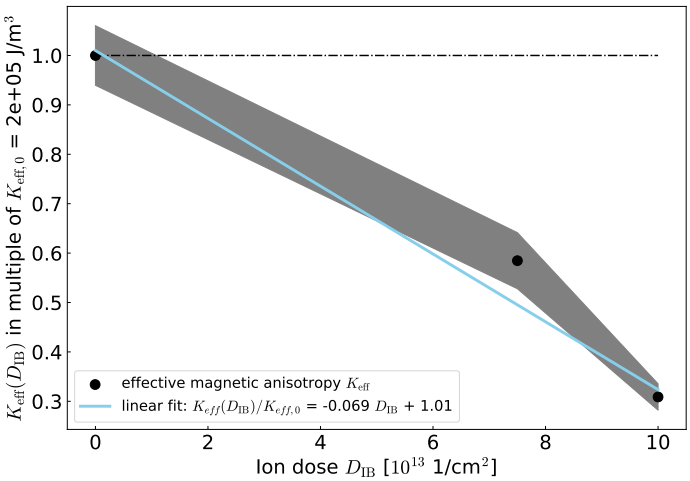

Figure 38: Dependence of the effective magnetic anisotropy K_{eff} (black circles) on the ion bombardment dose D_{IB} in the region between $D_{\mathrm{IB}} = 0$ and $1 \cdot 10^{14}\,\mathrm{cm}^{-2}$ in multiple of $K_{\mathrm{eff}}\,(0\,\mathrm{cm}^{-2})$. The general dependency is interpolated with the linearly decreasing function (blue) in the legend, whereby its informative value is questionable due to the few given data points. In appendix section 9.4, Fig. 55 contains additionally the ion dose $1 \cdot 10^{15}\,\mathrm{cm}^{-2}$ and an exponentially decreasing fit.

the anisotropy is therefore very likely to include changes in these interface states. Since the DMI appears here as an interfacial effect, its modification is expected to require changes at the interfaces. The modification of the anisotropy is therefore likely to include modifications of the DMI.

6.3 Modified Intrinsic DMI Field

The last experimentally accessible quantity is the intrinsic DMI field H_{DMI} which involves the optical asymmetric bubble expansion method. As already mentioned and exemplarily shown in Fig. 34, the feature size of the dendrimeric domains decreases significantly upon ion bombardment. Ion doses above $D_{\mathrm{IB}} = 2.5 \cdot 10^{14}\,\mathrm{cm}^{-2}$ could not be resolved in a previous work [26]. Although this limit might require a re-examination, especially according to the results in section 7.2, the first attempts for the determination of the DMI field were limited to ion doses below $1 \cdot 10^{14}\,\mathrm{cm}^{-2}$, whereby further tests could not be carried out due to limited sample material and experimental time.

In addition to the reduced domain feature sizes and the associated resolution problems in the MOKE microscope, there are further difficulties with the bombarded samples, which were briefly addressed in section 6.1. First of all, with an increasing ion dose, the magnetic reversal process starts at lower absolute field strengths if saturation is assumed as the starting point.

This means, that the magnetic reversal process always starts in the regions with the highest ion doses and, in the case of existing gradients, spreads along this gradient towards less bombarded areas via domain wall movement. Since ion gradients thereby generate a directed domain wall motion, they are in direct concurrence with the field-driven domain expansion of the asymmetric bubble expansion method. Perhaps with more research, it would be possible to combine both effects, e.g. to determine the ion gradient with known non-bombarded DMI strength.

Secondly, the remanence magnetization decreases rapidly with increasing ion dose, being close to $M_{\mathrm{rem}} \gtrsim 0\,\mathrm{kA\,m^{-1}}$ with an ion dose of $1 \cdot 10^{14}\,\mathrm{cm^{-2}}$ as shown in Fig. 35. This is problematic because the asymmetric bubble expansion method requires a saturation state as the initial state for nucleation and subsequent growth ($M_{\mathrm{rem}} \approx M_{\mathrm{S}}$). The initial, saturated state in remanence is not guaranteed if the region has been bombarded with higher doses, in which the remanent state has been observed to always resemble the upper region in Fig. 34. One possibility to still enable the asymmetric bubble expansion method might be an additional offset in the form of a constant oop magnetic field $H_{\mathrm{z,\,off}}$. If the experiment is started, for example, in positive saturation, the external oop magnetic field would not be reduced to $0\,\mathrm{mT}$ but to $H_{\mathrm{z,\,off}} > 0\,\mathrm{mT}$, which has to be chosen so that $M(H_{\mathrm{z,\,off}}) \approx M_{\mathrm{S}}$ holds. Starting from this point, pulsed growth could be achieved by further reducing the field frequently. However, it can be assumed that in this case, the basic creep law according to Arrhenius has to be adapted.

Both problems occur particularly with ion doses above $1 \cdot 10^{14}\,\mathrm{cm^{-2}}$. For this reason, samples bombarded with such high ion doses could not be examined with the asymmetric bubble expansion method and these samples will therefore not be mentioned further in this work. Hereby, the main reason for the non-applicability of the asymmetric bubble expansion method is the presence of ion gradients. The problems were either not observed for the sample bombarded according to Fig. 29 or it was always possible to find sample regions in which the problems did not occur. All statements related to the intrinsic DMI field as a function of ion bombardment are therefore only based on a single bombardment process on a single piece of sample.

Besides the reduction in domain size, no significant differences were observable in the experimental investigation of the asymmetric bubble expansion in bombarded regions. Section 7.2 further investigates this dependence, whereby Fig. 43a displays a direct artificially generated comparison between the domains of the non-bombarded region and the region bombarded

with a dose of $7.5 \cdot 10^{13}\,\mathrm{cm}^{-2}$. However, one positive observation was obtained: According to the subjective assessment, the bombarded samples had less disruptive appearances from neighboring domains, which made the measurements more pleasant. However, this was not investigated further and it is unclear whether this originates from the ion bombardment or simply from the change of position on the sample surface.

The curves recorded via the asymmetric bubble expansion are summarized in appendix section 9.4 Tab. 7, whereby the left column contains measurements with a negative pre-saturation and the right column contains measurements with a positive pre-saturation. Also included in the table are the measurements of the non-bombarded regions. The intrinsic DMI fields H_{DMI} are summarized in the plots in Fig. 39, whereby the dependence on the ion dose is displayed for both pre-saturation separately on top and as the average of both pre-saturation directions in the lower plot. In all cases a decrease of the DMI field of up to 40% relative to

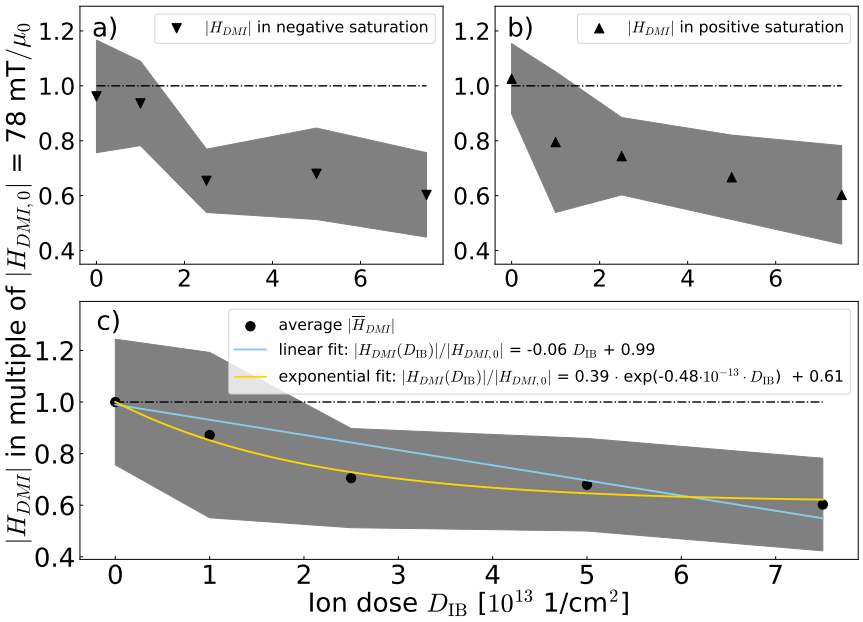

Figure 39: Dependence of the intrinsic DMI field H_{DMI} on the ion bombardment dose in the range of 0 to $7.5 \cdot 10^{13}\,\mathrm{cm}^{-2}$ for a negative pre-saturation (top, a)) and positive pre-saturation (top, b)) as well as the average for both pre-saturations (bottom, c)) in multiples of the averaged $H_{\mathrm{DMI},\,0}$. The averaged trend is fitted by a linearly (blue) and exponentially decreasing function (yellow), given in the legend.

the non-bombarded case is visible. The averaged curve is fitted once via a linearly decreasing (blue) and once via an exponentially decreasing function (yellow), which both are given in the respective legend. Since the DMI D is directly proportional to the DMI field H_{DMI}, as

described in Eq. (70), this trend indicates a decreasing DMI strength.

Together with the trends for saturation magnetization and effective magnetic anisotropy, there are two decreasing trends and one increasing trend for the effect on the DMI. Thereby, indicating the trends as arrows in the index, the DMI is given by

$$|D\,(D_{\mathrm{IB}})| = \left|\mu_0 \cdot H_{\mathrm{DMI}}\,(D_{\mathrm{IB}})_{\downarrow} \cdot M_{\mathrm{S}}\,(D_{\mathrm{IB}})_{\downarrow} \cdot \sqrt{\frac{A_{\mathrm{ex}}}{K_{\mathrm{eff}}\,(D_{\mathrm{IB}})_{\downarrow}}}\right| . \tag{88}$$

To determine the overall trend of the DMI, the DMI of the individual measured ion doses in the range of 0 to $1 \cdot 10^{14}\,\mathrm{cm}^{-2}$ have been determined. For this, the intrinsic DMI field strength H_{DMI} has been extrapolated for the ion dose $D_{\mathrm{IB}} = 1 \cdot 10^{14}\,\mathrm{cm}^{-2}$, and for the ion doses $1 \cdot 10^{13}\,\mathrm{cm}^{-2}$, $2.5 \cdot 10^{13}\,\mathrm{cm}^{-2}$, and $5 \cdot 10^{13}\,\mathrm{cm}^{-2}$ the saturation magnetization M_{S} and the effective magnetic anisotropy K_{eff} were interpolated. For the extra- and interpolation, the linear fits of this chapter 6 as well as the exponential fits in the appendix section 9.4 have been applied. The resulting DMI values are summarized in Fig. 40, in which the blue points represent the linearly estimated DMI values while the yellow dots represent the exponentially estimated values. For the data points of $D_{\mathrm{IB}} = 0\,\mathrm{cm}^{-2}$ and $7.5 \cdot 10^{13}\,\mathrm{cm}^{-2}$, all parameters have been measured completely, which is the reason why they appear identical in both curves. Except

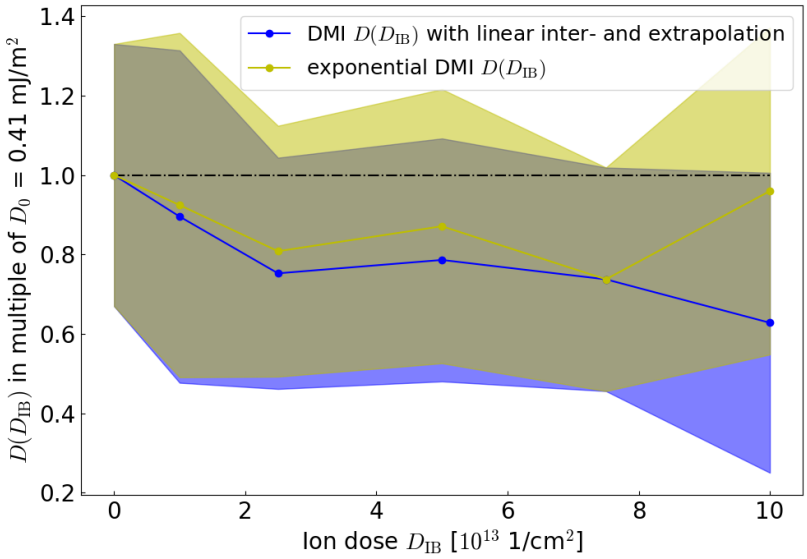

Figure 40: Dependence of the DMI strength on the ion bombardment dose in the range of 0 and $1 \cdot 10^{14}\,\mathrm{cm}^{-2}$, whereby missing data points are either interpolated with linear fits (blue) or exponential fits (yellow). The fits are given in Figs. 39, 36, 54, 38, and 55.

for the last point with a dose of $1 \cdot 10^{14}\,\mathrm{cm}^{-2}$, both estimated curves display approximately the same trend, which predicts a decrease of up to about 40%. Remarkably, the exponentially estimated curve rises again to almost the original value at this last ion dose. Considering

the assumption that moderate intermixing could lead to an increase in the DMI and high intermixing could lead to a decrease of the DMI via destruction of the interfaces or sample system, this sudden increase seems unlikely. Since M_S and K_{eff} of this point were determined experimentally, the supposedly overestimated DMI value could occur due to an overestimated intrinsic DMI field if fitted exponentially.
Overall, the trend indicates a steady decrease in the DMI, although the large uncertainties would in principle also agree with a slightly increasing or a constant DMI.

7 Further Investigations

In the following first two sections, sample properties that are not directly connected to the determination or modification of the DMI are examined. For this objective, section 7.1 will deal with the H_x-field and domain growth directions in the KERR microscopic setup (see section 3.2), and section 7.2 with the reduction of the feature sizes of the domain texture upon ion bombardment and applied in-plane field strength.
Furthermore, section 7.3 will provide a few approaches that might enable an improved, automatized measurement procedure in the future.

7.1 Growth Directions and Field Alignment

During all asymmetric bubble expansion experiments conducted so far, the main asymmetry of the growth velocity was assumed to appear parallel to the x-axis of the MOKE images (see sections 3.2.4 and 4.3). On one hand, this section deals with the question of whether the asymmetry is truly expressed primarily along this axis and, on the other hand, it is considered whether the asymmetric growth is symmetric to the applied absolute field strengths, as assumed in the model described in section 3.2.3. The latter might be linked to one of the most important experimental conditions to be considered: the mutual orientation of the magnetic fields, the sample surface, and the camera.
The sample surface, the in-plane field, and the camera are aspired to be orientated parallel to each other (in-plane) whereby the z-field should be orthogonal to all (out-of-plane). This alignment is required for the deliberate control of the individual field axes. For the quantification in this section, two parameters are to be examined: Firstly, the main axis of the asymmetric growth within the image, and secondly, the alignment of the externally applied magnetic fields relative to the sample's surface normal.

Main Axis of Asymmetry

For all asymmetric bubble expansion measurements, the domain wall velocity has been extracted along the x-axis of the recorded MOKE images (see section 4.3), based on the underlying assumption that the x-axis of the recorded images matches perfectly with the external magnetic field in-plane.

However, this assumption is solely based on the manual alignment of the external magnetic field relative to the camera. Additionally, section 3.2.3 briefly discussed a model in which the axis of the external magnetic field in-plane does not necessarily have to coincide with the axis of strongest asymmetric growth. This is the axis with the largest difference in domain wall growth velocities and is henceforth referred to as the main axis of asymmetry. It is unclear whether this model is practicable for the investigated domains. During the experiments, a clear trend of the growth velocity along the x-axis of the recorded images was visible, which is to be quantified and verified in this section.

For determining the axis of strongest asymmetry, the movement of the center of mass is utilized. In presence of an asymmetric growth axis, the center of mass moves along the direction of the stronger pronounced growth. This direction is parallel to the axis of the strongest asymmetry if the growth orthogonal to the axis is mirror symmetric to it, which is assumed to be the case here. Therefore, the axis of the strongest asymmetry is set to be parallel to the movement direction of the center of mass, determined by a linear fit.

Thus, the center of mass has been determined pulse-dependently for the binarized images of each asymmetric growth series with its specific in-plane field. Figure 41 exemplarily displays this evaluation method (a)) with a positively pre-saturated asymmetric bubble expansion measurement series in presence of a $\mu_0 \cdot H_{\text{ext}} = -60\,\text{mT}$ ip field. The direction of the movement is determined by the enclosed angle in between the linear fit and the x-axis of the image as shown in Fig. 41. Thus, the angle α_{asym} is determined by the slope a_{asym} of the linear fit according to

$$\alpha_{\text{asym}} = \arctan a_{\text{asym}} \,. \tag{89}$$

Once the growth of the domain exceeds the FOV on one of both image edges, the center of mass in the FOV is not accurately representing the asymmetry of the growth. Therefore, the linear fit is solely applied to the center of masses in which the growth is contained in the FOV as discussed in section 4.3.4. The fit is additionally restricted to measurement series in which at least three growth pulses are contained in the FOV to reduce the otherwise strong impact of statistical fluctuations. Figure 41 b) summarizes the enclosed angles of 221

measurement series which fulfill the mentioned conditions. This includes bombarded as well as non-bombarded sample regions, positive and negative pre-saturation, and positive and negative ip field strengths and therefore represents the entirety of all performed asymmetric bubble expansion measurement series. The polar histogram possesses a dominant portion

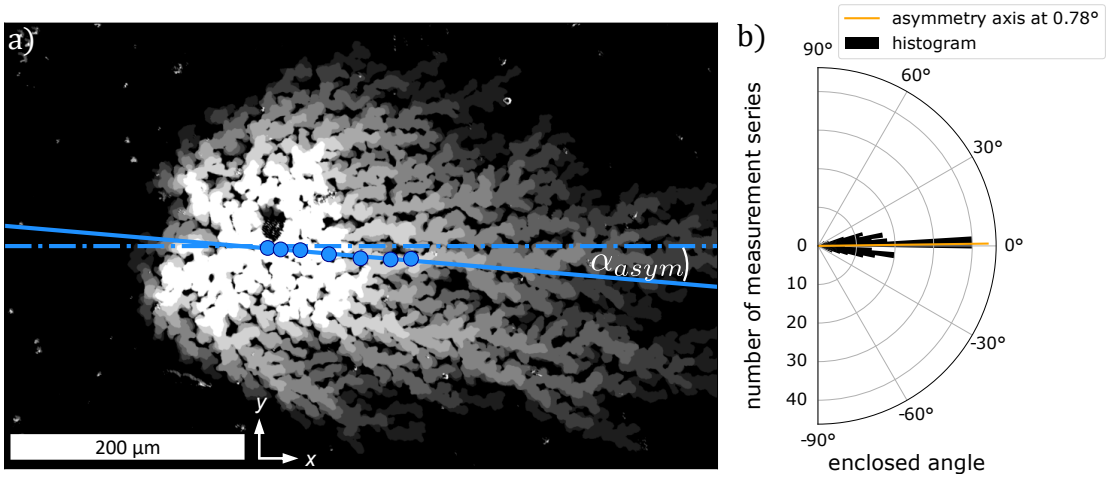

Figure 41: Determination for the axis of the strongest asymmetry with an example of the measurement procedure displayed in a) and a polar histogram, containing all asymmetric bubble expansion measurements in b). The determination is based on the enclosed angle α_{asym} between the image's x-axis (dotted blue line) and the linear fit (solid blue line) of the movement of the center of mass (blue dots) in a series of binarized images. Averaging over all angles leads to an asymmetry axis (orange) tilted by 0.78° relative to the image's x-axis.

along $\alpha_{\mathrm{asym}} \simeq 0°$ as well as two roughly equal-sized portions around $\pm 10°$, which result in an average enclosed angle of 0.79°.

Considering the movement of a center of mass in absence of an external ip field, it roughly stays within a Δx, $\Delta y = \pm 5\,\mathrm{px}$ space of the initial center of mass after the nucleation pulse. This observation may indicate an isotropic growth of the dendrimeric domain texture on average, which would agree with the roughly uniform growth of the domain. This can be observed, for example, in the overview in Fig. 15. This also limits the evaluation method based on the linear fit of the movement of the center of mass. For no or very small field strengths, the fit direction is governed by statistical noise instead of an asymmetry axis since it is not present or extremely weak. Future considerations based on this or an equal method may be adapted by, e.g., weighting the enclosed angles α_{asym} by the absolute ip field strength or the distance traveled by the center of mass per pulse. Another approach might be the exclusion of measurement series in which the center of mass remains in a small area of, for example, a circle with a radius of 5 px.

Due to the statistically rather isotropic growth, the two comparably large portions which are roughly symmetrical to the mean value might occur as part of statistical fluctuations in the growth directions and linear fits. Besides the statistically associated widening of the enclosed angles, there might be the possibility of two main axes of asymmetry, attributed to the two direction possibilities for pre-saturation, the different signs of the ip field, or a combination of both. In such a case, the contributions of both axes of asymmetry, if equally far apart from the x-axis, could cancel each other out in the mean value of all asymmetric bubble expansion experiments displayed in Fig. 41. Separation of the angles by saturation direction, ip field direction, and the combinations of both, which has not been performed here, could provide information about whether deviating preferred direction of growth exists.

If there are two main axes of asymmetry, these are unlikely to be caused by deviations in the relative orientation of the field with the camera, since in such a case only rotation of the principal symmetry axis is expected to occur. Nevertheless, the experiment could be repeated with other samples with different properties, like the domain texture or anisotropy, to ensure that the possible two main axes of asymmetry are caused by the sample's properties.

Determination of the domain wall velocity with arbitrary angles of the ROI to the ip field could also provide additional information. In general, an angle-dependent determination of the velocity is considered useful for future evaluations and measurements since it is a relatively easy approach to extract more data from the images, which are mainly experimentally limited here.

Orthogonality of External Magnetic Fields

For an idealized alignment of the oop and ip field relative to the sample surface, as well as a single main axis of asymmetry along the x-axis ($\alpha_{\mathrm{asym}} = 0°$), the model in section 3.2.3 expects the asymmetry to be symmetric regarding the absolute field strengths.

According to Eq. (70), the growth velocity depends on the absolute value of the superposition of the external ip field $\vec{H}_{\mathrm{x}}$ and the intrinsic DMI field $\vec{H}_{\mathrm{DMI}}$. Hereby, the velocity of the dendrimeric domain is determined along the x-axis and thus, ideally, along the external ip field. Simplified, the dendrimeric domain possesses two kinds of domain walls along this field axis, which are oriented antiparallel to each other. Comparing these to the external field always results in one parallel and one antiparallel superposition between the intrinsic and externals fields, which is the origin of the asymmetric growth velocity (see section 3.2.3). Consequently, the inversion of the in-plane field inverts the asymmetric growth since the

parallel and antiparallel superposition is reversed. Thus, for the domain growth velocities,

$$\frac{v_{\mathrm{r}}(H_{\mathrm{x}})}{v_{\mathrm{l}}(-H_{\mathrm{x}})} \simeq 1 \tag{90}$$

applies within the measurement inaccuracies, if the alignment is sufficient. Another way of looking at this condition is that the asymmetric bubble expansion curve of one direction (or domain wall normal) should be mapped onto the curve of the other direction by taking the mirror curve along the y-axis. In Fig. 42 Eq. 90 has been applied exemplarily for the asymmetric bubble expansion curves of Fig. 24 with positive (blue) and negative pre-saturation (orange). The displayed field strengths are reduced to the values H_{x} for which both direction-dependent velocities $v_{\mathrm{r}}(H_{\mathrm{x}})$ and $v_{\mathrm{l}}(-H_{\mathrm{x}})$ have been measured. An increase

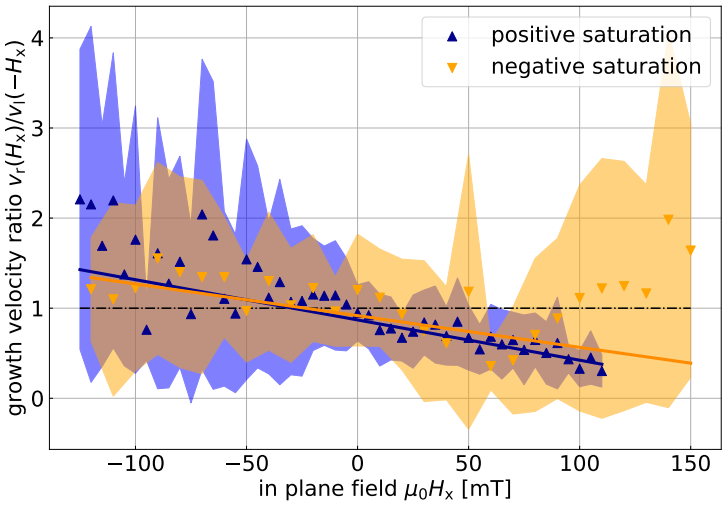

Figure 42: Ratio of the velocities along the right side $v_{\mathrm{r}}(H_{\mathrm{x}})$ and the velocities along the left side $v_{\mathrm{l}}(-H_{\mathrm{x}})$ but with opposite in-plane field direction. The blue curve displays the ratio with positive pre-saturation (Fig. 24b) and the orange curve with negative pre-saturation (Fig. 24a). The idealized trend of 1 is indicated by the dotted black line.

in the same direction can be seen for both pre-saturations. In general, such an increase might be caused by a sample tilt along the y-axis[4], whereby both applied magnetic fields $\vec{H}_{\mathrm{x}}$ and $\vec{H}_{\mathrm{z}}$ possess an ip and oop component depending on the tilting angle. Thus, they superimpose each other resulting in amplification or reduction of the effective field strength, depending on the applied field directions. This should lead to a slope in the representation in Fig. 42, depending on the sample tilt as well as $\vec{H}_{\mathrm{x}}$ and $\vec{H}_{\mathrm{z}}$. In general, the oop field strength was between $|\mu_0 \cdot H_{\mathrm{z}}| = 8 - 12\,\mathrm{mT}$, while the ip field strength varied in a range of

[4]Idealized, this method is not sensitive to tilting along the x-axis since the ip field does not have a component orthogonal to the x-axis.

more than ±150 mT. Differences in the velocity ratio due to a sample tilt along the y-axis are expected, especially at high ip fields. However, the common slope for both saturation magnetizations in Fig. 42 is not expected to be caused by sample tilting since the inversion of the saturation should lead to an inversed superposition with the in-plane field and thus to a negative slope. Therefore, a sample tilt should be visible as a cross of the trends for both saturation directions. Besides the general large uncertainties in the measurement, the origin of this common trend is unclear.

In Tab. 4, the trends for the velocity ratios analogously to Fig. 42 are summarized in dependence on the ion bombardment dose and pre-saturation direction. The trend is thereby given by the angle β between the linear interpolation and the idealized case of 1, i.e., how strongly the linearly fitted trend is rotated in comparison to the ideal case.

Table 4: Summary of the angles β by which the linear fit of the ratio of the domain wall velocities is rotated compared to the ideal case.

IB dose D_{IB} $[1 \cdot 10^{13}\,\mathrm{cm}^{-2}]$	0	1	2.5	5	7.5
β for positive pre-saturation [°]	-14.7	16.9	1.1	-8.2	3.3
β for negative pre-saturation [°]	-11.5	-11.1	-9.5	-13.3	-17.9

Thereby, two peculiarities arise:

1. For negative pre-saturation, the rotation angles are comparable and possess the same sign, while the rotation angles for positive pre-saturation differ from each other

2. Two crossed trends of the velocity ratio, associated with a sample tilt, is expressed by two angles with opposite sign, which are expected to possess a decisive but unknown difference. Such an angle pair is presumably visible for the sample region with $D_{\mathrm{IB}} = 1 \cdot 10^{13}\,\mathrm{cm}^{-2}$ and less significant for the sample region with $D_{\mathrm{IB}} = 7.5 \cdot 10^{13}\,\mathrm{cm}^{-2}$.

Since all samples were measured with the same structure and no consistent trend is visible in Tab. 4, no statement can be made about the tilting of the sample. Figure 42 also shows that the ideal case falls within the associated uncertainty range for almost all measured ratios. If the measurement accuracy can be increased (see section 7.3), this method might enable the detection of a tilt in the sample. Taking into account the values for the field strengths, it might also be possible to estimate the angle.

7.2 Domain Size Distribution

During the experiments as well as their evaluation it has been noticed that the spatial feature size of the dendrimeric domains decreases both with the ion bombardment dose and with the absolute applied in-plane field. This is schematically depicted in the artificially stitched images in Fig. 43. To investigate and quantify both of these phenomena, the raw MOKE images, and the binarized images are analyzed via FOURIER transformation, which addresses the feature sizes contained in the images. The 2D-FOURIER analysis extracts the spatial

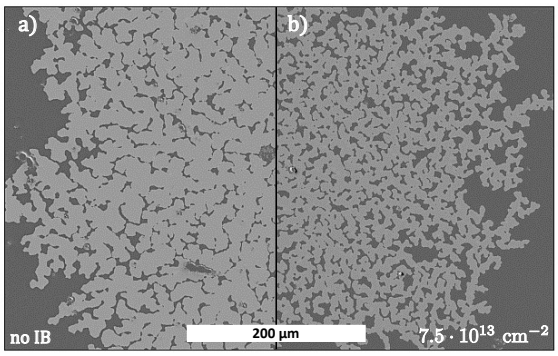

(a) Example of the decrease in the dendrimeric domain sizes between the non-bombarded sample on the left (a)) and the sample bombarded with an ion dose of $D_{\mathrm{IB}} = 7.5 \cdot 10^{13}\,\mathrm{cm}^{-2}$ on the right (b)).

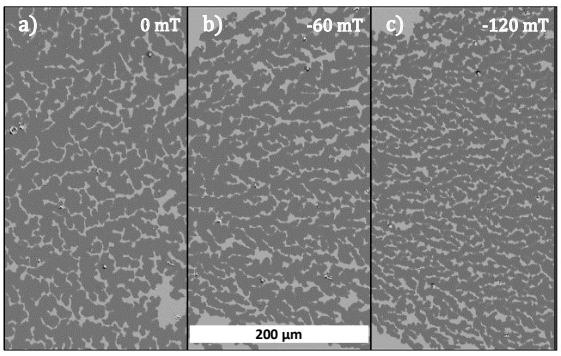

(b) Example of the decrease in the dendrimeric domain sizes of the non-bombarded sample region with an increasing absolute in-plane field strength, with $\mu_0 H_{\mathrm{x}} = 0\,\mathrm{mT}$ (a)), $\mu_0 H_{\mathrm{x}} = -60\,\mathrm{mT}$ (b)), and $\mu_0 H_{\mathrm{x}} = -120\,\mathrm{mT}$ (c)).

Figure 43: Examples for the decrease in the dendrimeric domain sizes with ion bombardment in Fig. 43a and with in-plane field strength in Fig. 43b.

frequencies contained in the grayscale images and is thus especially useful if periodic features are investigated. The dendrimeric domain structures seem chaotic and irregular but may contain frequent spatial characteristics like the distances at which a single branch splits. The size evaluation is based on [37], which has already been successfully applied to the domain structures [26]. The investigation is exemplarily displayed for a non-bombarded domain image in Fig. 44a whose numerical Fast FOURIER Transformation (FFT) results in Fig. 44b. In this image, the spatial frequency components are contained in an absolute logarithmic scale. It possesses an elliptically centered structure that originates from the non-squared image size of $1920\,\mathrm{px} \cdot 1200\,\mathrm{px}$. A bright spot in the center and a darker ellipse at a small distance from the center can be seen. Starting from the center of the image, the values of the FFT image

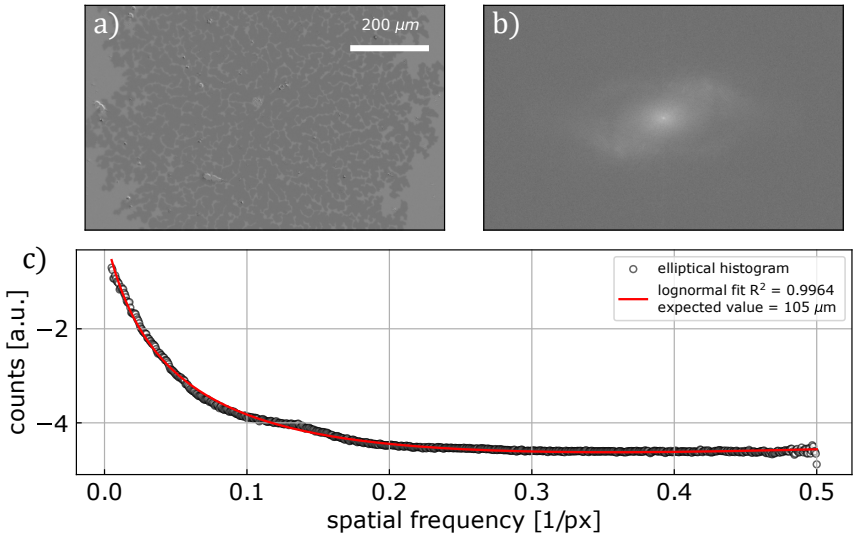

Figure 44: Exemplary calculation of the feature size of a non-bombarded sample region (a)) via FOURIER transformation (b)) and subsequent formation of a elliptical histogram (c)). The expectation value for the feature size is estimated by the expectation value of a fitted lognormal distribution.

reflect the spatial frequency in the respective direction in multiples of the corresponding image dimension [37, 26]. This means that all values on an ellipse around the image center with a ratio of major and minor axes reflecting the image dimensions correspond to the same spatial frequency. The 2D FOURIER transformed image was thus converted into a histogram $N(f_{\mathrm{ellip}})$ by summing up all values within such a frequency ellipse f_{ellip}, starting from the center of the image. The frequencies on the x-axis of the image were converted into frequencies on the y-axis via the ratio of the image dimension. The resulting frequency histogram is displayed in Fig. 44c. This frequency histogram $N(f_{\mathrm{ellip}})$ is fitted to a phenomenologically appropriate lognormal function with a constant offset, whereby low frequencies are cut off with a high-pass filter, given by

$$N_{\mathrm{lognorm}} = \frac{\alpha_0}{\sqrt{2\pi} \cdot \sigma \cdot f_{\mathrm{r}}} \cdot \exp\left(-\frac{(\log f_{\mathrm{r}} - \mu)^2}{2 \cdot \sigma^2}\right) + \alpha_1 \,. \tag{91}$$

The lognormal function enables the histogram to be reduced to the few parameters of α_0 and α_1, which are scaling factors as well as the statistical quantities μ and σ, which are variants of the mean value and standard deviation of a normal distribution, respectively. For a quantitative informative value of the lognormal function, its expected value is determined via $f_{\mathrm{r,\,expect}} = \exp(\mu + \frac{\sigma^2}{2})$. Based on this, a characteristic feature size is estimated, whereby the reciprocal value of the expected frequency is multiplied by the conversion factor from pixel to the physical length of $1\,\mathrm{px} = 0.516\,\mu\mathrm{m}$.

The resulting feature size S_{expect} is thus given by

$$S_{\text{expect}} = f_{\text{r, expect}}^{-1} \cdot 0.516\,\mu\text{m}\,\text{px}^{-1}\,. \tag{92}$$

This evaluation procedure is applied once to images containing grown domains of different ion doses but no additional in-plane field and once again to an image series of the non-bombarded sample with changing ip field strength. Care was taken to ensure that the grown domains cover the major part of the image. Once this state has been achieved no further growth pulses were applied in order not to arbitrarily widen the dendrimeric strands. Due to the time limitation of the work, this evaluation method has been applied to a limited extent. Thus, all presented results are based on domains with positive pre-saturation. Figures

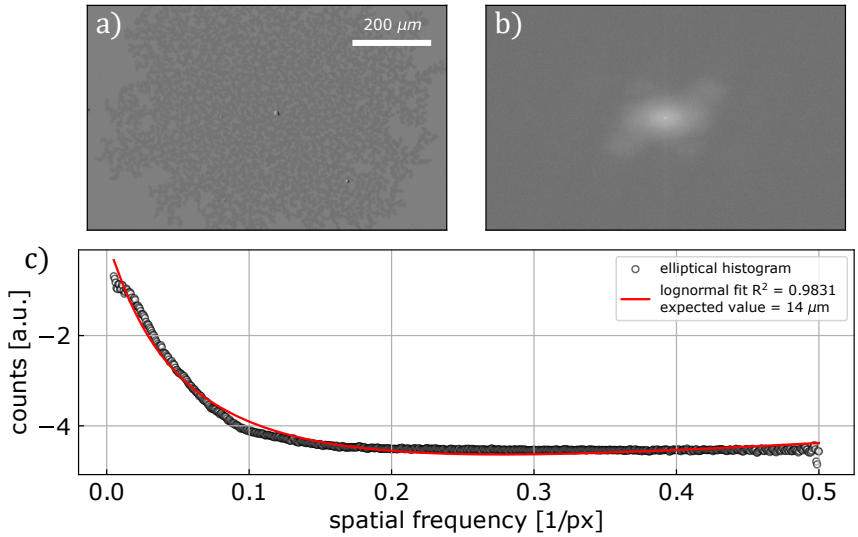

Figure 45: Exemplary calculation of the feature size of a sample region bombarded with $D_{\text{IB}} = 7.5{\cdot}10^{13}\,\text{cm}^{-2}$ (a)) via FOURIER transformation (b)) and subsequent formation of a elliptical histogram (c)). The expectation value for the feature size is estimated by the expectation value of a fitted lognormal distribution.

44 and 45 exemplify the FOURIER transformation based size analysis for a non-bombarded region an region bombarded with $D_{\text{IB}} = 7.5 \cdot 10^{13}\,\text{cm}^{-2}$, respectively. This represents the largest difference in ion dose and thus most likely also the largest differences in the domain feature sizes. A comparison of the expected values of both evaluations agrees well with this expectation and, regarding the scale bars in the attached images, also seems to deliver values in a reasonable magnitude, especially when it is considered that the more complex size distribution is reduced to a single parameter.

This trend is also partially visible if the feature sizes, determined by this method, are plotted against the corresponding ion doses, as in Fig. 46, in which the expected decreasing trend does occur within large deviations. However, this is mainly due to the point of the highest ion dose, otherwise, it would resemble a stagnant trend. The limited informative value is probably due to the small number of measuring points as well as the evaluation method. On

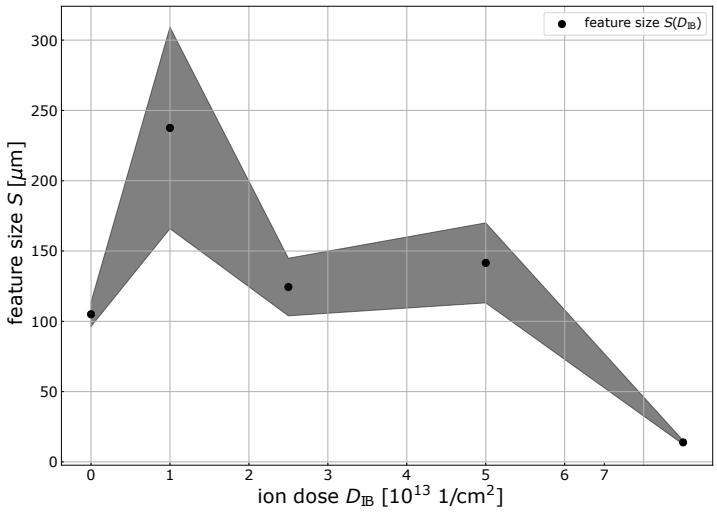

Figure 46: Uncertain decrease of the domain feature size with ion bombardment dose determined by the evaluation based on the 2D FOURIER transformation.

the one hand, the measurement method using the absolute proportions of the 2D Fourier transformation is not sensitive to one type of domain but always to both types of domains. A comparison of the underlying images in Figures 46 a) and 47 a) shows that the intermediate areas between the grown domains are significantly smaller than in the bombarded region. This is probably also explained by the small peak around $f_\mathrm{r} \approx 0.12\,\mathrm{px}^{-1}$ in the histogram, which is missing in the shelled region. This higher frequency is correspondingly associated with smaller feature size. In addition, the resulting histogram is reduced to a single value via the fit and the associated expected value, which is tantamount to a strong simplification. A consideration of all frequencies, for example by subtracting the histograms of both Fourier transformations from one another, which was no longer carried out due to time constraints, could provide information about which spatial frequencies occur more frequently and which less frequently and which less frequently.

The method appears to obtain even less meaningful results for the analysis of the domain size over the applied field, as shown in Fig. 47. Since the decrease in domain size was observed as a function of the absolute field strength, a maximum around $\mu_0 H_\mathrm{x} = 0\,\mathrm{mT}$ was expected

with decreasing trends upon increasingly absolute field strengths, which is not observed. A possible explanation for this, apart from the already mentioned reasons, is that the decrease in feature size over the magnetic field, in contrast to the decrease over the bombardment, has a preferential direction. While the feature sizes orthogonal to the applied field decrease, the feature sizes along the external field increase. Accordingly, to determine the reduction, the histogram of the Fourier analysis should be formed along the x- and y-axes of the image. A possibly more revealing method could be based on automatic edge detection, utilizing,

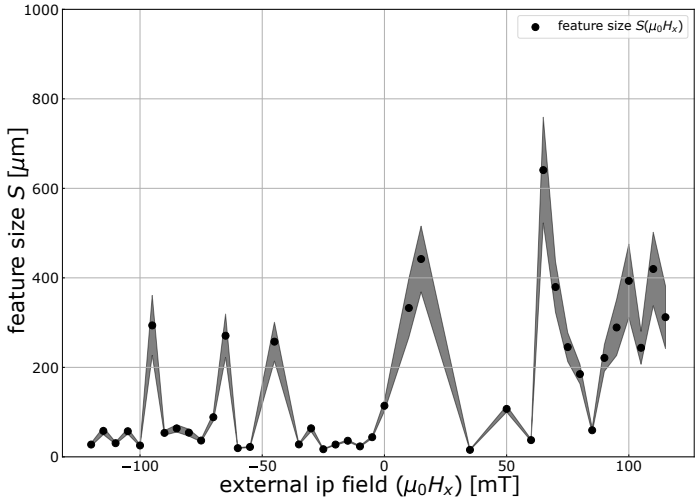

Figure 47: Domain feature size in dependence of the ip field strength, determined by the evaluation based on the 2D Fourier transformation. No trend is visible contradicting the qualitative investigation of the recorded MOKE images.

for example, a Tenenbaum gradient or a high pass filter. With such a method, edges, i.e., domain walls in subtraction images, can be converted into intensities, which would make it possible to measure the feature size in arbitrary directions via peak-to-peak distances. Furthermore, the method could be linked to the binarized images to enable domain-specific size determination. With an edge detection method, the pre-grown or pre-nucleated domains could be neglected, which is helpful in the field-dependent decrease of the feature size since the nucleation was always performed in absence of an ip field. However, in the binarized images, the grown domains might appear distorted or migrated, due to the 2D filtering, which usually caused a broadening of the observed domains. The Tenenbaum gradient is an approximation of a numerical gradient image via convolution of the original image with the empirical Sobel operators [38].

7.3 Automatization of Asymmetric Bubble Expansion

The automatization of the measurement procedure could improve comparability, relieve the experimenter and increase the number of measurements by, for example, a series of measurements performed overnight. This would also help to improve the method, e.g., via parameter optimization. For such automatization, three major problems were identified during the experiments of this work, which will be briefly summarized in this section. Some solutions are also proposed, although these have not been applied.

The first problem is thermal oscillations, which on the one hand move the FOV on the sample surface, and the other hand shifts the sample surface out of the focal plane. The second problem is the limited reproducibility of the nucleation domain. Without manual verification, it is unpredictably unclear whether a measurement was successful or not. The last and third problem primarily affects the high ip field strengths, in which undesirable phenomena, exemplified in Fig. 48 a)-d), increasingly occur. These phenomena mainly concern the growth of another domain into the FOV. However, phenomena such as the apparent switching between domain types have been observed as well.

Autofocus

Thermal fluctuation affects the observed FOV as well as the focal plane. The former was hardly observed in the experiments and it can be partially compensated for via shifting the images. The latter, however, has adverse effects, since large fluctuations can render the image completely unusable, and even small fluctuations can reduce the domain contrast. In the experiment, the focus was therefore readjusted at regular intervals of at least five minutes. In an automatized version, this would have to be done by a program. The conference contribution [38] presents a study of the applicability of 13 different algorithms to biological objects that are proposed to be able to find the focal plane. Based on the results of this study and the available experiences with the Tenenbaum gradient in this working group, this is regarded as a promising algorithm for readjusting the focus at regular intervals, such as every 10 pulses. However, the feasibility of the Tenenbaum gradient as well as the readjustment intervals have to be verified.

Recognition of Individual Nucleation Phenomena

The reproducibility of the nucleation of individual domains, located in the center of the FOV and with a suitable size and shape, is limited. At a few defect-associated sample positions, it was possible to nucleate several times in a row without any problems, but quite often it was not possible to nucleate a single, suitable domain, even after a moderate double-digit number of attempts. The probability could be partly increased experimentally by switching several times between the saturation magnetizations and changing the sample's magnetic history, but no way was found to ensure stable nucleation or at least nucleation with a reproducible probability.

In principle, this problem can be partially compensated for by simply taking more measurements and then discarding and remeasure incorrect measurements. However, this is quite an inefficient approach. Automatized detection of whether a suitable domain has been nucleated, would be preferable. A simple and easy-to-implement detection could be realized by calculation of the average intensity before and after a nucleation pulse. Depending on the polarization filter and saturation, there should be a sudden increase or decrease in the intensity upon successful nucleation, which magnitude corresponds to the size of the nucleated domain. With help of calibration, this could be utilized to determine whether a domain with a possibly suitable size has been nucleated. However, this simple approach does not provide any information about the domain's location and whether several small domains or domains at the FOV edges are nucleated. Nevertheless, this method might be well suited as a low-threshold preliminary test. Upon positive return of this test, a subsequent more precise but mathematically more complex detection method can be carried out. Such a more complex detection method could involve, for example, machine learning, such as random forest walk or neural layered networks, as well as clustering via principle component analysis (PCA), in which a program is taught what a successfully nucleated domain looks like in a previously manually recorded training data set. The system can then compare new measurements to check whether a nucleation pulse was successful, whereby the feasibility is depending on the complexity of the domain structures. Recognition is anticipated to be comparably easy for bubble domains, whereas the dendrimeric domains of this work might pose a greater challenge.

Parasitic Effects

With increasing ip field strengths, the probability of parasitic effects, occurring during the measurement, increases, with some selected effects exemplified in Fig. 48 a)-d). These mainly involve bubble-like domains, associated with significantly higher domain wall velocities.

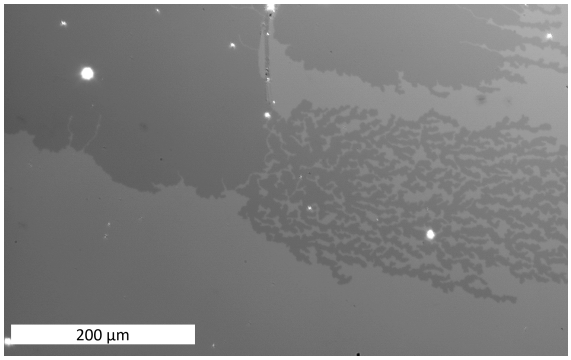

(a) Bubble domain reaching the investigated dendrimeric domain.

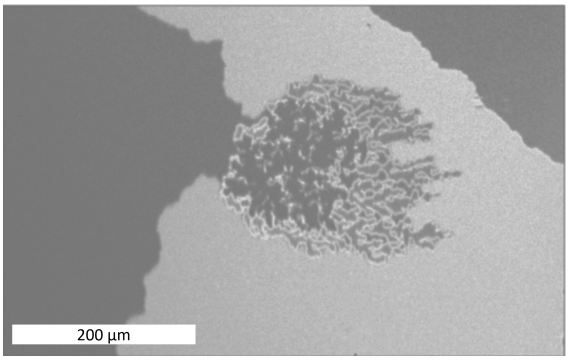

(b) Subtraction image of a partially enclosed dendrimeric domain.

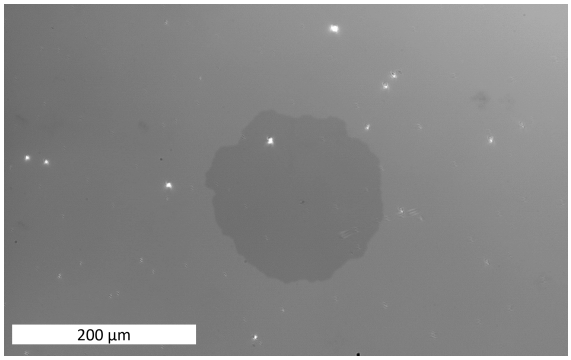

(c) Bubble domain with a rough surface.

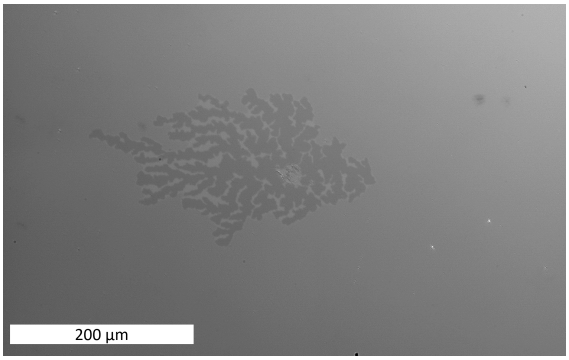

(d) The dendrimeric domain is enclosed by a bubble domain, which is only visible in a slightly brighter area around the dendrimeric domain.

Figure 48: Some selected examples of parasitic effects limiting the asymmetric bubble expansion method. The rather trivial case of other dendrimeric domains growing into the FOV is omitted. Figures 48a and 48b display a dendrimeric domain partially reached or enclosed by a bubble-like domain. In addition, figure 48a displays a partial conversion between the two kinds of domains in the upper corner. Figure 48c displays the rarely occurred case of a nucleated bubble domain. In general, the bubble domains are associated with significantly higher domain wall velocities and, therefore, they mostly fill up the entire FOV within a growth pulse. Since the area around the dendrimeric domain is then already remagnetized, the dendrimeric domain is not able to expand any further and usually freezes in its movement. This is hardly visible except for a small edge around the domain, as shown in Fig. 48d. This has been the most prominent parasitic effect besides other dendrimeric domains growing inside the FOV.

In addition to the exponentially dependent growth rate, which quickly exceeds the FOV at high fields, this is one of the two reasons that limit the measurable ip field range due to the sample. In principle, the exponential growth can be partially compensated by selecting the pulse duration and the oop field strength. It was not checked whether a different choice of these two parameters might also limit the parasitic effects.

The only correlation found during the measurements is that domains nucleated outside the FOV can grow into the FOV. Suppressing unwanted nucleations could at least eliminate this parasitic contribution. One possibility for this could be the targeted introduction of defects as energetically low-threshold nucleation centers. These could make it possible for nucleation to appear there even at lower fields, which does not occur in other parts of the sample. However, the defect must be limited to a small area in order not to make a significant contribution to asymmetric bubble expansion. One possibility that should be mentioned at this point is bombardment in the nanometer range using a helium ion microscope (HIM). As already mentioned in section 6.1, the ion bombardment causes the magnetic reversal to begin at lower field strengths, which corresponds exactly to the desired effect described. This effect seems to be also valid in the nanometer range with a roughly 100 nm precision shown in [39, 40]. It might therefore be promising for controlled nucleation sites.

8 Summary and Discussion

This work can be briefly summarized into three parts, concerning the quantification of the interfacial DMI in sections 3 and 4, the local modification via He^+ ion bombardment in sections 5 and 6, and a few additional investigations addressing the asymmetric bubble expansion method in section 7.

In the first part, the successful quantification of the interfacial DMI in dendrimeric domains is demonstrated, whereby the main experimental method is based on magneto-optical investigations of NÉEL domain wall velocities of oop domains in presence of an additional applied magnetic ip field. For the DMI quantification, the MOKE setup has been refined and a new measurement procedure and an evaluation program have been established, extracting the domain wall velocity. Thereby, the domain wall velocity is typically determined in the MOKE images, resembling a stop-motion movie of the domain wall movement, by the detection of intensity edges [9], corresponding to domain walls in the MOKE images [21]. In [9] it is pointed out that the typical method of edge detection for precise extraction of the domain wall velocities is difficult or even impossible for rough or dendrimeric domains. The difficulties arise from the numerous edges present in the dendrimeric domain texture. Instead, the recorded images are binarized according to their changes in magnetization and evaluated statistically. This binarization approach is thus capable of avoiding the problems arising from edge detection. The image processing steps and the subsequent velocity extraction (being presented in section 4.3) operated reasonably in the manually recorded images and are also expected to be capable of quantifying the DMI of other samples with perpendicular magnetic anisotropy. It might furthermore be capable of dealing with domain textures deviating from the texture studied in this work.

However, the evaluation is merely based on a few images and a small parameter variation range, and should thus not be considered as a fully operational tool but rather as a foundation for future studies. It may be verified and sophisticated in systematic studies involving parameter sweeps and further differing samples. Besides the parameter sweeps, a few optimization strategies are given in this work, which are mainly addressed in section 7.3. The parameter sweep involves experimental parameters such as the applied field strengths, the pulse duration, and the Kerr contrast, while also evaluation parameters may be varied, like the size of the 2D filter, the parameters for determining binarization and FOV growth threshold, and the size of the ROI. Additionally, the program can be upgraded by enabling velocity

determination in arbitrary angles or an automatized measurement procedure. Since the binarization of the images worked well, it could perhaps be applied in other studies concerning samples with PMA.

One disadvantage of the binarization approach is a shift in the domain walls arousing mainly from the 2D filtering process, whereas in all manually reviewed images, the growing domain appeared always enlarged resulting in a supposedly overestimated velocity. This particularly affects small, closely packed domain texture, in which additionally the gaps in between might be filled up and consequently significantly higher growth velocities might be detected. According to the observations in section 7.2, this especially applies to the domains at high ion doses and high ip fields. In addition, defects may also be misinterpreted as domains, which in particular influence the determination of the center of mass of the nucleated domain. The velocity determination is only affected if the defects are located in the FOV. With a lower domain contrast, noisy images, or images with high defect densities, the program might fail in detecting the domain. The main reasons for the time-consuming measurement procedure are the limited reproduction of domain nucleation and parasitic effects, whereby section 7.3 provides a few approaches to handle them.

The experimental recording procedure of the MOKE images itself may also be improved, for example, by carrying out a preliminary measurement without an ip field and with a varying oop field, which is then employed to specify the material parameters via a fit of the creep law [9]. These are then applied as initial information for the actual asymmetric bubble expansion series. It is also conceivable to test in advance whether the sample and the fields are properly aligned by comparing whether the growth for the ip fields $\pm H_\mathrm{x}$ is symmetrical [9]. In addition, the basic creep law can be adapted as suggested in Tab. 2.

There are also software-based determination methods such as the MOKAS software, which determines the growth rate via jumps in the grayscale value of individual pixels [9]. The pulse duration of one second, in particular, should also be mentioned, which is significantly longer in comparison to some publications [9, 22], while others apply similar pulse durations [41]. The reason for this originates most likely from the deviating type of domain since it has been observed that the bubble domains possess higher domain wall velocities.

In addition to the intrinsic DMI field H_DMI, accessible in the asymmetric bubble expansion experiments, the saturation magnetization, the layer thickness, and the effective crystal anisotropy were also determined experimentally. The resulting values are very close to known values for the sample system considered [16]. The hereby operated VVSM-based methods

for determining the saturation magnetization and effective magnetic anisotropy are mainly intended as supplementary methods to estimate the impact of the ion bombardment on the sample's properties and are thus relevant for the second part of this work. With the measured values, the DMI is determined to a reasonable value [9, 16], whereby its sign has been determined by the mutual directions of the magnetization, external magnetic field, and main growth direction in the asymmetric bubble expansion experiments.

Table 5: Summary of the non-bombarded sample's most important magnetic parameters in this work. These are the saturation magnetization M_S, the effective magnetic anisotropy K_{eff}, the intrinsic DMI field H_{DMI}, the exchange stiffness A_{ex}, and the interfacial DMI D. All parameters have been measured experimentally in section 4, besides the exchange stiffness A_{ex}, which has been taken from [16].

quantity	$M_S\,[\mathrm{kA\,m^{-1}}]$	$K_{eff}\,[\mathrm{J\,m^{-3}}]$	$\mu_0 \cdot H_{DMI}\,[\mathrm{mT}]$	$A_{ex}\,[\mathrm{J\,m^{-1}}]$	$D\,[\mathrm{mJ\,m^{-2}}]$
value	591 ± 55	$2 \cdot 10^5 \pm 1.2 \cdot 10^4$	78 ± 19	$1.6 \cdot 10^{-11}$	$+0.41 \pm 0.14$

As a result, this first part of the work presents a working model for determining the interfacial DMI, which, however, still has many possibilities for optimization. In particular, the number of measured data and samples should be increased to test and verify the method. An extension of the experimental methods with other methods known from the literature, for example, Brillouin Light Scattering [8, 9], could also contribute to the improvement and verification of the method. Since the evaluation deviates from the typical in some points, especially concerning binarization and ROI, the here implemented method for asymmetric bubble expansion could also be applied to typical bubble domains for verification.

This correspondingly still highly experimental model was applied directly in the second part of this work, the 10 keV He^+ ion bombardment experiments, in which it has been demonstrated that a modification of the DMI in the dose range from $1 \cdot 10^{13}\,\mathrm{cm^{-2}}$ to $1 \cdot 10^{14}\,\mathrm{cm^{-2}}$ is possible. However, only a few data points are currently available suggesting a reduction in the DMI of around 40%, although the uncertainties measured would in principle also enables other trends. In other measurements, an increase in the DMI due to the ion bombardment could also be observed [11, 8]. Comparison of the measured DMI trend, it may be possible that such an increase could appear in the range of lower ion doses. To achieve these lower ion doses, it is presumably necessary to perform the ion bombardment experiments with a tilted angle, which has been theoretically discussed and simulated here. This should be able to reduce the ion dose, whereby the angle also influences the interaction itself, as shown in section 5.4.

The generally strong modifications in the sample properties with the comparably low ion doses [8] could be due to the very thin layer system of only a few atomic layers. However, the original assumption of intermixing as the reason for the changes in the DMI with ion bombardment could not be confirmed by employing SRIM simulations. It is unclear whether the modifications have a different origin or whether the simplified SRIM simulations carried out do not adequately reflect the situation.
Therefore, the investigation has to be extended, which might involve other, more simple sample systems and more detailed simulations. Other works draw a connection between ion bombardment and intermixing [42, 8]. The intermixing could be verified experimentally by measuring the samples with transmission electron microscopy (TEM) or a focused ion beam (FIB) with secondary ion mass spectrometry (SIMS). However, both methods are destructive investigations, which in the case of the TEM is caused by the sample preparation.
In the third part of the work, the different directions of growth of the domains and changes in the domain texture with the ion bombardment and the ip field were briefly discussed. The changes in the domain texture with the ion bombardment have already been mentioned in previous works [26]. There are three important points to be highlighted

- Without further external effects, the dendrimeric domains seem to grow isotropically on a statistical average, which is a not further discussed condition for the asymmetric bubble expansion

- The feature sizes of the domains decrease with the ion dose, which is qualitatively observed in the associated images. This trend is only partially evident in the presented method for determining the feature size. All domains were conveniently observable with a 50x magnification, whereby the MOKE setup enables magnification up to 400x. Even higher ion doses should therefore be resolvable if the magnification is adjusted. This contradicts the observations in [26] but would make a larger dose range accessible experimentally. The deviations from [26] could be since the ISA has been serviced in the meantime and the ion dose determined in [26] might have been larger than expected

- With increasing dose in ion bombardment, the magnetization reversal magnetic field decreases, resulting in an earlier start of the magnetization reversal process, i.e., a reduction in the energy barriers for magnetization reversal. Therefore, it might be useful, for example, to bombard small areas in HIM (helium ion microscopy) experiments and thus cause reproducible centers of nucleation.

The size dependency of the features in the domain texture was only evident to a limited extent with the method based on 2D Fourier transformation, which is particularly true for the dependency of the magnetic field strength. Possible causes for this are given in section 7.2. It is unclear whether the latter is also related to the DMI and whether it could enable a method for its determination that could be independent of the nucleation in the FOV. Such a method, decoupled from individual domains, may have great advantages, especially concerning the experimental procedure.

Since lower field strengths were generally used at higher ion doses to fill the FOV within 12 pulses, it can be assumed that the velocity increases, which was compensated for by the lower field strengths. All in all, the work can be summarized by the fact that the existing Kerr microscope was expanded to include asymmetric bubble expansion as a method for determining the DMI. It is possible to quantify the DMI not only from bubble domains but from dendrimeric or maze-like domains as well. In addition, it was quantitatively shown that ion bombardment can locally modify the DMI. All these investigations form the basic building block for future investigations of the DMI and its modification via ion bombardment.

These include, for example, spintronic devices, magnetic memory technologies [4, 5, 6] or non-linear neural networks with ion gradients [43]. Thereby, ion bombardment might be an important extension, as it allows local modification of the DMI and energy barriers. For example, a method for the targeted, local nucleation of skyrmions via He^+ ion bombardment was recently presented, which represents a possibility for engineered nanopatterning of samples [39, 40]. With this method, it is also possible to isolate the skyrmions in the bombarded regions [39, 40]. It is also possible to control the density of skyrmions with the ion bombardment [44]. Depending on the application, also a decrease of the DMI is favorable, like in MRAM (magnetic random access memory) cells, in which the DMI may have disruptive impact as a reduced thermal stability and an increased switching current [45]. For these cases, a method for quantifying and possibly reducing the DMI is important as well.

References

[1] I. Dzyaloshinskii. "A Thermodynamic Theory of Weak Ferromagnetism of Antiferromagnetics". In: *J. Phys. Chem. Solids* 4 (4 1958), pp. 241–255. DOI: 10.1016/0022-3697(58)90076-3.

[2] T. Moriya. "New Mechanism of Anisotropic Superexchange Interaction". In: *Phys. Rev. Lett.* 4 (5 Mar. 1960), pp. 228–230. DOI: 10.1103/PhysRevLett.4.228.

[3] M. Bode et al. "Chiral Magnetic Order at Surfaces Driven by Inversion Asymmetry". In: *Nature* 447 (May 2007). DOI: 10.1038/nature05802.

[4] G. Finocchio et al. "Magnetic Skyrmions from Fundamental to Applications". In: *J. Phys. D* 49.42 (Sept. 2016). DOI: 10.1088/0022-3727/49/42/423001.

[5] F. Būttner, I. Lemesh, and G. Beach. "Theory of Isolated Magnetic Skyrmion from Fundamentals to Room Temperature Applications". In: *Sci. Rep.* 8 (1 Mar. 2018). DOI: 10.1038/s41598-018-22242-8.

[6] B. Dieny et al. "Opportunities and Challenges for Spintronics in the Microelectronics Industry". In: *Nat. Electron.* 3 (8 Aug. 2020). DOI: 10.1038/s41928-020-0461-5.

[7] C. Back et al. "The 2020 Skyrmionics Roadmap". In: *J. Phys. D* 53.36 (June 2020). DOI: 10.1088/1361-6463/ab8418.

[8] H. Nembach et al. "Tuning of the Dzyaloshinskii-Moriya Interaction by He^+ Ion Irradiation". In: *J. Appl. Phys.* 131 (14 Apr. 2022). DOI: 10.1063/5.0080523.

[9] A. Magni et al. "Key Points in the Determination of the Interfacial Dzyaloshinskii-Moriya Interaction from Asymmetric Bubble Domain Expansion". In: (2022). DOI: 10.48550/arXiv.2201.04925.

[10] K. L. J. Moon S. Seo and M. Stiles. "Spin-Wave Propagation in the Presence of Interfacial Dzyaloshinskii-Moriya Interaction". In: *Phys. Rev. B* 88 (18 Nov. 2013). DOI: 10.1103/PhysRevB.88.184404.

[11] M. V. L. Herrera Diez and D. Ravelosona. "Enhancement of the Dzyaloshinskii-Moriya Interaction and Domain Wall Velocity Through Interface Intermixing in Ta/CoFeB/MgO". In: *Phys. Rev. B* 99 (5 Feb. 2019). DOI: 10.1103/PhysRevB.99.054431.

[12] D. Jiles. *Introduction to Magnetism and Magnetic Materials*. Third. CRC Press, Sept. 2015. ISBN: 9781482238884. DOI: 10.1201/b18948-8.

[13] S. Chikazumi. *Physics of Ferromagnetism*. Second. Oxford University Press, Apr. 2009. ISBN: 9780199564811.

[14] L. Bergmann and C. Schāfer. *Lehrbuch der Experimentalphysik Band 6 - Festkörper*. Ed. by R. Kassing. Second. De Gruyter, Sept. 2005. ISBN: 3110174855.

[15] K. Buschow and F. de Boer. *Physics of Magnetism and Magnetic Materials*. First. Kluwer Academic Publishers, Dec. 2003. ISBN: 0306484080.

[16] M. Li et al. "Magnetic Domain Wall Substructures in Pt/Co/Ni/Ir Multi-Layers". In: *J. Appl. Phys.* 130 (15 Oct. 2021), p. 153903. DOI: 10.1063/5.0056100.

[17] B. D. V. Franco. *Magnetic Measurement Techniques for Materials Characterization*. First. Springer Nature Switzerland AG, Sept. 2021. ISBN: 9783030704421. DOI: 10.1007/978-3-030-70443-8.

[18] G. Herzer. *Properties and Applications of Nanocrystalline Alloys from Amorphous Precursors - The Random Anisotropy Model*. Springer, Mar. 2006, pp. 15–34. ISBN: 1-4020-2963-2. DOI: 10.1007/1-4020-2965-9_2.

[19] H. Draaisma and W. de Jonge. "Surface and Volume Anisotropy from Dipole-Dipole Interactions in Ultrathin Ferromagnetic Films". In: *J. Appl. Phys.* 64 (7 Oct. 1988). DOI: 10.1063/1.341397.

[20] D. Lau. "Experimental Evaluation of the Interfacial Dzyaloshinskii-Moriya Interaction in Co/Ni Magnetic Multilayers". PhD thesis. Carnegie Mellon University, Aug. 2018.

[21] A. Hubert and R. Schāfer. *Magnetic Domains - The Analysis of Magnetic Microstructures*. Third. Springer Science & Business Media, 2009, p. 23. ISBN: 9783540641087.

[22] D. Lau. "Disentangling Factors Governing Dzyaloshinskii Domain-Wall Creep in Co/Ni Thin Films Using Pt_xIr_{1-x} Seed Layers". In: *Phys. Rev. B* 98 (18 Nov. 2018). DOI: 10.1103/PhysRevB.98.184410.

[23] M. Li et al. "Lorentz TEM Investigation of Chiral Spin Textures and Néel Skyrmions in Asymmetric $[Pt/(Co/Ni)_M/Ir]_N$ Multi-Layer Thin Films". In: *Phys. Rev. Mater.* 3 (6 June 2019), p. 064409. DOI: 10.1103/PhysRevMaterials.3.064409.

[24] E. Joven, A. del Moral, and J. Arnaudas. "Magnetometer for Anisotropy Measurement using Perpendicular Magnetization". In: *J. Magn. Magn. Mater.* 83 (1-3 Jan. 1990), pp. 548–550. DOI: 10.1016/0304-8853(90)90620-6.

[25] P. Bloemen et al. "Magnetic Anisotropy Determined from Angular Dependent Magnetization Measurements". In: *MRS Online Proceedings Library OPL* 231 (May 1991). DOI: 10.1557/PROC-231-479.

[26] F. Ott. "Modification of Magnetic Anisotropies in Perpendicular Magnetized Mulitlayer Systems". functional thin films and physics with synchrotron radiation. MA thesis. University of Kassel, Sept. 2021.

[27] S. Je et al. "Asymmetric Magnetic Domain-Wall Motion by the Dzyaloshinskii-Moriya Interaction". In: *Phys. Rev. B* 88 (21 Dec. 2013). DOI: 10.1103/PhysRevB.88.214401.

[28] P. Chauve, T. Giamarchi, and P. L. Doussal. "Creep and Depinning in Disordered Media". In: *Phys. Rev. B* 62 (10 Sept. 2000). DOI: 10.1103/PhysRevB.62.6241.

[29] P. Metaxas et al. "Creep and Flow Regimes of Magnetic Domain-Wall Motion in Ultrathin Pt/Co/Pt Films with Perpendicular Anisotropy". In: *Phys. Rev. Lett.* 99 (21 Nov. 2007). DOI: 10.1103/PhysRevLett.99.217208.

[30] S. E. E. Martinez and G. Beach. "Current-Driven Domain Wall Motion Along High Perpendicular Anisotropy Multilayers: The Role of the Rashba Rield, the Spin Hall Effect, and the Dzyaloshinskii-Moriya Interaction". In: *Appl. Phys. Lett.* 103 (7 Aug. 2013). DOI: 10.1063/1.4818723.

[31] J. K. D. Han N. Kim and C. You. "Asymmetric Hysteresis for Probing Dzyaloshinskii-Moriya Interaction". In: *Nano Lett.* 16 (7 June 2016). DOI: 10.1021/acs.nanolett.6b01593.

[32] *OpenCV Documentation on cv2.moments*. https://docs.opencv.org/3.4/d0/d49/tutorial_moments.html. Accessed: 2022-09-13.

[33] L. H. Diez et al. "Controlling Magnetic Domain Wall Motion in the Creep Regime in He+-irradiated CoFeB/MgO Films with Perpendicular Anisotropy". In: *Appl. Phys. Lett.* 107 (3 July 2015). DOI: 10.1063/1.4927204.

[34] M. Z. J. Ziegler J. Biersack. *SRIM - The Stopping and Range of Ions in Matter*. Fifth. Lulu.com, Dec. 2008. ISBN: 9780965420716.

[35] N. Henning. "Strukturelle und Magnetische Veränderungen in Schichtsystemen mit Grenzflächenaustauschkopplung nach dem Beschuss mit keV-Heliumionen". functional thin films and physics with synchrotron radiation. PhD thesis. University of Kassel, 2018.

[36] A. Gaul. "Erzeugung Remanent Stabiler Domänenmuster in Austauschverschobenen Dünnschichtsystemen Mittels Heliumionenmikroskopie". functional thin films and physics with synchrotron radiation. PhD thesis. University of Kassel, 2017.

[37] M. Momota, H. Miike, and H. Hashimoto. "Measuring Particle Size Distribution by Digital Image Processing with Inverse Fourier-Bessel Transformation". In: *Jpn. J. Appl. Phys.* 33.2 (Feb. 1994). DOI: 10.1143/jjap.33.1189.

[38] B. N. Y. Sun S. Duthaler. "Autofocusing Algorithm Selection in Computer Microscopy". In: (2005). DOI: 10.1109/IROS.2005.1545017.

[39] K. R. R. Juge K. Bairagi and J. Vogel. "Helium Ions Put Magnetic Skyrmions on the Track". In: *Nano Lett.* 21 (7 Mar. 2021). DOI: 10.1021/acs.nanolett.1c00136.

[40] L. Kern et al. "Deterministic Generation and Guided Motion of Magnetic Skyrmions by Focused He^+-Ion Irradiation". In: *Nano Lett.* 22 (10 May 2022). DOI: 10.1021/acs.nanolett.2c00670.

[41] A. Hrabec et al. “Measuring and Tailoring the Dzyaloshinskii-Moriya Interaction in Perpendicularly Magnetized Thin Films”. In: *Phys. Rev. B* 90 (2 July 2014). DOI: 10.1103/PhysRevB.90.020402.

[42] X. Ma et al. “Interfacial Control of Dzyaloshinskii-Moriya Interaction in Heavy Metal Ferromagnetic Metal Thin Film Heterostructures”. In: *Phys. Rev. B* 94 (18 Nov. 2016). DOI: 10.1103/PhysRevB.94.180408.

[43] K. Song, J. Jeong, and B. Pan. “Skyrmion-Based Artificial Synapses for Neuromorphic Computing”. In: *Nat. Electron.* 3 (3 Mar. 2020). DOI: 10.1038/s41928-020-0385-0.

[44] Y. Hu et al. “Precise Tuning of Skyrmion Density in a Controllable Manner by Ion Irradiation”. In: *ACS Appl. Mater. Interfaces* 14 (29 July 2022). DOI: 10.1021/acsami.2c07268.

[45] M. K. J. Sampaio A. Khvalkovskiy and N. Reyren. “Disruptive Effect of Dzyaloshinskii-Moriya Interaction on the Magnetic Memory Cell Performance”. In: *Appl. Phys. Lett.* 108 (11 Mar. 2016). DOI: 10.1063/1.4944419.

9 Appendix

In this appendix additional information regarding the performed VVSM experiments are provided in the sections 9.1 and 9.2. The section 9.3 contains further information on the modifications of the KERR microscopic setup and section 9.4 summarizes all experimentally determined paramters in dependence on the ion dose.

9.1 Optical Determination of the Sample Surface Area

For the interpretation of the absolute magnetization values of the VVSM measurements in section 4.1, the volume of the magnetic material is a crucial parameter as depicted in Eq. (55) and (56). Furthermore depicted in the later equation is the separation of the volume V into the layer thickness t_{FM} of the magnetic material and the surface area of the entire sample A. The surface area is in the range of a few mm^2 and thus allocatable with high precision by means of an optical microscope e.g., the confocal laser scanning microscope (CLSM) from the company KEYENCE. With this microscope the whole sample area of all three samples of interest have been scanned individually.

The complete area images, generated by stitching several separately scanned areas together, are presented in Fig. 49. In areas without any sample material, the CLSM microscope measured the background (fibers of an underlaying cloth) and thus created insignificant measurement artifacts there.

With the open source image processing program *Fiji - ImageJ*, the sample areas in the images in Fig. 49 were colored white (pixel value 255) and the background was colored black (pixel value 0). For this the functions *Make Binary*, *Invert*, *Fill Holes* and *Invert* were applied in this order. Between the *Make Binary* and the first *Invert* process, all white areas which were clearly outside of the sample surface were removed manually. These are primarily caused by the scale bar in the lower right corner.

The sample surface area in terms of px^2 was then determined by multiplying the image size (height $\times$ width) by the reduced mean pixel value $\frac{\overline{z}}{z_{\max}}$ of the discretized images. The resulting value represents the number of pixels associated to the surface area.

$$A_{\mathrm{px}^2} = w \times h \cdot \frac{\overline{z}}{z_{\max}} \,. \tag{93}$$

Before applying this image processing procedure, the scale bars were transformed into a pixel to µm length conversion ratio of $\alpha_{\mu\mathrm{m}} = 2.7\,\mu\mathrm{m}\,\mathrm{px}^{-1}$, which is true for all of the three images.

Applying this conversion ratio squared to the pixel areas of each sample results in the total size of the sample area, which are depicted together with the discretized images in Fig. 50.

(a) Sample 1a) with an image size of 1856 px × 2064 px.

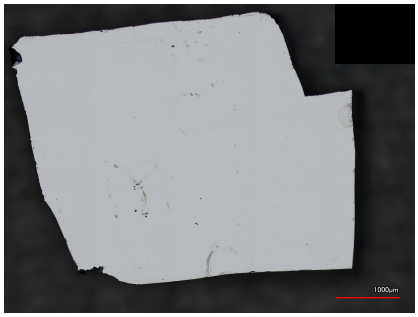

(b) Sample 1b) with an image size of 2304 px × 1728 px.

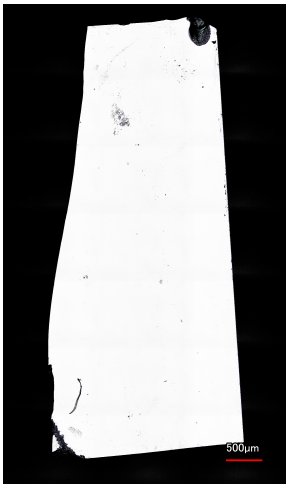

(c) Sample 1c) with an image size of 1408 px × 2400 px.

Figure 49: Images of the samples 1a) - 1c) taken with the optical CLSM microscope. The total image dimension in $width \times height\,(w \times h)$ is depicted as well.

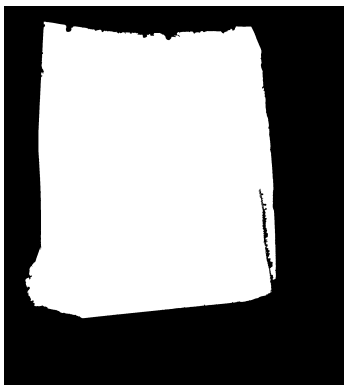

(a) surface area of sample 1a): $A_{\mathrm{mm}^2} = 1.458\,\mathrm{mm}^2$.

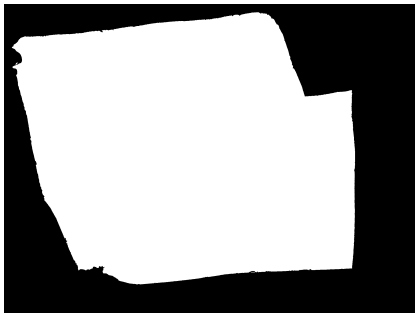

(b) Surface area of sample 1b): $A_{\mathrm{mm}^2} = 1.777\,\mathrm{mm}^2$.

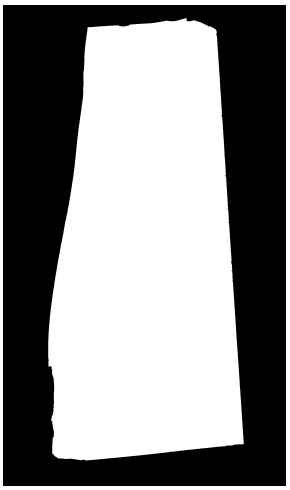

(c) Surface area of sample 1c): $A_{\mathrm{mm}^2} = 1.344\,\mathrm{mm}^2$.

Figure 50: Discretized images of the samples 1 a) - c) of Fig. 49 showing the associated sample surface in white. The rows below display the sample area in px^2 and mm^2, respectively.

9.2 VSM - Angular Resolved Hysteresis Curves

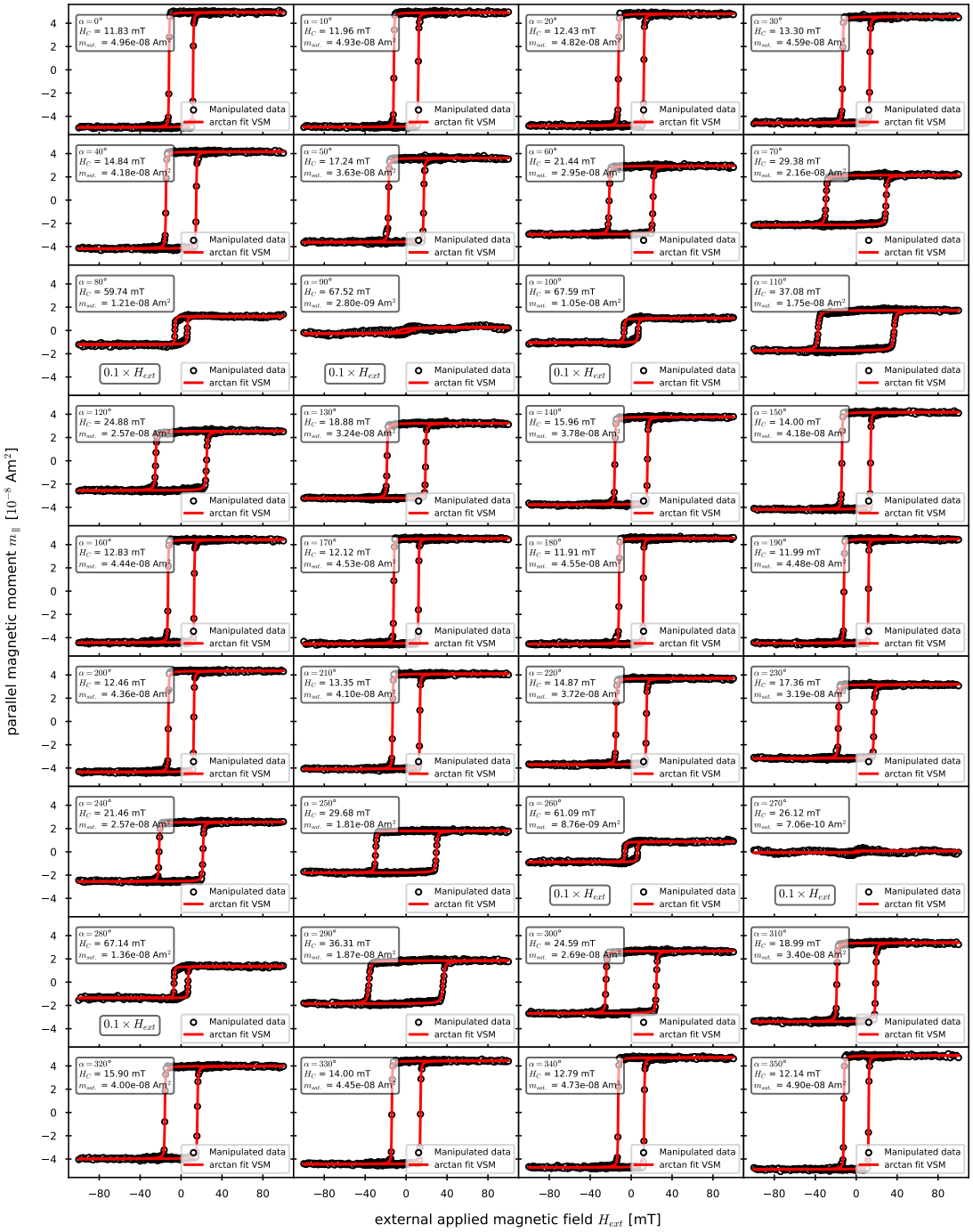

Figure 51: Angular resolved hysteresis curves of the sample 1c. Depicted is the post-processed magnetization $m_y = m_\perp$ parallel to the external applied field in a rotation angle range of $0° \leq \alpha \leq 360°$ and field ranges of either $-1000\,\mathrm{mT} \leq |H_{\mathrm{ext}}| \leq 1000\,\mathrm{mT}$ or $-100\,\mathrm{mT} \leq |H_{\mathrm{ext}}| \leq 100\,\mathrm{mT}$ depending on the rotation angle. All hysteresis curves possesses regions of saturation in both magnetization directions.

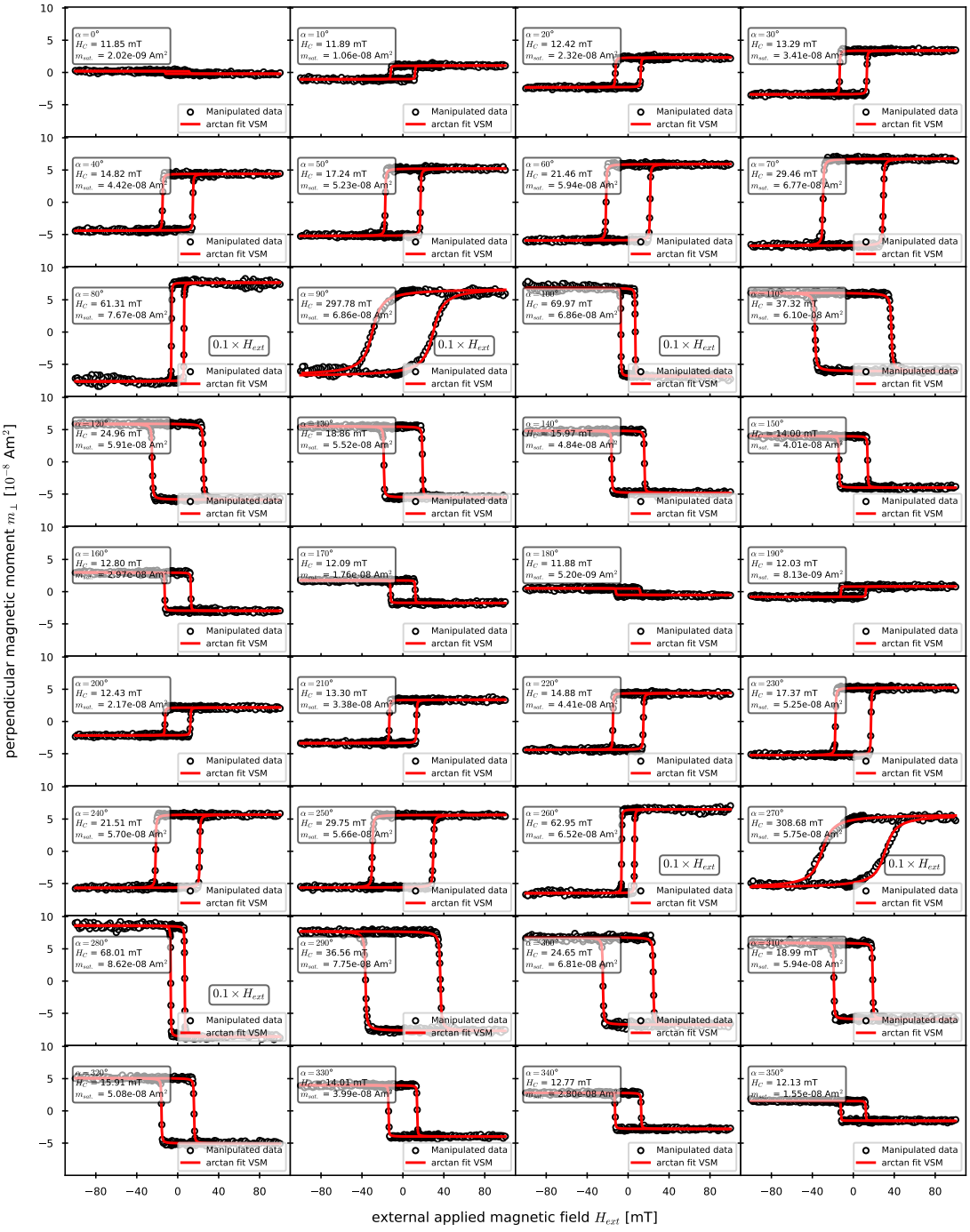

Figure 52: Angular resolved hysteresis curves of the sample 1c. Depicted is the post-processed magnetization $m_y = m_\perp$ parallel to the external applied field in a rotation angle range of $0° \leq \alpha \leq 360°$ and field ranges of either $-1000\,\mathrm{mT} \leq |H_\mathrm{ext}| \leq 1000\,\mathrm{mT}$ or $-100\,\mathrm{mT} \leq |H_\mathrm{ext}| \leq 100\,\mathrm{mT}$ depending on the rotation angle. All hysteresis curves possesses regions of saturation in both magnetization directions.

9.3 Modifications in the Wide Field Kerr Microscopy Setup

In this section, the two minor modifications of the wide-field KERR setup are contained and thus provide additional information to the optical setup introduced in section 3.2.2. The new

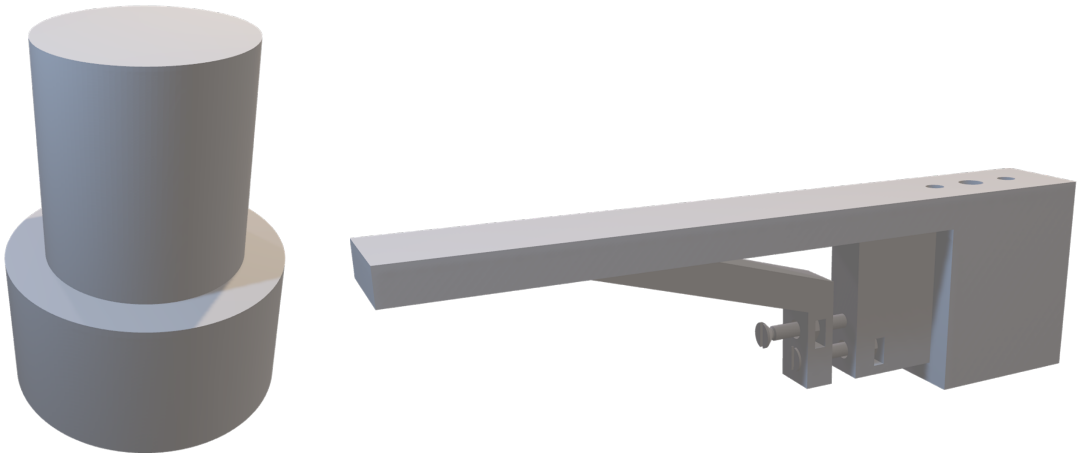

(a) CAD design of the new oop iron core.

(b) CAD design of the modified sample holder.

Figure 53: CAD models of the new modifications on the KERR microscopy setup consisting of an new iron core for the oop electromagnet as well as a stabilized sample holder with the possibility of tilt correction.

out-of-plane iron core in Fig. 53a replaces the old one, which was composed of two individual iron cores held together by a 3D printed mounting component. It offers more support with a larger area, resulting in more homogeneous fields with better reproducibility.
The sample holder in Fig. 53b has been extended by the stability-enhancing crossbar for noise reduction. This crossbar additionally possess two embedded screws which allow tilting around the x-axis via mechanical tension. These screws are intended for tilt correction but they should also be able to intentionally tilt the sample as long as the tilt does not result in material fatigue or damages. The limit of the tilt has not been verified but it is expected to lie in the lower two-digit region if given in angle degrees.

9.4 Summary of Ion Dose Dependent Parameters

This section provides overview over the saturation magnetization M_S (see Fig. 54), the effective magnetic anisotropy K_{eff} (see Fig. 55), and the intrinsic DMI field H_{DMI} (see Tab. 7) in dependence on the ion bombardment dose D_{IB} of the He^+ ion bombardment experiment described in section 5.3. This section's content is intended to provide additional information for section 6 in which the dependence on the ion bombardment is discussed in detail. The Tab. 6 gives a brief overview of the determined values prior to the ion bombardment. The dependence of the saturation magnetization and effective magnetic anisotropy on the ion bombardment is graphically depicted in Figs. 54 and 55, respectively. Lastly, Tab. 7 summarizes all performed asymmetric bubble expansion experiments and thus also contains the ion dose dependence of the intrinsic DMI field.

Table 6: Summary of the sample's most important magnetic parameters in this work. These are the saturation magentization M_S, the effective magnetic anisotropy K_{eff}, the intrinsic DMI field H_{DMI}, the exchange stiffness A_{ex}, and the interfacial DMI D. All parameters have been measured experimentally in section 4, besides the exchange stiffness A_{ex}, which has been taken from [16]. This is a repetition of Tab. 5.

quantity	$M_S\,[\mathrm{kA\,m^{-1}}]$	$K_{eff}\,[\mathrm{J\,m^{-3}}]$	$\mu_0 \cdot H_{DMI}\,[\mathrm{mT}]$	$A_{ex}\,[\mathrm{J\,m^{-1}}]$	$D\,[\mathrm{mJ\,m^{-2}}]$
value	591 ± 55	$2 \cdot 10^5 \pm 1.2 \cdot 10^4$	78 ± 19	$1.6e-11$	0.41 ± 0.14

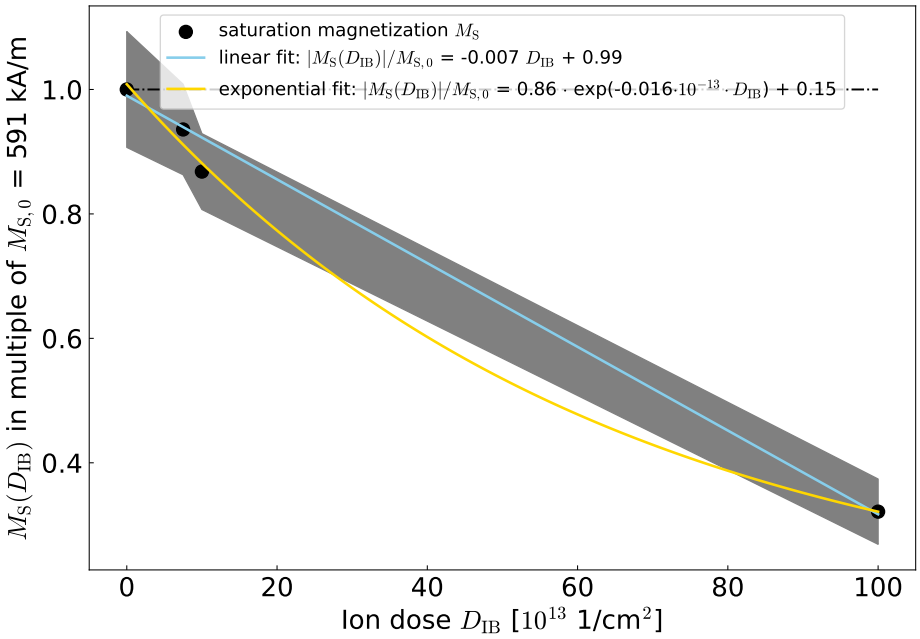

Figure 54: Expansion of Fig. 36, displaying the dependence of the saturation magnetization (black dots) on the ion bombardment dose of all measured doses. The trend has been fitted by a linearly (blue) and an exponentially decreasing function (yellow), both given in the legend.

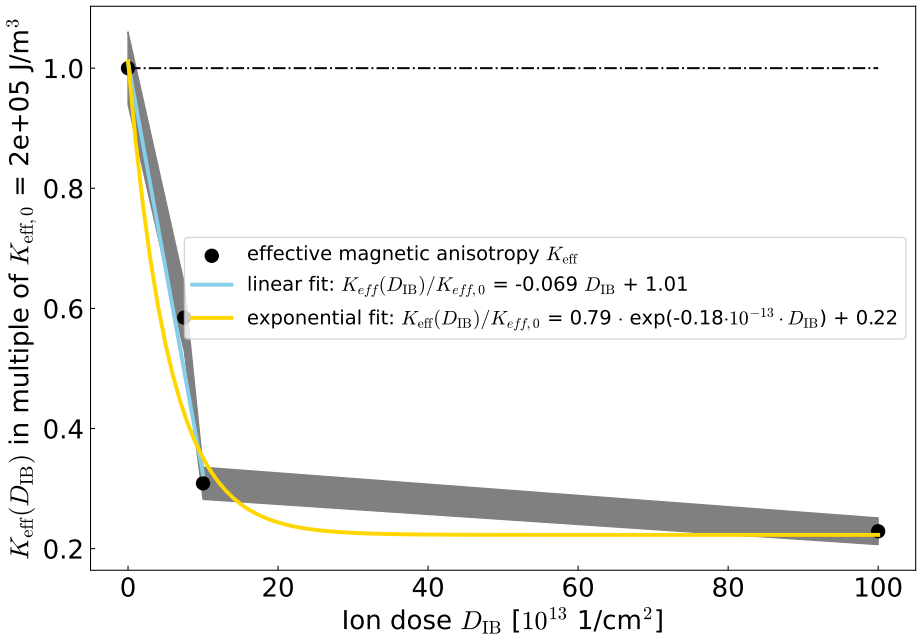

Figure 55: Expansion of Fig. 38, displaying the dependence of the effective magnetic anisotropy (black dots) on the ion bombardment dose of all measured doses. The trend has been fitted by a linearly (blue, only the first three points) and an exponentially decreasing function (yellow), both given in the legend.

Table 7: Summary of all asymmetric bubble expansion measurements of bombarded and non-bombarded sample regions. The results of this table are graphically represented in Fig. 39. Starting from top, the measured regions are bombarded by the ion doses $D_{\mathrm{IB}} = 0$, 1, 2.5, 5, and $7.5 \cdot 10^{13}\,\mathrm{cm}^{-2}$.

negative pre-saturation	positive pre-saturation
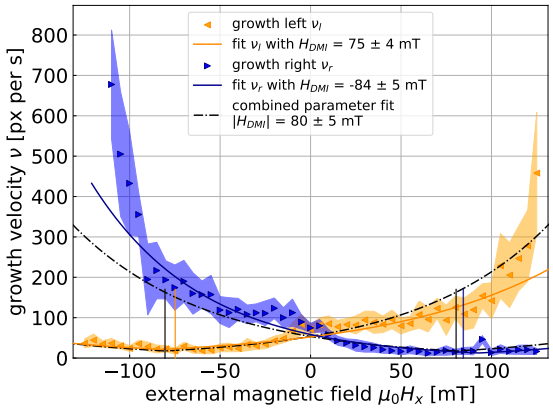	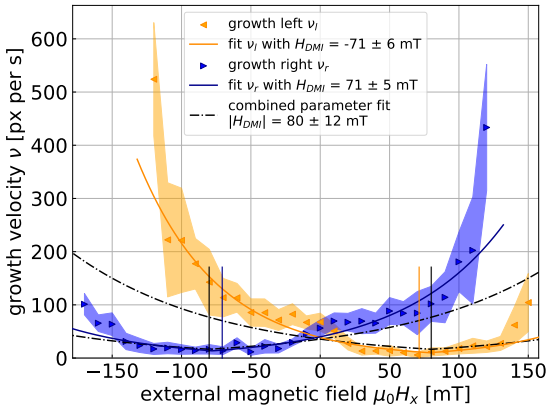
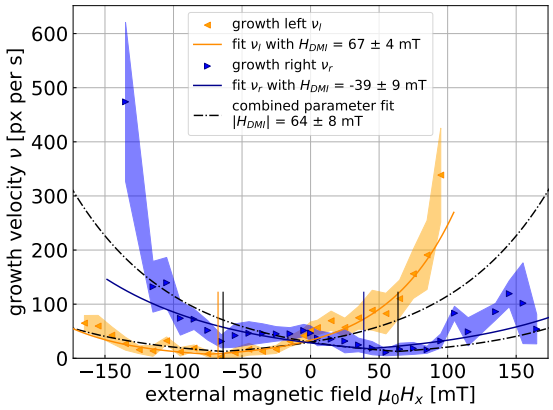	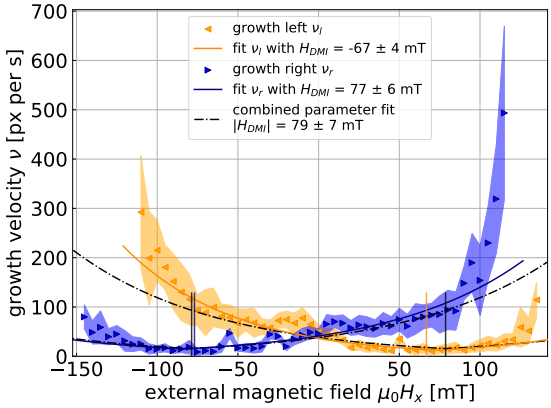
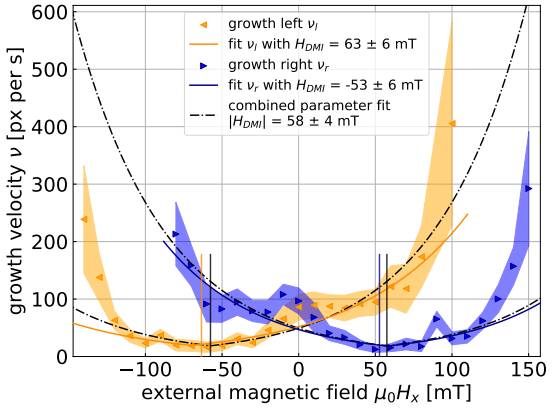	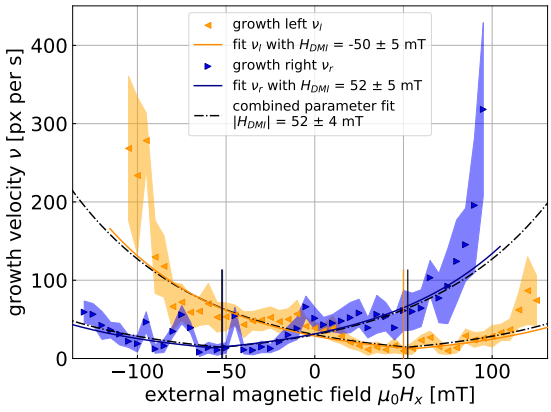

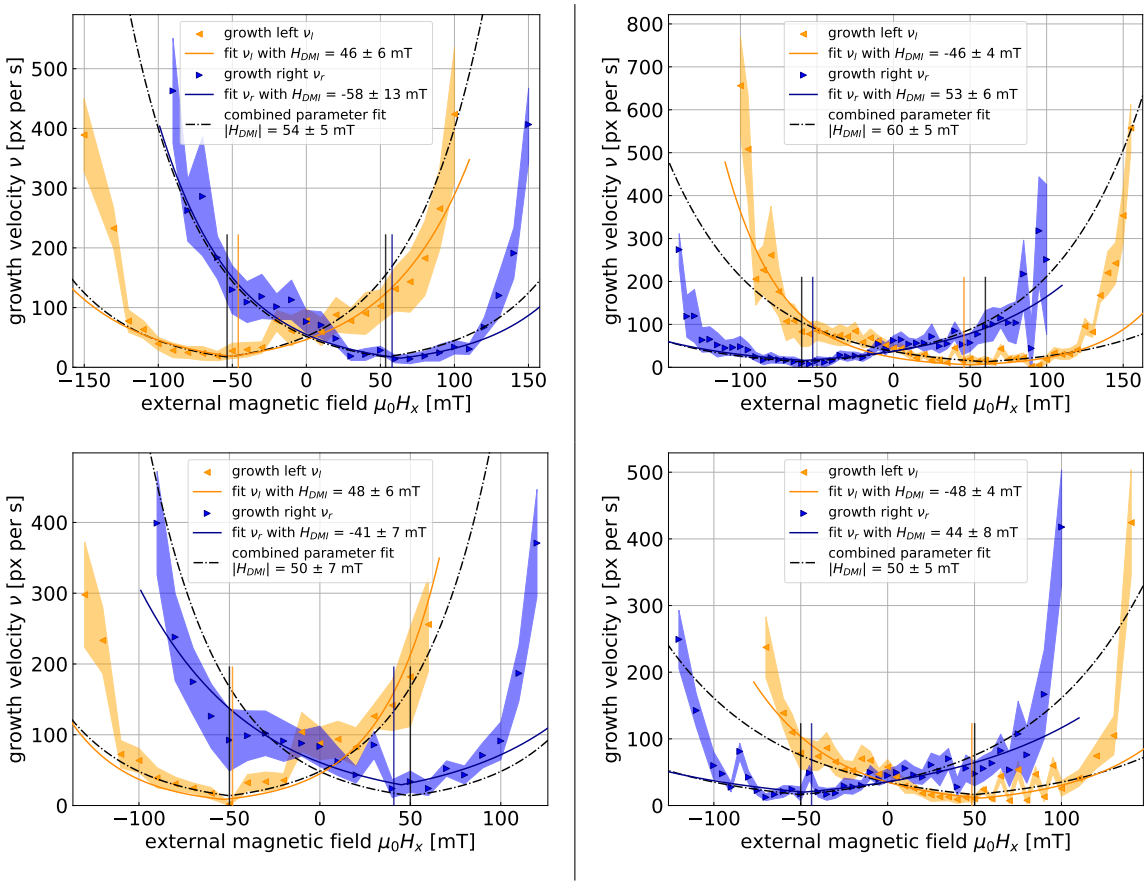
growth left ν_l
fit ν_l with H_{DMI} = 46 ± 6 mT
growth right ν_r
fit ν_r with H_{DMI} = -58 ± 13 mT
combined parameter fit
$|H_{DMI}|$ = 54 ± 5 mT
growth velocity ν [px per s]
external magnetic field $\mu_0 H_x$ [mT]
growth left ν_l
fit ν_l with H_{DMI} = -46 ± 4 mT
growth right ν_r
fit ν_r with H_{DMI} = 53 ± 6 mT
combined parameter fit
$|H_{DMI}|$ = 60 ± 5 mT
growth velocity ν [px per s]
external magnetic field $\mu_0 H_x$ [mT]
growth left ν_l
fit ν_l with H_{DMI} = 48 ± 6 mT
growth right ν_r
fit ν_r with H_{DMI} = -41 ± 7 mT
combined parameter fit
$|H_{DMI}|$ = 50 ± 7 mT
growth velocity ν [px per s]
external magnetic field $\mu_0 H_x$ [mT]
growth left ν_l
fit ν_l with H_{DMI} = -48 ± 4 mT
growth right ν_r
fit ν_r with H_{DMI} = 44 ± 8 mT
combined parameter fit
$|H_{DMI}|$ = 50 ± 5 mT
growth velocity ν [px per s]
external magnetic field $\mu_0 H_x$ [mT]

Declaration of Independence

I hereby confirm that I have written this thesis with the title **Quantification and Local Modification of the Interfacial DMI** independently and have not used any resources other than those specified. The parts of the work that are taken from other works (including internet references) in wording or meaning have been identified and the reference has been indicated.

Eigenständigkeitserklärung

Hiermit bestätige ich, dass ich die vorliegende Arbeit mit dem Titel **Quantification and Local Modification of the Interfacial DMI** selbständig verfasst und keine anderen als die angegebenen Hilfsmittel benutzt habe. Die Stellen der Arbeit, die dem Wortlaut oder dem Sinn nach anderen Werken (dazu zählen auch Internetquellen) entnommen sind, wurden unter Angabe der Quelle kenntlich gemacht.

Kassel, den 16.09.2022

location, date

signature